

Digital output tilt sensor with conductive microspheres

A dissertation submitted to

ETH ZÜRICH

for the degree of
Doctor of Sciences

presented by

LARS BÜTHE

Dipl.-Ing., Friedrich-Alexander-Universität Erlangen-Nürnberg
MTM, University of New South Wales
born April 25, 1986
citizen of Germany and the United States

accepted on the recommendation of

Prof. Dr. Gerhard Tröster, examiner
Prof. Dr. Christofer Hierold, co-examiner

2017

Lars Bütke

Digital output tilt sensor with conductive microspheres

Diss. ETH No. 24085

First edition 2017

Published by ETH Zürich, Switzerland

Printed by Druckzentrum ETH

Copyright © 2017 by Lars Bütke

All rights reserved. No part of this publication may be reproduced, stored in a retrieval system, or transmitted, in any form or by any means, electronic, mechanical, photocopying, recording, or otherwise, without the prior permission of the author.

To my parents

Acknowledgments

The results of this project could only be achieved with the generous support of many individuals who I would hereby like to express my gratitude:

First and foremost, this thesis would not have been possible without my supervisor, Prof. Dr. Gerhard Tröster. I would like to thank him not only for his guidance during the time I spent in his group and for providing excellent research facilities, but also for his trust by giving me great freedom in conducting my work. Whenever required, he made himself available for valuable advice. His encouragement to present the results my work at various international conferences was highly appreciated. In addition, I enjoyed the sharing of his personal experience and opinions which helped me broaden my horizon beyond the scope of the thesis.

Special thanks go to Prof. Dr. Christofer Hierold for his time for reviewing my thesis and acting as a co-examiner in my doctoral committee.

My sincere appreciation goes to our former and current support staff at the Electronics Laboratory: Ruth Zähringer who always was helpful to solve any administrative issues or give advice on life in Switzerland, Fredy Mettler with whom I enjoyed interesting discussions in the mornings and who supported me with his broad network at ETH, and Paul Holz who was of great help in tackling new ideas and technical challenges.

I would like to thank my close colleagues who I collaborated with and who supported me by providing valuable advice and fruitful discussions: Giuseppe Cantarella, Alwin Daus, Thomas Kinkeldei, Stefan Knobelspies, Niko Münzenrieder, Luisa Petti, Christian Vogt, and Christoph Zysset.

Through my funding project iCareNet, I had the pleasure of closely working with Julia Seiter and receiving helpful input from Prof. Dr. Oliver Amft and many other gifted researchers all around Europe. I would also like to express my gratitude to Dr. Kunigunde Cherenack, Timon Grob and Hans de Vries who readily accepted me as a guest researcher at Philips Corporate Technologies in Eindhoven.

I would like to thank all my former office mates who helped me getting started in Switzerland: Franz Gravenhorst, Michael Hardegger and Amir Muaremi. Additionally, the supportive atmosphere at the institute was fostered by many other colleagues: Rolf Adelsberger, Bert

Arrrich, David Bannach, Ulf Blanke, Alberto Calatroni, Mathieu Chan-son, Simon Christen, Burcu Cinaz, Sebastian Feese, Tobias Grosshauser, Thomas Holleczek, Andreas Hösl, Catherine Ikae, Vanessa Klaas, Matthias Flückiger, Martin Kusserow, Andreas Mehmann, Long-Van Nguyen-Dinh, Daniel Roggen, Mirco Rossi, Giovanni Salvatore, Christina Strohrmann, Bernd Tessororf, Matija Varga, Daniel Waltis-berg, Martin Wirz, Zack Zhu, and Rolf Zinniker.

Many parts of this work were realized in the FIRST clean room which is run by a very dedicated and committed team: Emilio Gini, Yargo Bonetti, Silke Schön, Tobias Häusler, Sandro Loosli, Maria Leibinger, Peter Diedrich, Petra Burkard, Hansjakob Rusterholz, and Rachel Schumacher. I am also thankful to Martin Lanz for his support in the fabrication of photolithography masks. Sincere thanks go to Christian Mathis for our discussions and the assistance for the friction measurement and to Jinwoong Cha for his help during the high speed image recordings.

Furthermore, I would like to thank Patrick Brülisauer, Sandra Fer-reiro, Elizabeth Ren, Wojciech Staszewski, Haralds Capkevics, Silvio Bischof, Renato Huber, Petar Jokic, and Guido Gandus for their ex-cellent inputs they delivered working on their semester and master theses.

Not having sufficient room to name them all, my sincere thanks go to all other colleagues at ETH that I had the pleasure to meet and work with on many different occasions and projects, who helped me to grow along the road and have a fruitful time at ETH.

Last but not least, I want to express special thanks to my family - my parents and my sister - for their unlimited trust and wholehearted support in all my endeavors. They spared no effort to provide me with the best education possible and for that I am eternally grateful.

Zürich, December 2016

LARS BÜTHE

Contents

Acknowledgments	vii
Abstract	xiii
Zusammenfassung	xv
1. Introduction	1
1.1 Motivation	2
1.2 State of the art	3
1.2.1 Accelerometers	3
1.2.2 Tilt sensors	5
1.2.2.1 Solid pendulum	5
1.2.2.2 Liquid pendulum	7
1.2.2.3 Gaseous pendulum	8
1.3 Contributions	8
1.4 Thesis outline	10
1.5 Publications	11
2. Sensor system	15
2.1 Sensing principle	16
2.2 Design and architecture	17
2.2.1 Tilt switch	17
2.2.2 Tilt sensor	19
2.3 Sensor properties	22
2.4 Conclusion	22
3. Pendulum	25
3.1 Material selection	26
3.1.1 Liquids	27
3.1.2 Solids	28
3.2 Pendulum preparation	30
3.3 Conclusion	31

4. Cavity	33
4.1 Stacking of polyimide layers	34
4.1.1 Fabrication process	34
4.1.2 Bendability	37
4.2 SU-8 cavity	38
4.2.1 Fabrication process	39
4.2.1.1 Pillar dimensions	40
4.2.1.2 UV exposure	42
4.2.1.3 Surface cleaning	44
4.2.2 Bendability	45
4.3 Conclusion	46
5. Contact mechanics	47
5.1 Electrical contact resistance	48
5.2 Surface properties	52
5.2.1 Surface roughness	52
5.2.2 Friction	56
5.3 Conclusion	58
6. Sensor modeling	59
6.1 Definition of parameters	60
6.1.1 Design parameters	60
6.1.2 Evaluation parameters	62
6.2 Control of design parameters	63
6.2.1 Resolution	64
6.2.2 Non-linearity	64
6.3 Conclusion	71
7. Evaluation	73
7.1 Tilt switch	74
7.1.1 Experimental setup	75
7.1.2 Static performance	76
7.2 Tilt sensor	76
7.2.1 Experimental setup	78
7.2.2 Static performance	80
7.2.3 Response time	83
7.2.4 Dynamic performance	86
7.3 Conclusion	88

8. Conclusion	89
8.1 Summary and achievements	90
8.2 Scalability and limitations	90
8.3 Conclusions	91
8.4 Outlook	92
8.4.1 Materials and technology	92
8.4.2 Sensor design	92
8.4.3 Sensor readout	93
Appendix	95
Bibliography	99
Glossary	111
Curriculum Vitae	115

Abstract

Knowledge of a device's orientation with respect to gravity has been and still is of great interest for mankind. Since the invention of the pendulum as one of the first man-made instruments determining the tilt, major advances have been made in the measuring principle, accuracy and size of tilt sensing devices. Tilt sensors can be found in various areas of practical application including construction, transport and logistics, process automation, consumer products, etc. Recent research and development successfully helped to reduce size and energy consumption of the sensors. As a result of consumer devices, such as wearables, moving closer to the body, the flexibility of the deployed parts becomes a critical prerequisite to increase user comfort and feature long-term and accurate measurements.

The iCareNet focuses as a research network on contributions to healthcare, wellness, and assisted living (HWA). Within the scope of this network, a new tilt sensor concept is explored in this thesis. The pendulum of the tilt sensor, consisting of conductive microspheres, creates an electrical connection between contact pads on the substrate surface of the cavity. The location of the pendulum in the cavity is determined by a resistance measurement which indicates the state of each contact pad and, thus, identifies the contact pads that are connected to each other. With the help of a look-up table, the digital output of the steady states of the contact pads is used to determine the applied tilt.

The device is fabricated utilizing standard cleanroom processes on flexible 50 μm -thick polyimide (PI) foil as the substrate. Commercially available solder spheres with a diameter of 250 μm are deployed as a pendulum. A gold coating of the microspheres is applied to achieve a reliable electrical contact with the surface of the substrate. Roughness and friction measurements of the substrate and microsphere surface determine the influence of adhesion forces which are negligible for a contact with SU-8, but are relevant for a contact with the substrate.

Two different tilt sensing devices are developed, fabricated and evaluated: a tilt switch gives an indication on the tilt direction without information about the magnitude of the tilt, while a tilt sensor with several circularly arranged contact pads can be used to measure the tilt angle of the device.

The tilt switch is fabricated by means of stacking several PI layers which have been structured using photolithography and subsequent

dry-etching, and are glued together. The cavity's inner dimensions are $10 \times 3 \times 0.3 \text{ mm}^3$, its maximum bending radius is 5 cm. The make angle and the break angle of this device are 5° and 25° , respectively.

In contrast, the cavity of the tilt sensor is defined by a pillar structure of the photoresist SU-8. The circular cavity with SU-8 pillars has a diameter of 2 mm and a height of $300 \mu\text{m}$ and is bendable down to 2 cm bending radius. A comprehensive model of the tilt sensor is introduced which determines the influence of design parameters of contact pads as well as cavity and pendulum. The resolution of the tilt sensor is dependent on the number of contact pads which - together with the amount of microspheres - determines the non-linearity of the resulting device.

Exemplarily, tilt sensors with 4 and 8 contacts are fabricated, achieving a resolution of 45° and 22.5° , respectively. A reliable electrical contact as well as a minimal hysteresis of the microsphere movement is achieved at a tilt of the sensor plane of 50° . The response time of the pendulum of the tilt sensor is approximately 50 ms which allows to operate the device at rotational speeds of up to 20 rpm with an accuracy of more than 50 %.

Zusammenfassung

Die Kenntnis über die Orientierung eines Objektes im Schwerkraftfeld ist in steigendem Masse von technischer Bedeutung. Das Pendel ist eines der ersten von Menschenhand geschaffenen Apparate, um die Neigung zu messen, und seit seiner Erfindung wurden erhebliche Fortschritte hinsichtlich Messprinzip, Genauigkeit und Abmessung der Neigungssensoren erzielt. Sie finden heute Einsatz in einer Vielzahl von Anwendungsgebieten, wie dem Baugewerbe, der Logistik, der Prozessautomatisierung, der Unterhaltungselektronik, etc. Die technische Innovation hat in den letzten Jahren zu immer kleineren Sensoren und gleichzeitig reduziertem Stromverbrauch geführt. Da Systeme wie „Wearables“ in steigendem Umfang näher am Körper eingesetzt werden, ist die Biegebarkeit der elektronischen Bauelemente zudem ein wichtiges Kriterium, um einen hohen Tragekomfort bei gleichzeitig akkurater Langzeitmessung zu gewährleisten.

Im Rahmen dieser Arbeit wird ein neuartiges Konzept für einen Neigungssensor präsentiert. Dabei schliesst das Pendel des Sensors, bestehend aus leitenden Mikrokugeln, elektrische Kontakte auf der Substratoberfläche in der Sensorkavität kurz. Über eine Widerstandsmessung, die den Zustand jedes Kontaktes angibt, wird die Position des Pendels in der Kavität bestimmt. Anhand einer Nachschlagetabelle wird anschliessend aus den Zustandsdaten der angelegte Neigungswinkel ermittelt.

Die Fertigung des Sensors erfolgt unter Anwendung üblicher Reinraumprozesse auf einem 50 μm dicken Polyimidsubstrat. Kommerziell erhältliche Lotkugeln mit einem Durchmesser von 250 μm bilden das Pendel. Eine Beschichtung dieser Kugeln mit Gold garantiert einen zuverlässigen elektrischen Kontakt mit der Substratoberfläche. Rauheits- und Reibungsmessungen zeigen, dass die Adhäsionskräfte für einen Kontakt des Pendels mit dem Substrat relevant sind, während sie für einen Kontakt mit den Seitenwänden vernachlässigt werden können.

Zwei verschiedene Sensoren zur Messung der Neigung werden entwickelt, hergestellt und charakterisiert: ein Neigungsschalter gibt die Richtung der Neigung an, während ein Neigungssensor mit mehreren kreisförmig angeordneten Kontakten zusätzlich den Neigungswinkel des Objekts ermittelt.

Der Neigungsschalter wird aus mehreren PI-Folien hergestellt, die durch Photolithographie und Trockenätzen strukturiert und anschlies-

send aufeinander gestapelt und miteinander verklebt werden. Die so erzeugte Kavität hat ein Volumen von $10 \times 3 \times 0.3 \text{ mm}^3$ und bleibt bis zu einem Biegeradius von 5 cm intakt. Bei einem Neigungswinkel von mindestens 5° wird der Kontakt geschlossen, bei einem Winkel von mehr als 25° wieder geöffnet.

Eine Säulenstruktur aus dem Polymer SU-8 definiert die kreisförmige Kavität des Neigungssensors. Sie hat einen Durchmesser von 2 mm mit einer Höhe von $300 \mu\text{m}$ und ermöglicht einen Biegeradius von bis zu 2 cm. Ein detailliertes Modell des Neigungssensors zeigt die Auswirkung verschiedener Designparameter bei Kontakten, Kavität und Pendel auf: die Auflösung des Neigungssensors ist abhängig von der Anzahl der Kontakte, die - zusammen mit der Anzahl der Mikrokugeln - die Nichtlinearität des Sensors beeinflusst.

Exemplarisch werden Neigungssensoren mit vier und acht Kontakten hergestellt, die eine Auflösung von 45° bzw. 22.5° aufweisen. Ein zuverlässiger elektrischer Kontakt sowie eine minimale Hysterese werden bei einer Neigung der Sensorfläche von 50° erreicht. Die Reaktionszeit des Pendels im Sensor liegt bei ca. 50 ms. Damit ist ein Einsatz des Sensors bei Rotationsgeschwindigkeiten von bis zu 20 min^{-1} mit einer Genauigkeit von über 50 % möglich.

1

Introduction

Sensors are an important part of wearables and other, related devices. In this work, we discuss a tilt sensor as knowledge about the orientation with respect to gravity is an important information in various applications.

The introduction motivates the work and provides an overview on existing tilt sensing devices. The contributions of this work are presented and the outline of the thesis is given.

1.1 Motivation

Knowledge about a device's orientation with respect to gravity is an important input parameter for many applications in various domains. From rough orientation measurements, e.g. for display orientation, up to precise measurements in building construction or navigation where a resolution down to a tenth of a degree is needed, tilt sensors need to cover a wide range of values and accuracies.

The human sensors for measuring tilt of the head are built inside the human ear, the utricle and the saccule that can measure the accelerations in both vertical and horizontal direction. Probably the first man-made device measuring the tilt was a pendulum. Since then, major advances have been made in the measuring principle, accuracy and size of tilt sensing devices. Possible areas of application include the construction as well as the transport and logistics domain where it is important to know whether goods have been transported in a correct way. Electronic devices such as smartphones or e-books also make use of tilt sensors in order to detect the display orientation, and automation in fabrication processes needs information about the orientation for control.

Nowadays, wearable sensors are becoming increasingly important as various applications in health care and sports require physiological data as input. This ranges from heart rate, skin resistance and body temperature to the knowledge in body movement and posture. The sensors for the latter two are usually placed in rigid electronic devices which then capture the required data. However, for an unobtrusive, longterm and accurate measurement, the sensors need to be placed even closer to the body, e.g. by integration into textiles. Therefore, research is designing flexible sensors providing an increased user comfort by creating smart textiles [1]. Recent work has already successfully investigated bendable sensors for temperature [2], pressure [3] or gas [4] signals, also mechanically flexible transistors have been realized [5].

For applications in the area of wearable computing such as activity monitoring [6], activity recognition [7] as well as movement analysis [8] or body posture detection [9], sensors are required which can measure the orientation of the body with respect to gravity. It has been shown that body posture detection is possible with off-the-shelf accelerometers [10, 11]. However, the sensors used are not suitable for unobtrusive textile integration as they are rigid and thus limit the bendability of the textile.

In this thesis, we will present a new tilt sensor principle which enables a mechanically flexible design of the sensor. At the same time, the sensor does not require an active power supply and provides a direct digital output. We evaluate different materials for the pendulum and different fabrication approaches for the cavity. The behavior of the sensor depending on the design parameters is modeled and the sensor characteristics are evaluated.

1.2 State of the art

The state of the art on devices for tilt measurement is summarized. We report mainly on devices which are small, i.e. where the sensing structure does not exceed dimensions of a few centimeters. Devices for navigation on aircraft and alike exceed this size [12] and are therefore excluded from the following report.

The first part will cover an overview on MEMS (micro-electro-mechanical system) accelerometers which are ubiquitously used in consumer electronics today. They can not only measure the orientation of the device with respect to gravity, but provide a value on the applied dynamic acceleration. This allows a usage of the devices especially in dynamic environments where a sampling rate of several 10 Hz and more is required. In the second part we cover the various concepts of tilt sensors targeting static applications.

1.2.1 Accelerometers

Most MEMS accelerometers are based on a proof mass which is displaced by the applied acceleration. The displacement of the proof mass is measured either by a piezoresistive or capacitive principle.

For a piezoresistive measurement, the beams supporting the proof mass are made from a piezoresistive material, such as zinc oxide (ZnO) or p-type silicon (Si) [13]. The deflection of the beam causes a change in resistance of the beam which allows to draw conclusions on the proof mass displacement and thus the acceleration. Huang et al. report on a MEMS fabricated accelerometer which can measure the acceleration perpendicular to the substrate plane [14]. Combined with other accelerometer designs which allow for an acceleration measurement in plane by a respective beam design [15, 16], a measurement of acceleration in all three dimensions is possible with a device fabricated

on a single substrate. More sophisticated structures enable a measurement of three components of linear acceleration as well as three components of angular acceleration where only a single proof mass is suspended [17]. The resulting chip with a size of $3 \times 3 \times 0.9 \text{ mm}^3$ allows a measurement range of up to 10 g and has a bandwidth of 300 Hz. An important parameter is the cross-sensitivity of the different applied acceleration dimensions. This is reduced to a minimum of $<1\%$ by design of a six-beam accelerometer with self-cancelling cross-axis sensitivity [18]. As already mentioned, accelerometers are especially suitable for dynamic applications. Atwell et al. have experimentally presented a piezoresistive accelerometer which is operational for accelerations up to 40 000 g [19].

While the piezoresistive measurement does not allow a measurement under static conditions, the capacitive principle is also suitable for DC measurement. However, their use is usually more complex in design as well as the evaluation electronics. The capacitive measurement is performed with an interdigitated electrode structure which increases the capacitance and therefore improves the signal to noise ratio (SNR). Either a change of the overlapping area or a distance change of the electrodes leads to a change in capacitance which can then be used to derive the applied acceleration. Luo et al. present such a structure for a CMOS accelerometer which measures the acceleration in plane [20]. Again, by combining this with a design which allows for out-of-plane measurement, a three-axis accelerometer is fabricated [21]. Finally, a device is presented by Sun et al. that only uses a single proof mass while enabling a three dimensional measurement [22]. With a chip size of $1.78 \times 1.38 \text{ mm}^2$, a reliable measurement of up to 6 g at an excitation frequency of 150 Hz can be achieved. All previously presented work is fabricated in bulk silicon, however, research has also started to work on other materials. An accelerometer fabricated on polyimide will enable new areas of application as also a flexible device can be envisioned [23].

Finally, thermal accelerometers operate without a proof mass. This reduces the amount of moving parts inside the sensing structure, thus making it less sensitive to shocks. A thermal accelerometer consists of a heater which is surrounded by thermosensitive structures. By applying an acceleration to the structure, the heat distribution inside the sensor is changed and allows to infer the magnitude of acceleration [24]. Due to the measurement principle, the 3 dB bandwidth of the thermal accelerometer is at 20 Hz and the device is therefore not suitable for high dynamic applications.

1.2.2 Tilt sensors

Tilt sensors can be classified by their type of pendulum. The pendulum is the part of the sensing structure - analog to the proof mass of accelerometers - which follows the direction of gravity and can either be solid, liquid or gaseous. The position of the pendulum is detected by various methods, based on resistance, capacitance, inductance, magnetism, optical and fiber-optical measurement. In the following, we will give an overview of the different sensing principles which are summarized in Tab. 1.1.

Literature provides the measurement range of the described tilt sensors, while few concepts also report on other parameters such as the achievable resolution. The response time which describes the required time from applying a tilt until the correct output signal is achieved is important for the description of the dynamic performance of tilt sensors. In Tab. 1.1 selective highlights with regard to these parameters are explicitly mentioned.

1.2.2.1 Solid pendulum

Mescheder et al. present a micromechanical tilt sensor which is - similar to the piezoresistive accelerometers - based on structure where a mass is displaced by the applied tilt and the resulting displacement measurement with piezoresistive elements [25]. Here, the proposed structure allows to measure the inclination in two axes with a range of $\pm 80^\circ$. A similar design of a solid beam stressing four piezoresistive springs enables a full turnover, i.e. 360° [26]. By copying the principle of the balance organ of a jellyfish, Smith et al. develop a device where a single metallic sphere with a diameter of 1.55 mm follows the orientation of gravity inside a cavity. The walls of the cavity consist of 60 SMD (surface mount device) resistors which are electrically connected by the metallic ball to the ground plane on the substrate surface [27]. The sensor has a resolution of 6° while requiring an extensive readout to measure the resistance of each of the 60 connections individually.

A capacitive sensor, also using a metallic ball, is proposed by Lee et al. Here, the metallic ball with a diameter down to 2.38 mm lies inside a plastic tube on top of two electrodes. By tilting the device, the ball changes its position inside the tube, leading to a change in capacitance with the electrodes [28]. This device was characterized for angles between 0° and 90° . Using bulk micromachining in a quartz wafer, a tilt sensor based on a capacitive accelerometer design is fabricated [29].

Other work uses the capacitive principle to present a tilt sensor with a 3-bit comb drive which enables a direct digital output of the sensor [30].

An inductive sensor is presented where a magnetic core with two permanent magnets fixed at the ends is placed inside a cylindrical container [31], achieving a response time as high as 3 s. The position of the magnetic core which is dependent on the device tilt is detected by two coils. The measurement range is $\pm 15^\circ$.

Another magnet-based sensor uses two magnets and a flux-gate sensor. The magnets are placed on either side of the flux-gate which detects changes in the magnetic field, when the magnets are tilted [32].

Constandinou et al. propose a micro-optoelectromechanical tilt sensor [33]. A circular array of 66 photodetector elements, arranged in 5° segments, detects the position of the solid pendulum. The pendulum is a semicircular mass and covers some of the photodetectors. A LED above the structure illuminates the photodetectors which are not covered, thus enabling the determination of the tilt of the device. The sensor has a range of 300° . Alternatively, an LED light spot is focused on a CMOS image sensor with $640 \text{ pixel} \times 480 \text{ pixel}$. The position of the light spot on the sensor allows to observe the tilt angle with a resolution of less than 0.07° [34].

Fiber-optic tilt sensors have been widely researched. They offer the advantage of being able to operate in hazardous areas for electrical equipments. However, their readout usually requires expensive and complex equipment, such as an optical spectrum analyzer (OSA). Two general concepts are presented in literature: the first is based on interferometric measurement. The light is guided through a taper in an optical fiber, resulting in an interferometric pattern at the end of the fiber. The pattern is dependent on the bending of the taper, i.e. resulting in a change when the end of the fiber is tilted which allows to infer the tilt angle from the optical measurement [35]. The concept allows for measurement angles of up to $\pm 12^\circ$ [36, 37]. For a measurement with fiber Bragg gratings (FBG) a solid mass is attached to a beam where the deflection of the beam is dependent on the tilt of the structure [38, 39, 40]. Fibers with FBG are attached to the beam and the deflection of the beam leads to strain in the fiber which results in a varying FBG wavelength. Tilt angles of up to 20° are measured with this principle [41].

1.2.2.2 Liquid pendulum

Liquid-based tilt sensors with a resistive measurement principle rely on the use of electrolytes as pendulum. These conductive liquids are placed inside a cavity which has patterned metal electrodes on the substrate surface [42]. By tilting the sensor, the area of the electrodes which is covered by the electrolyte changes, leading to different resistances between the electrodes. The change is then read out with a wheatstone bridge. With a planar design of the cavity, a tilt angle range of $\pm 60^\circ$ is achieved [43]. By introducing electrodes in two dimensions in the cavity, a dual-axis tilt sensor can be realized, achieving an operating angle range of $\pm 70^\circ$ in each axis [44]. The response time of this sensor is around 300 ms. A three dimensional design of the cavity finally even allows a measurement range of 360° in two axes with response times down to 170 ms [45]. Lin et al. use a liquid metal (GaInSn alloy and mercury) as pendulum which connects a circular electrode with a ground electrode. Depending on the position of the pendulum, the resistance of the circular electrode changes, enabling a measurement range of $\pm 150^\circ$.

A fluidic tilt sensor which uses a capacitive measurement was first presented in 2003 by Yotter et al. [46]. Water is filled into cavities above a interdigitated electrode structure. The area of the electrodes covered with water changes with the tilt, resulting in a change in capacitance between the electrodes. This design achieves a response time of 353 ms in the measurement range of $\pm 30^\circ$. Other works present circular cavity designs where a fluid covers parts of the electrodes [47]. At a measurement range of $\pm 60^\circ$ a resolution of 0.4° and a response time of 900 ms is obtained. As fluids, either silicone oil [48] or an oil with dielectric nano-particles [49] are used. Based on the design, the measurement range can go up to $\pm 90^\circ$ [50].

Ferrofluids, i.e. liquids with nanoscale ferromagnetic particles, are used in conjunction with an inductive measurement principle to fabricate a tilt sensor. A cylindrical cavity is filled partially with a ferrofluid and a coil wound around the cavity detects the slope of the liquid surface [51]. Other work uses a drop of a ferrofluid inside a water-filled pipe [52]. A coil around the pipe generates a retaining force and separate sensing coils detect the position of the droplet. Here, the design limits the possible tilt angles to $\pm 20^\circ$ can be measured.

Welch et al. present a tilt sensor where a cavity is partially filled with an opaque liquid while the remaining volume is occupied by an air

bubble [53]. A LED on top of the cavity illuminates four photodetectors on the bottom of the cavity. From the light intensity on the photodiodes which changes with the applied tilt, the tilt angle of the device can be inferred in two axes in a range of $\pm 50^\circ$.

For a fiber optic measurement, two optical fibers are mounted axially symmetric on opposite ends of a cavity filled with a liquid [54]. Light is emitted from one fiber, travels through the liquid and is received by the second fiber. A tilt of the device modifies the transmission path through the cavity filled with liquid and air, thus resulting in a change of the received light intensity. Here, a resolution of 0.02° is achieved. A photonic crystal fiber (PCF) is used by Zhang et al. and immersed in a NaCl solution [55]. Tilt of the fiber changes the length of the fiber immersed in the liquid, resulting in a different transmission spectrum.

1.2.2.3 Gaseous pendulum

Tilt sensors with a gaseous pendulum follow the same principle as thermal accelerometers (see chapter 1.2.1). A resistor heats the volume of a cavity and the resulting thermal profile is measured by several temperature elements [56]. When applying a tilt, the temperature profile changes which allows to infer the tilt angle. This principle allows for measurement angles of up to 360° with a response time of 110 ms [57, 58].

1.3 Contributions

The goal of this work is to design a flexible tilt sensor that can be integrated into textiles. A special focus is put on the selection of materials and fabrication processes. The influence of sensor design parameters is determined by modeling the behavior of the sensor. We want to:

- **design a tilt sensor** that is flexible and can be fabricated with standard clean room processes on plastic,
- **identify materials and fabrication processes** to achieve a low sensor hysteresis considering parasitic forces which hinder the pendulum movement,
- **determine the design parameters** for the sensor, which influence the sensor characteristics, by development of an analytical model,

Table 1.1: Classification of tilt sensor concepts based on pendulum state and measurement principle, and selected highlights with regard to achievable measurement range, resolution and response time.

	Pendulum state				Highlights
	Solid	Liquid	Gaseous		
Resistance	Mescheder et al. [25], Smith et al. [27], Tang et al. [26]	Bin et al. [45], Choi et al. [44, 59], Jung et al. [43], Lee et al. [42], Lin et al. [60]	Billat et al. [57, 58], Courteaud et al. [56]		Measurement range of $\pm 360^\circ$ in two axes [45] Response time of 110 ms [58]
Capacitance	Lee et al. [28, 61], Liang et al. [29], Zhao et al. [30]	Benz et al. [50], Manaf et al. [47], Salvador et al. [48], Ueda et al. [49], Yotter et al. [46]	-		-
Inductance	Olaru et al. [31]	Ando et al. [52], Baltag et al. [51]	-		-
Magnetism	Rovati et al. [32]	-	-		-
Optical	Constandinou et al. [33], Wu et al. [34]	Welch et al. [53]	-		-
Fiber optical	Amaral et al. [35], Bao et al. [41], Dong et al. [39], Frazao et al. [36], Guan et al. [38], Peng et al. [40], Shao et al. [37]	Bajic et al. [54], Zhang et al. [55]	-		Resolution of 0.02° [54]

Measurement principle

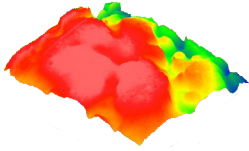
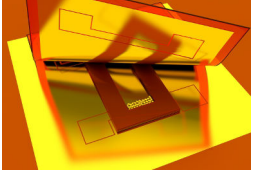
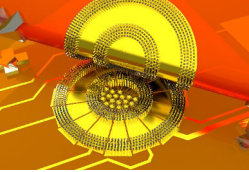
Technology and materials 	Tilt switch 	Tilt sensor 
	Chap. 2: Sensor system	
Chap. 3: Pendulum		
Chap. 4: Cavity		
Chap. 5: Contact mechanics		
		Chap. 6: Sensor modeling
	Chap. 7: Evaluation	

Figure 1.1: Overview of the thesis structure.

- **evaluate the behavior of the pendulum** by analyzing the static and dynamic characteristics of the sensor.

1.4 Thesis outline

In this work, we present the design, modeling and evaluation of a flexible tilt sensor. Our sensor is based on a resistive measurement principle, while conductive microspheres are employed as a pendulum inside the cavity. Standard cleanroom processes are used for fabrication.

The structure of the thesis is given in Fig. 1.1 and is also described in the following:

Chapter 2 introduces the novel sensor principle. The ideas for a tilt switch as well as a tilt sensor are presented and the resulting sensor properties are discussed.

In chapter 3, different types of material as pendulum are evaluated and the pendulum treatment process is given.

Chapter 4 covers the fabrication process of the sensor cavity and the whole sensing structure for two different approaches. The bendability of both approaches is also evaluated.

The effects of the electrical contact between contact pad and pendulum are examined in chapter 5 and the surface roughness with regard to friction and adhesion is analyzed.

The important design parameters for the tilt sensor are evaluated in chapter 6 by creating an analytical model of the sensor. The optimal parameters with respect to the sensor requirements are defined.

The tilt switch and tilt sensor are characterized in chapter 7. First a static evaluation is performed, followed by an analysis of the dynamic microsphere movement in the cavity of the tilt sensor.

Chapter 8 summarizes the findings from this thesis and provides an outlook on further work and possible applications.

1.5 Publications

This thesis is based on the following publications:

- L. Büthe, C. Vogt, L. Petti, G. Cantarella, N. Münzenrieder and G. Tröster. Fabrication, modeling and evaluation of a digital output tilt sensor with conductive microspheres. In *IEEE Sensors Journal*, 2017, submitted.
- L. Büthe, C. Vogt, L. Petti, G. Cantarella, N. Münzenrieder and G. Tröster. Digital output flexible tilt sensor with conductive microspheres. In *Proceedings of the IEEE Sensors 2015*, pages 1–4, 2015.
- L. Büthe, C. Vogt, L. Petti, N. Münzenrieder, C. Zysset, G. Salvatore and G. Tröster. A Mechanically Flexible Tilt Switch On Kapton Foil With Microspheres As A Pendulum. In *Proceedings of Sensors and Measuring Systems 2014; 17. ITG/GMA Symposium*, pages 1–4, 2014.

The following publications have been authored and co-authored additionally:

- L. Büthe, O. Amft, G. Tröster. Textile-integrated sensor technologies for posture and movement detection. In *Context-Aware Systems - Fundamentals and Applications*. Lecture Notes in Computer Science, submitted.

- L. Bütthe, U. Blanke, H. Capkevics, G. Tröster. A wearable sensing system for timing analysis in tennis. In *Proceedings of the 2016 IEEE 13th International Conference on Wearable and Implantable Body Sensor Networks (BSN)*, pages 43–48, 2016.
- N. Münzenrieder, D. Karnaushenko, L. Petti, G. Cantarella, C. Vogt, L. Bütthe, D. D. Karnaushenko, O. G. Schmidt, D. Makarov and G. Tröster. Entirely Flexible On-Site Conditioned Magnetic Sensors. In *Advanced Electronic Materials*, 2(8), page 1600188, 2016.
- L. Petti, N. Münzenrieder, C. Vogt, H. Faber, L. Bütthe, G. Cantarella, T. D. Anthopoulos and G. Tröster. Metal oxide semiconductor thin-film transistors for flexible electronics, In *Applied Physics Review*, 3(2), page 021303, 2016.
- G. Cantarella, N. Münzenrieder, L. Petti, C. Vogt, L. Bütthe, G. A. Salvatore, A. Daus and G. Tröster. Flexible In-Ga-Zn-O Thin-Film Transistors on elastomeric substrate bent to 2.3% strain. In *IEEE Electron Device Letters*, 36(8), pages 781–783, 2015.
- L. Petti, A. Frutiger, N. Münzenrieder, G. A. Salvatore, L. Bütthe, C. Vogt, G. Cantarella and G. Tröster. Flexible Quasi-Vertical In-Ga-Zn-O Thin-Film Transistor with 300 nm Channel Length. In *IEEE Electron Device Letters*, 36(5), pages 475–477, 2015.
- N. Münzenrieder, G. Cantarella, C. Vogt, L. Petti, L. Bütthe, G. A. Salvatore, Y. Fang, R. Andri, Y. Lam, R. Libanori, D. Widner, A. Studart and G. Tröster. Stretchable and Conformable Oxide Thin-Film Electronics. In *Advanced Electronic Materials*, 1(3), page 1400038, 2015.
- N. Münzenrieder, G. A. Salvatore, L. Petti, C. Zysset, L. Bütthe, C. Vogt, G. Cantarella and G. Tröster. Contact resistance and overlapping capacitance in flexible sub-micron long oxide thin-film transistors for above 100 MHz operation. In *Applied Physics Letters*, 105(26), page 263504, 2014.
- L. Petti, N. Münzenrieder, G. A. Salvatore, C. Zysset, T. Kinkeldei, L. Bütthe, C. Vogt and G. Tröster. Flexible electronics based on oxide semiconductors. In *2014 21st International Workshop on Active-Matrix Flatpanel Displays and Devices (AM-FPD)*, pages 323–326, 2014.

- N. Münzenrieder, P. Voser, L. Petti, C. Zysset, L. Büthe, C. Vogt, G. A. Salvatore and G. Tröster. Flexible Self-Aligned Double-Gate IGZO TFT. In *IEEE Electron Device Letters*, 35(1), pages 69–71, 2014.
- L. Petti, N. Münzenrieder, G. A. Salvatore, C. Zysset, T. Kinkeldei, L. Büthe and G. Tröster. Influence of Mechanical Bending on Flexible InGaZnO-Based Ferroelectric Memory TFTs. In *IEEE Transactions on Electron Devices*, 61(4), pages 1085–1092.
- L. Petti, F. Bottacchi, N. Münzenrieder, H. Faber, G. Cantarella, C. Vogt, L. Büthe, I. Namal, F. Spath, T. Hertel, T. D. Anthopoulos and G. Tröster. Integration of solution-processed (7,5) SWCNTs with sputtered and spray-coated metal oxides for flexible complementary inverters. In *2014 IEEE International Electron Devices Meeting (IEDM)*. pages 610–613, 2014.
- L. Büthe, M. Hardegger, P. Brülisauer and G. Tröster. RFID-Die: Battery-free Orientation Sensing Using an Array of Passive Tilt Switches. In *Proceedings of the 2014 ACM International Joint Conference on Pervasive and Ubiquitous Computing: Adjunct Publication*, pages 215–218, 2014.
- G. A. Salvatore, N. Münzenrieder, T. Kinkeldei, L. Petti, C. Zysset, I. Strebel, L. Büthe and G. Tröster. Wafer-scale design of lightweight and transparent electronics that wraps around hair. In *Nature Communications*, 5(2982), pages 1–8, 2014.
- G. A. Salvatore, N. Münzenrieder, C. Barraud, L. Petti, C. Zysset, L. Büthe, K. Ensslin and G. Tröster. Fabrication and Transfer of Flexible Few-Layers MoS₂ Thin Film Transistors to Any Arbitrary Substrate. In *ACS Nano*, 7(10), pages 8809–8815, 2013.
- C. Zysset, N. Münzenrieder, L. Petti, L. Büthe, G. A. Salvatore and G. Tröster. IGZO TFT-Based All-Enhancement Operational Amplifier Bent to a Radius of 5 mm. In *IEEE Electron Device Letters*, 34(11), pages 1394–1396, 2013.
- N. Münzenrieder, G. A. Salvatore, T. Kinkeldei, L. Petti, C. Zysset, L. Büthe and G. Tröster. InGaZnO TFTs on a Flexible Membrane Transferred to a Curved Surface with a Radius of 2 mm. In *2013 71st Annual Device Research Conference (DRC)*, pages 165–166, 2013.

- N. Münzenrieder, L. Petti, C. Zysset, D. Görk, L. Büthe, G. A. Salvatore and G. Tröster. Investigation of gate material ductility enables flexible a-IGZO TFTs bendable to a radius of 1.7 mm. In *43rd European Solid-State Device Research Conference (ESSDERC13)*, pages 362–365, 2013.
- L. Petti, P. Aguirre, N. Münzenrieder, G. A. Salvatore, C. Zysset, A. Frutiger, L. Büthe, C. Vogt and G. Tröster. Mechanically flexible vertically integrated a-IGZO thin-film transistors with 500 nm channel length fabricated on free standing plastic foil. In *2013 IEEE International Electron Devices Meeting (IEDM)*, pages 296–299, 2013.
- C. Zysset, N. Nasser, L. Büthe, N. Münzenrieder, T. Kinkeldei, L. Petti, S. Kleiser, G. A. Salvatore, M. Wolf and G. Tröster. Textile integrated sensors and actuators for near-infrared spectroscopy. In *Optics Express*, 21(3), pages 3213–3224, 2013.
- S. Jalaliniya, J. Smith, M. Sousa, L. Büthe and T. Pederson. Touchless Interaction with Medical Images Using Hand & Foot Gestures. In *Proceedings of the 2013 ACM Conference on Pervasive and Ubiquitous Computing: Adjunct Publication*, pages 1265–1274, 2013.

2

Sensor system

We introduce the general sensing principle. Two different design architectures are described which will be evaluated in more detail in the following chapters. Finally, the sensor properties which are achievable with the architectures are reported.

2.1 Sensing principle

In contrast to many other tilt sensor approaches as described in chapter 1.2, the proposed tilt sensing principle does not supply continuous output values. Instead, we present a tilt sensing principle where discrete contact elements are shorted with the pendulum, either with each other or towards a ground plane. As shown in Fig. 2.1, the short circuit of each contact element can be detected by a resistance measurement. This requires only an ohmmeter and a multiplexer. Based on a resistance threshold value, the connection is then evaluated as either open (0) or closed (1). With this information and a corresponding look-up table, the static orientation of the tilt sensor can be determined.

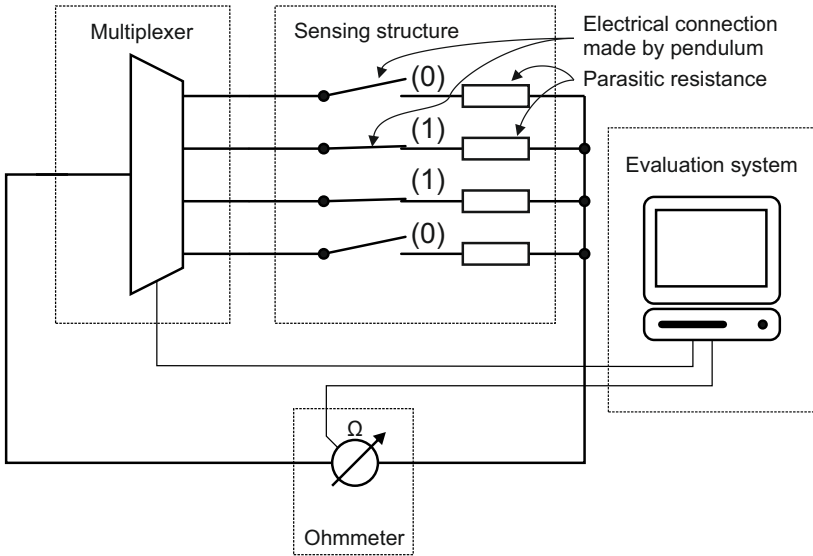


Figure 2.1: Overview of the sensing principle.

By selecting the resistance threshold value appropriately, the sensor becomes largely independent of parasitic resistances or capacitances. It does not require the evaluation electronics close to the sensor cavity, instead they can be "far away", i.e. several meters of connection lines are possible. Changes to the connection lines such as bending or stretching, which shift the resistance of these lines, will not influence the sensor orientation measurement, as the sensor output is digital.

2.2 Design and architecture

Based on the previously described sensing principle, we propose two different types of tilt sensing architectures:

- **Tilt switch:** A tilt switch is a switch with two states, i.e. open when tilted in one direction with respect to horizontal, and closed when tilted in the other direction.
- **Tilt sensor:** The tilt sensor measures the tilt of the device with a certain angular resolution.

As a pendulum conductive microspheres are used which will be discussed in more detail in chapter 3. Both sensing architectures have their advantages and disadvantages, especially with regard to resolution and complexity, and will be discussed in the following sections.

2.2.1 Tilt switch

The schematic design of the tilt switch is shown in Fig. 2.2. On each side of the cavity two contact pads are located. The pendulum inside the cavity boundaries follows the orientation of gravity and connects two adjacent contact pads. This indicates the orientation of the device, i.e. whether the sensor is tilted to the right side (Fig. 2.2b, d) or to the left side (Fig. 2.2c, e). The state of two contact pads is either *active* when they are connected by the pendulum or *inactive* when no electrical connection is made. By evaluating this state, the electrical representation of the sensor (Fig. 2.2f, g) and subsequently its orientation can be determined. The rectangular shape of the cavity ensures that the pendulum can only lie at the end of the cavity where the contact pads are located.

The tilt switch can only detect tilt changes along the axis as indicated in Fig. 2.2b. Other tilt of the sensor cannot reliably be detected by the proposed concept.

In case the sensor is held horizontally, the microspheres can spread at random over the area of the cavity. Thus, designing the sensor with contact pads on either side of the cavity, this state can be detected as well as both contacts on either side will not be in electrical contact.

This architecture is especially useful in scenarios where only knowledge about the direction of tilt of the device is required.

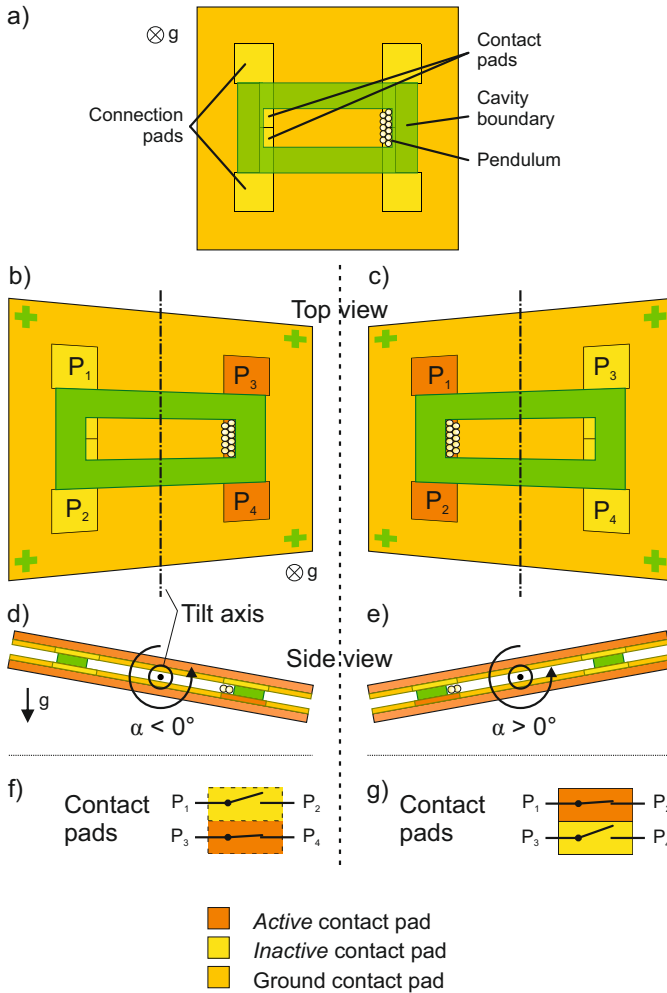


Figure 2.2: Top view of tilt switch architecture (a). Active contact pads when tilted right (b), (d) as well as tilted left (c), (e) with the corresponding electrical representation (f) and (g), respectively.

2.2.2 Tilt sensor¹

Fig. 2.3 depicts the architecture of the tilt sensor which consists of circularly arranged contact pads. Exemplarily, a tilt sensor with four contact pads is shown.

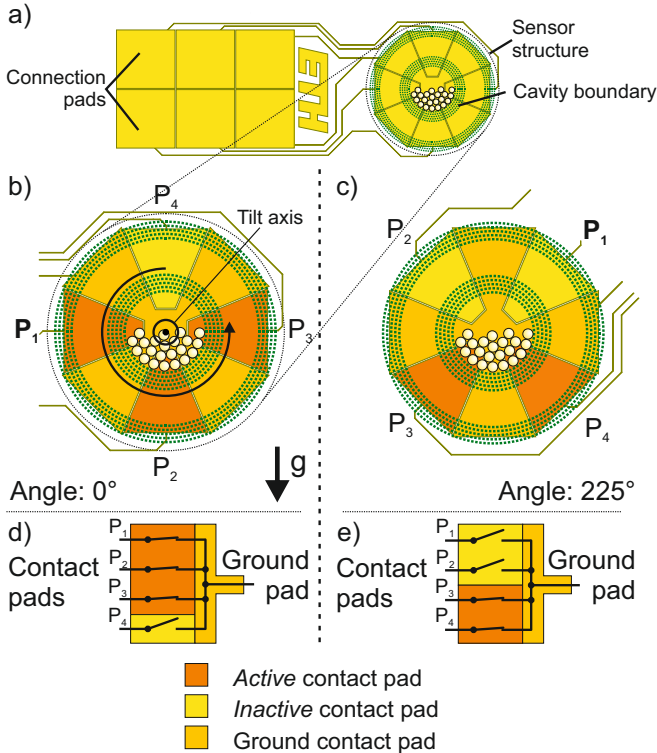


Figure 2.3: Top view of tilt sensor architecture (a). Sensing principle of tilt sensor: Active contact pads at a tilt of 0° (b) and 135° (c) with the corresponding electrical representation (d) and (e), respectively.

The cavity, visualized in green, is of circular shape. The inner ring of the cavity defines the movement area of the microspheres, whereas the outer ring is used for sealing of the cavity with adhesive (see chapter 4.2). A ground pad fills the area between the contact pads. The coverage of the substrate surface with a conductive layer is necessary

¹This section is based on [62] © 2015 IEEE

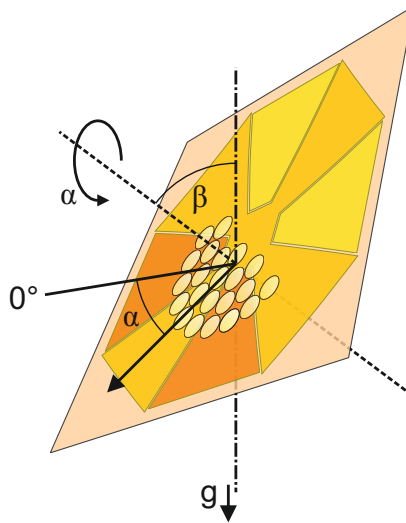


Figure 2.4: Schematic of the tilt sensor with identification of two tilt angles.

in order to mitigate electrostatic charges which might build up on the underlying substrate during the fabrication process and will influence the movement of the pendulum. Different styles of contact pads are also possible and will be evaluated along with other parameters in chapter 6.

Depending on the orientation of the sensor structure with respect to gravity, the conductive microspheres create an electrical connection between the ground pad and the respective contact pads (Fig. 2.3b, c). These connected pads are defined as *active* (1), whereas the other pads remain *inactive* (0) and have no electrical connection to ground. By measuring the resistance between the ground pad and each contact pad, a readout of the sensor can be achieved, leading to a digital output signal. The sensor can be simplified in a corresponding electrical representation where each connection between a contact pad and the ground pad is exemplified by a switch which is either closed (*active*) or open (*inactive*) (Fig. 2.3d, e).

The orientation of the tilt sensor is described by two angles according to Fig. 2.4. The tilt of the normal of the sensor plane with regard to vertical is measured by the angle β . At $\beta = 0^\circ$, the sensor plane is

Table 2.1: Possible steady states (0: *inactive* contact pad; 1: *active* contact pad) of a 4-contact tilt sensor (cavity area covered by 50% with the pendulum) with the corresponding output angle based on Fig. 2.3b.

State of contact				Angle	
P ₁	P ₂	P ₃	P ₄	Sensor orientation	Sensor output
1	1	1	0	-22.5° (337.5°) to 22.5°	0°
0	1	1	0	22.5° to 67.5°	45°
0	1	1	1	67.5° to 112.5°	90°
0	0	1	1	112.5° to 157.5°	135°
1	0	1	1	157.5° to 202.5°	180°
1	0	0	1	202.5° to 247.5°	225°
1	1	0	1	247.5° to 292.5°	270°
1	1	0	0	292.5° to 337.5°	315°

horizontal and the microspheres spread randomly across the cavity area. Only for $\beta > 0^\circ$, the microspheres roll towards an edge of the cavity and create an electrical contact between contact pads and the ground pad.

The presented architecture can only detect tilt as a rotation around the axis perpendicular to the sensor plane. This rotation around the axis depicted in Fig. 2.4 is defined as α which is the measurement value of the sensor. Other tilt cannot reliably be detected by the tilt sensor.

The tilt sensor should also not be operated in a scenario where the sensor plane is horizontal, as this will cause the pendulum to randomly spread over the cavity area without activating the contact pads.

Once the electrical representation of the tilt sensor in a certain steady state has been established, a look-up table allows to infer the current tilt. Such a table is given in Table 2.1 for a 4-contact tilt sensor where the cavity area is covered by half with the pendulum. The modeling of the tilt sensor in chapter 6 will provide more insight into the influence of the different design parameters of the tilt sensor.

2.3 Sensor properties

With the previously described tilt sensing designs, several sensor properties can be achieved:

- **Mechanical properties and dimensions**

As the tilt sensor is intended for use in wearable devices, the sensor should be bendable without losing its functionality. We will demonstrate the bendability in chapter 4 while chapter 7 examines the functionality after bending of the device.

The proposed concepts allow the fabrication of a flat sensor where the thickness of the device is limited by the diameter of the microspheres which are used as the pendulum. Chapter 4 will demonstrate that this allows to build sensors that do not exceed the dimensions of current state-of-the-art MEMS tilt sensors which have a diameter of around 5 mm including the packaging.

- **Sensor readout**

The sensing principle enables a sensor readout that does not require sophisticated electronics, such as amplifiers, etc. close to the sensor. Instead the readout electronics can be located at a central distant location within a smart textile [63] while parasitic influences, e.g from the connection lines, do not influence the digital output signal.

- **Materials and technology**

In chapter 4 we will show the fabrication of the sensors on free-standing foil. Therefore we enable the assembly of devices such as electronics [64] or sensors [65] in one process flow with the tilt sensor. This would allow the integration of several other sensors, such as strain or temperature sensors, or even small circuits [66] to create smart sensor nodes on plastic.

2.4 Conclusion

Two different architectures based on the proposed tilt sensing principle have been presented with their basic operating principle. A tilt switch can detect the orientation of the tilt without allowing to infer the tilt angle. To gain insight into the applied tilt angle, the second approach

for a tilt sensor needs to be applied. This architecture will be modeled in chapter 6.

3

Pendulum

The material choice of the pendulum is discussed and several options are compared. We select solder spheres as the final choice for the pendulum and describe how the surface conductivity is increased by coating with gold.

3.1 Material selection

The pendulum is the part of the sensor which follows the direction of gravity inside the cavity and creates a change in the output signal of the sensor. Although the sensing principle in the previous chapter 2 is explained with the use of solid microspheres, different types of materials are possible for the proposed system. In general solids in the form of microspheres as well as liquids are qualified for this, while gaseous elements are discarded as they would not be able to create an electrical connection.

A solid or liquid pendulum also needs to fulfill the following criteria to be suitable for our tilt sensor:

- *Conductivity*: The material should be electrically conductive, i.e. resulting in a resistance in the range of $k\Omega$ or less so that the electrical connection between the contact pads can be clearly identified.
- *Density*: A larger density of the used material ensures that the gravitational field dominates the movement of the pendulum compared to other parasitic forces.

In addition, liquids have also additional requirements to conform with:

- *Surface tension*: The surface tension γ_{lv} of the liquids should be high to ensure a high contact angle θ which is represented by the following relation: $\cos(\theta) \sim -\gamma_{lv}$. This results in a low wetting on the substrate surface which is desirable to keep the contact area small and have low adhesion forces between the pendulum and the substrate (see chapter 5).
- *Vapor pressure*: The vapor pressure which is an indicator for a liquid's evaporation rate should be preferably low. This ensures that the material inside the cavity does not convert to the gaseous phase.
- *Viscosity*: The viscosity of the liquid, a measure of the resistance to deformation, should be low to ensure a good response time of the sensor.

A solid pendulum needs to show a high uniformity and roundness of the microspheres to ensure a free pendulum movement inside the cavity.

3.1.1 Liquids

As liquids, we have identified ionic liquids (IL) as the most promising category. IL are salts in a liquid state. Usually salts, such as NaCl, have high melting temperatures high above room temperature, but there also exist salts which are liquid at room temperature and are now in the focus of various research areas [67, 68, 69]. As they contain ions, they are electrically conductive and have been used as conducting fluids for different applications [70, 71]. They also exhibit a low vapor pressure [72, 73] as a consequence of their ionic nature.

The sensor design requires the pendulum to create an electrical connection between different areas on the substrate surface, i.e. the contact pads and the ground pad. This requires the pendulum to have several contact points with the substrate surface. A liquid pendulum that consists of several, individual spherically shaped elements would unite to a single, larger element. This single pendulum would have a contact area with the substrate surface which covers the contact pads and ground pad, compared to several, small contact points of each pendulum element. The contact area leads to increased adhesion forces of the pendulum with the substrate which decrease the performance of the sensor.

In addition, the design of the sensor aims for a height of the cavity which is less than 1 mm, a domain where the capillary effect has an influence on a liquid pendulum. The height h of a liquid column with the density ρ_l in a tube with the radius r is given as [74]

$$h = \frac{2\gamma_{lv}\cos(\theta)}{\rho_l g r}. \quad (3.1)$$

A reduced height of the cavity which relates to a reduced tube radius r leads to an increased capillary height h which indicates high capillary forces. These capillary forces which act against the gravitational forces influence the movement of the pendulum inside the cavity.

The surface tension also has an influence on the response time. Bin et al. [45] demonstrate that a reduction of the cavity size from 10 mm to 6 mm increases the response time from 0.17 s to 0.65 s which is caused by the liquid's surface tension. The response time, a measure for the time from when a tilt is applied until the correct output signal is achieved, should be minimal to allow a fast adaptation of the tilt sensor to new input angle values. The viscosity of IL is also larger than other electrically conductive liquids [75], thus rendering IL not suitable for achieving a low response time of the tilt sensor.

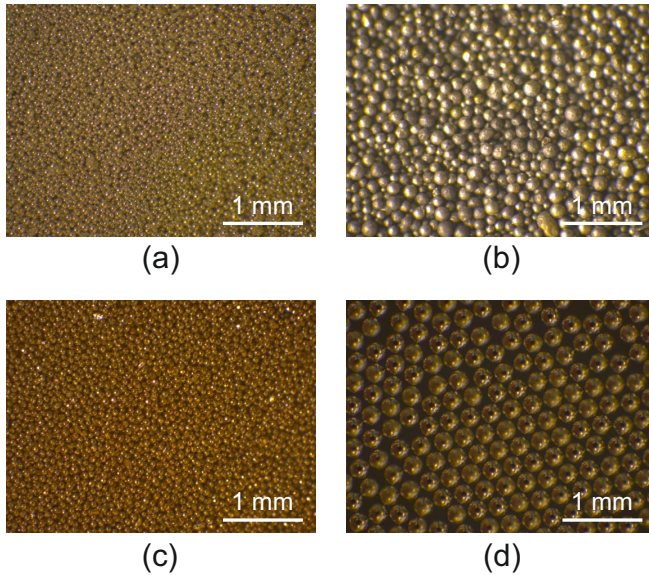


Figure 3.1: Microscope images of different spheres: (a) Hollow glass spheres coated with silver; (b) Cast steel; (c) Tin-bronze alloy; (d) Tin-silver-copper solder spheres.

Based on the previously listed requirements, we conclude that ionic liquids are not appropriate for the use as pendulum in the proposed tilt sensor.

3.1.2 Solids

A solid pendulum can either consist of a solid conductive material or of non-conductive spheres which are coated with a conductive material. Examples for the former are hollow glass microspheres coated with silver [76] as they are used in conductive paint (Fig. 3.1a). However, these hollow spheres have a density of only 0.16 g cm^{-3} .

The alternative is to use a single solid material as pendulum. Microspheres such as spheres from cast steel used for shot blasting [77] vary significantly in size and also do not exhibit a good roundness (Fig. 3.1b). However, a homogeneous size and good roundness are crucial for a repeatable movement of the pendulum in the cavity. These observa-

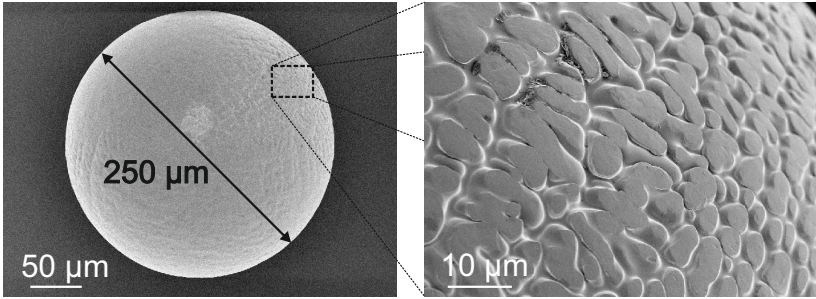


Figure 3.2: SEM picture of a solder sphere with a diameter of 250 μm .

tions also apply to tin bronze spheres used in the imaging of fluids in a flow channel [78] (Fig. 3.1c).

Solder spheres, however, fulfill the previously listed criteria and are commercially available. Usually used for soldering of ball grid arrays [79], they have also been employed in a variety of other applications, such as sensing for a single-use OFF-ON switch [80]. Current solder spheres are lead free and consist of a tin-silver-copper alloy (Fig. 3.1d).

Here, we use solder spheres of the type *Profound Material SAC305* which are composed of 96.5 % tin (Sn), 3 % silver (Ag) and 0.5 % copper (Cu) [81]. The available diameters range from 60 μm up to 889 μm . We choose a size of 250 μm which will enable a flat design of the tilt sensor, while allowing for a microsphere size which can be manually handled during the fabrication process. The spheres have a high uniformity in size ($\pm 10 \mu\text{m}$) as well as a high specific weight (7.4 g cm^{-3}) compared to other conductive microspheres such as coated hollow glass spheres [82].

Fig. 3.2 shows a scanning electron microscopy (SEM) image of one solder sphere with a closeup of the sphere surface. The microsphere has a sphericity with a tolerance of less than 1.5 %. It is visible from the image, especially the inset, that the surface of the microsphere is not smooth, but has a roughness with a depth of around 1 μm and size of several μm . This roughness originates from the fabrication process of the solder spheres [83, 84]. The microspheres are produced by uniform droplet spraying where liquid solder tin is sprayed through an orifice and the spheres are cooled in free fall in a gas environment. During the free fall, the air flow around the microspheres creates turbulences

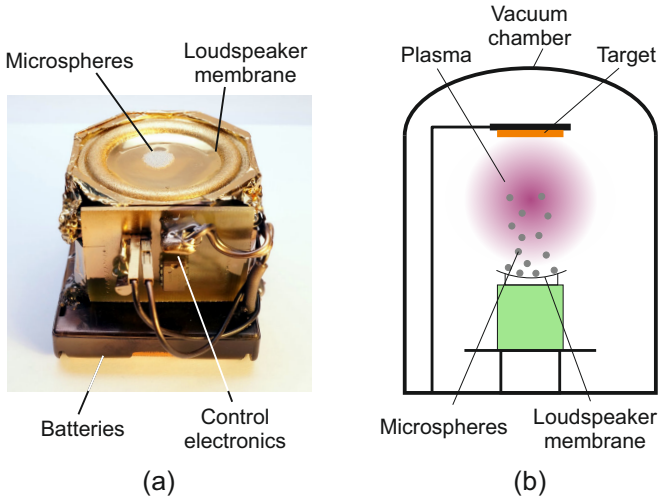


Figure 3.3: (a) Photograph of the custom-made vibration device with microspheres on the loudspeaker membrane; (b) Schematic of vibration device inside vacuum chamber of sputter tool.

which lead to the rough microsphere surface. In chapter 5, the surface roughness and its influence on adhesion forces and contact resistance will be explored in more detail.

3.2 Pendulum preparation

Prior to their use in the tilt sensor, the microspheres are coated. During the fabrication process, the solder spheres are kept under inert nitrogen atmosphere [85], to prevent oxidation of the solder alloy. However, as the assembly of the tilt sensor is performed in normal atmosphere, the solder spheres come into contact with oxygen and form an oxidation layer on their surface. This oxidation layer prevents the solder spheres from forming an electrical contact which would not allow to apply the proposed tilt sensing principle.

Therefore, we use gold to increase the surface conductivity of the microspheres. The microspheres are first sputtered with nickel which acts as an adhesion layer and subsequently with gold. During the sputter process the spheres are kept agitated in order to achieve a uniform coating over the whole surface area of the spheres. The spheres are

placed on a loudspeaker membrane which acts as a vibration device as shown in Fig. 3.3a and is oscillating at a frequency of 150 Hz, keeping the spheres agitated during the sputter process. A battery supply allows the operation of the device inside the sputter vacuum chamber (Fig. 3.3b). We deposit nickel at a rate of 1 nm/ min for 2 min and gold at a rate of 16 nm/ min for 4 min, achieving coating thicknesses of 3 nm and 16 nm, respectively. In chapter 5, we evaluate the resulting resistance of the coated microsphere with the substrate surface.

3.3 Conclusion

We introduced the requirements for the pendulum, followed by a discussion on different pendulum materials. Liquids are not a suitable material for a pendulum, solids are advantageous. Several sphere types were evaluated, but could not be considered due to the lack of homogeneity over all spheres and the sphericity of a single sphere. Solder spheres are selected as the best choice as a pendulum and coated uniformly to mitigate surface oxidation.

4

Cavity

We present two different fabrication processes for the cavity and the complete tilt switch and tilt sensor. Both approaches are compared with each other and evaluated for the bendability of the cavity.

The cavity defines the boundaries of the volume in which the pendulum can move freely across the contact pads. In addition, the cavity has to enable the bendability of the sensor without hindering the pendulum in its movement inside the cavity. As the sensor is fabricated on polyimide foil, the processing temperatures should not exceed 200 °C.

As possible applications (see chapter 8.4.2) require not only regular shaped cavities such as square or round, but also other cavity shapes, the fabrication process should allow for these designs. With photolithographic processing arbitrary layouts of cavity can be imagined while also allowing for high resolution in the μm -range.

Metz et al. present the fabrication of flexible cavities with the use of polyimide as well as SU-8 [86, 87]. Based on this, we will present two different approaches for fabrication of a flexible cavity, differing in the way how the side walls are created:

1. **Stacking of polyimide layers:** Layers of polyimide are structured and then stacked upon each other to reach the desired thickness.
2. **SU-8 pillars:** Pillars of SU-8 define the layout of the cavity.

The following sections will present the fabrication steps and discuss the bendability with a focus on the second approach with SU-8 pillars.

4.1 Stacking of polyimide layers¹

For this approach, several structured layers of polyimide foil are stacked upon each other forming the cavity. This allows to tailor the height of the cavity in multiples of the polyimide foil thickness. Here, we use *Kapton E* (DuPont) with a thickness of 50 μm .

4.1.1 Fabrication process

The fabrication process is shown in Fig. 4.1. First, e-beam evaporation is used to deposit 10 nm of chrome (Cr) and 60 nm of gold (Au) on the polyimide foil (Fig. 4.1a). The chrome acts as an adhesion layer between the polyimide and the gold layer. Gold is used as electrode material as it is conductive without oxidizing. Both metal layers are

¹This section is based on "Sensoren und Messsysteme 2014, ITG-Fachbericht 250, Beiträge der 17. ITG/GMA-Fachtagung vom 3. bis 4. Juni 2014, Beitrag 36: L. Bütke u.a., A Mechanically Flexible Tilt Switch on Kapton Foil with Microspheres as a Pendulum", VDE VERLAG, Berlin, Offenbach, 2014. [88]

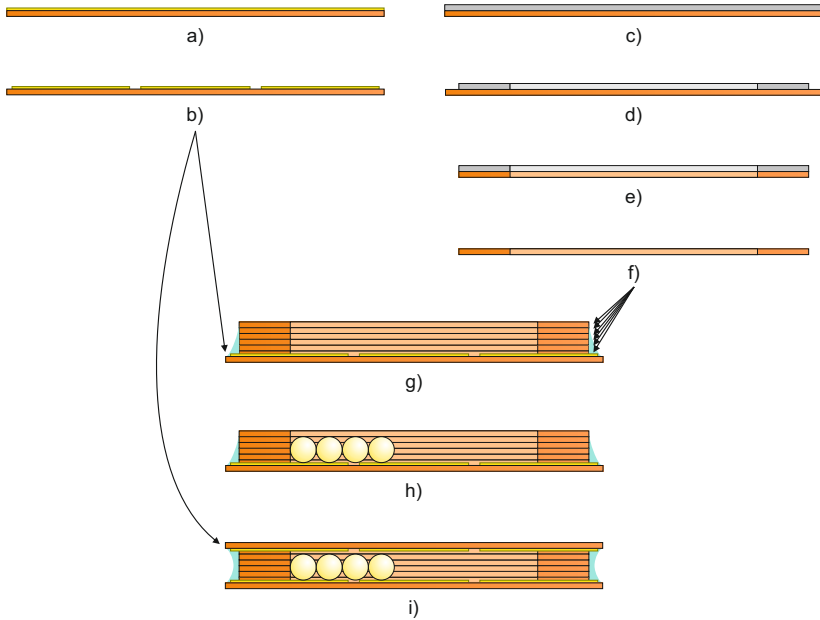


Figure 4.1: Fabrication of layered cavity: a) E-beam evaporation of Cr/Au on polyimide; b) Structuring of Cr/Au by wet etching; c) Sputter deposition of Al on polyimide; d) Structuring of Al hard mask by wet etching; e) Dry etching of polyimide; f) Removal of Al mask by wet etching; g) Glueing of several etched polyimide sheets onto polyimide with metal contacts; h) Placement of microspheres; i) Closing of cavity by glueing.

structured by wet etching to form the electrical contacts of the sensor (Fig. 4.1b). The patterned polyimide foil acts as a substrate for the following cavity fabrication.

For the side walls of the cavity, a stack of several 50 μm -thick polyimide foils is used. A layer of polyimide is coated with 200 nm of sputtered aluminum (Al) (Fig. 4.1c) which is subsequently patterned by photolithography and wet etching (Fig. 4.1d). The structured aluminum serves as a hard mask during the following structuring of the polyimide in a dry etching process (Fig. 4.1e). Dry etching is performed in an Oxford Plasmalab reactive ion etching (RIE) system running a SF_6/O_2 plasma at 300 W, 700 μbar , and 100 sccm flow for 40 min [89].

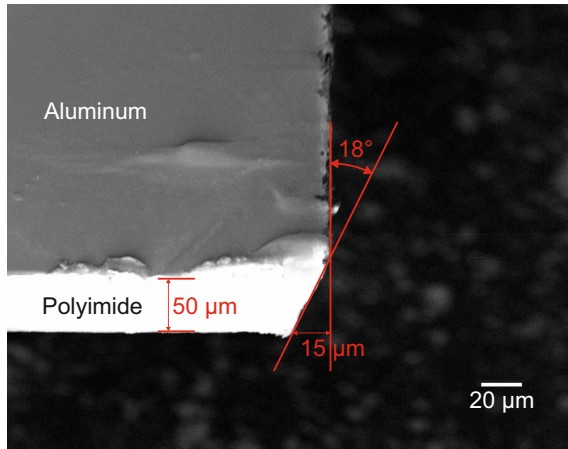


Figure 4.2: SEM picture of the edge of a layer of polyimide coated with aluminum, structured with reactive ion etching. The sample is tilted by 30°.

Finally, the remaining aluminum is removed by wet etching (Fig. 4.1f).

Fig. 4.2 shows an SEM picture of the edge of the structured polyimide foil before removal of the aluminum layer. Reactive ion etching is a predominately anisotropic process, but the angle of the edge of around 18 degree indicates also some isotropic etching. This isotropy needs to be taken into account during the design of the sensor and the dimensions of the cavity.

Subsequently the structured layers of polyimide are stacked upon each other to form a cavity with the desired height. As described in chapter 3, the microspheres used as a pendulum have a diameter of 250 μm. To allow for a free movement of the microspheres with a minimal clearance, six layers are used for the fabrication of the cavity. The sheets are aligned on top of each other and glued together with epoxy glue (EPO-TEK 301-2). The stack is mounted on top of the previously prepared Kapton substrate with the metal contacts (Fig. 4.1g). Afterwards the cavity is loaded with the desired amount of microspheres (Fig. 4.1h). The cavity is closed and sealed with a second patterned polyimide substrate with the same contacts as the first sheet (Fig. 4.1i). Fig. 4.3 shows a photograph of a cavity loaded with the microspheres before the final closing with the second substrate layer.

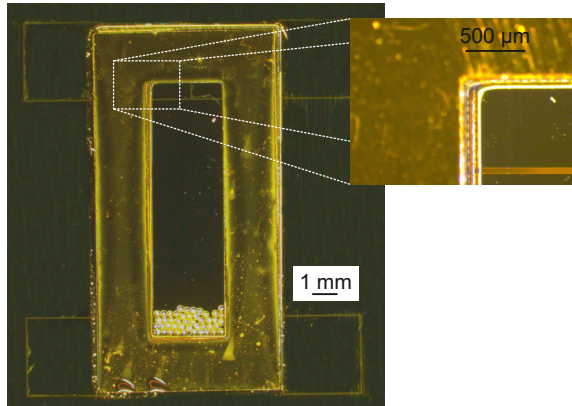


Figure 4.3: Macroscopic picture of a fabricated tilt switch by stacking of polyimide layers. The inset shows the misalignment of the polyimide layers.

The fabrication of the cavity with structured polyimide foil offers several advantages: the definition of the cavity with the help of photolithography is possible with standard clean room processes and allows for various possible cavity layout designs. Although we only show the tilt switch cavity fabricated by a stack of polyimide layers, the fabrication process can also be used to make a tilt sensor based on the principle described in chapter 2.2.2. In addition, the height of the cavity can be adapted by selecting the corresponding amount of layers in the stack. However, the alignment of the layer stack is challenging as several layers need to be aligned on top of each other, thus is more prone for imprecisions (see inset of Fig. 4.3).

4.1.2 Bendability

We examine the bendability of the cavity which is fabricated by stacking several layers of polyimide. The use of polyimide allows for a flexibility of the whole device. Nevertheless, the total height of the device of $400\ \mu\text{m}$ and the limited adhesion by glueing restrict the bendability. The substrate with the cavity is firmly attached to double-sided adhesive tape which is subsequently attached to objects with different radii. The cavity remains intact down to a bending radius of $r_{\text{bend}} = 5\ \text{cm}$, shown in Fig. 4.4. As it will be demonstrated in chapter 7.1, the functionality

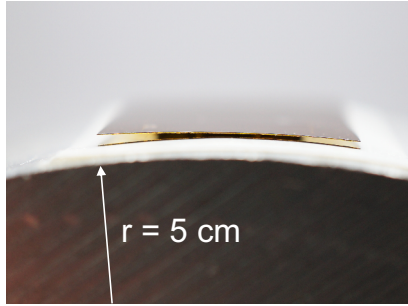


Figure 4.4: Photograph of cavity fabricated with a stack of polyimide layers, bent to a radius of 5 cm along the long side of the cavity.

of the sensor is also still guaranteed after re-flattening. The bending radius of 5 cm corresponds to a maximum compressive and tensile strain of (see appendix, Eq. A.6)

$$\epsilon = \frac{h}{2r_{bend}} = 0.4\% \quad (4.1)$$

with $h = 400 \mu\text{m}$ as the overall height of the sensor. Bending of other electronic devices has also demonstrated similar strain values as a limit, such as e.g. in TFTs [64]. However, these devices have a lower height of only $50 \mu\text{m}$ which allows the achievement of lower bending radii.

In case the bending radius is decreased further, the strain in the cavity exceeds the maximum possible strain. The resulting shear and tensile forces exceed the strength of the epoxy glue, resulting in a delamination of the glued polyimide layers from the substrate, rendering the cavity non-functional.

4.2 SU-8 cavity²

The sensor cavity can also be fabricated by structuring SU-8 pillars on the polyimide substrate with the contact pads. SU-8 is a negative photoresist, developed by IBM, which enables a broad range of thicknesses from less than $1 \mu\text{m}$ up to $450 \mu\text{m}$ [90]. The resist is exposed with

²This section is based on [62] © 2015 IEEE

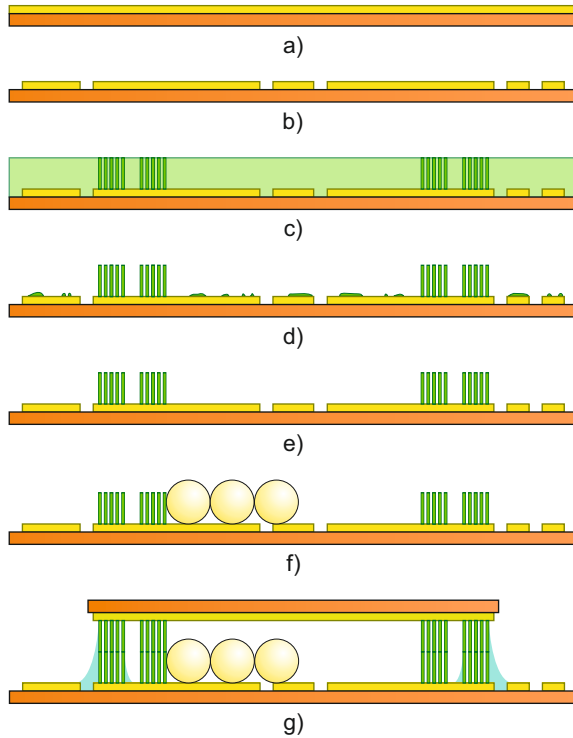


Figure 4.5: Fabrication of SU-8 pillar cavity: a) E-beam evaporation of Cr/Au on polyimide; b) Structuring of Cr/Au by wet etching; c) SU-8 spin coating (height: $150\ \mu\text{m}$) and UV exposure; d) Development of SU-8; e) Reactive ion etching; f) Placement of microspheres; g) Closing of cavity and glueing.

a standard UV mask aligner; aspect ratios of more than 18 are achievable [91]. The pillar design is necessary to balance arising strain on the flexible substrate due to different thermal expansion coefficients α_T of SU-8 and polyimide ($\alpha_{T,SU-8} = 52 \times 10^{-6}\ \text{K}^{-1}$, $\alpha_{T,PI} = 16 \times 10^{-6}\ \text{K}^{-1}$). It also allows for an increased bendability of the cavity.

4.2.1 Fabrication process

The fabrication process is depicted in Fig. 4.5. As a substrate, a $50\ \mu\text{m}$ -thick polyimide foil, Kapton E from *DuPont*, is used. First, via e-beam

evaporation a layer of 10 nm of chrome is deposited, followed by 60 nm of gold. The chrome is an adhesion layer between the polyimide and the gold layer while the gold layer itself acts as the conductive electrode material. The two metal layers are structured by wet etching and form the contact pads of the sensor (Fig. 4.5a).

Subsequently, *SU-8 2100* is spin coated with a thickness of 150 μm onto the substrate and structured via photolithography with UV light (Fig. 4.5b). With *mr-Dev 600*, the SU-8 is developed, resulting in the desired cavity structure (Fig. 4.5c). Reactive ion etching (RIE) with an O_2 -plasma is performed to remove remaining residue (Fig. 4.5d); this is described in more detail in chapter 4.2.1.3. The resulting cavity is then filled with the microspheres (Fig. 4.5e).

To close the cavity, a second sheet of polyimide foil with a chrome/gold layer and SU-8 pillars is placed upside down on the top of the structure and finally sealed with epoxy glue (EPO-TEK 301-2) (Fig. 4.5f).

4.2.1.1 Pillar dimensions

The dimensions of the SU-8 pillars are evaluated to identify the ideal edge length c_{pillar} as well as spacing c_{dist} for the given height of 150 μm with regard to bendability and fabrication yield.

- **Pillar edge length:** For a low stiffness and thus a high bendability of the sensor cavity, the edge length of the pillars should be as small as possible. The bending stiffness is defined as the product of the Young's Modulus E and the respective second moment of area I . The bending stiffness of polyimide foil with a thickness $h_{PI} = 50 \mu\text{m}$ and the Young's Modulus $E_{PI} = 5.5 \text{ GPa}$, normalized to its width w , is defined as

$$E_{PI} \cdot \frac{I_{PI}}{w} = E_{PI} \cdot \frac{wh_{PI}^3}{12w} = 5.73 \times 10^{-5} \text{ N}. \quad (4.2)$$

For a polyimide foil coated with 150 μm SU-8 and a Young's Modulus of $E_{SU-8} = 4.95 \text{ GPa}$ [92], the stiffness is at

$$E_{SU-8} \cdot \frac{I_{pillar}}{w} = E_{SU-8} \cdot \frac{w(h_{PI} + h_{SU-8})^3}{12w} = 3.67 \times 10^{-3} \text{ N}. \quad (4.3)$$

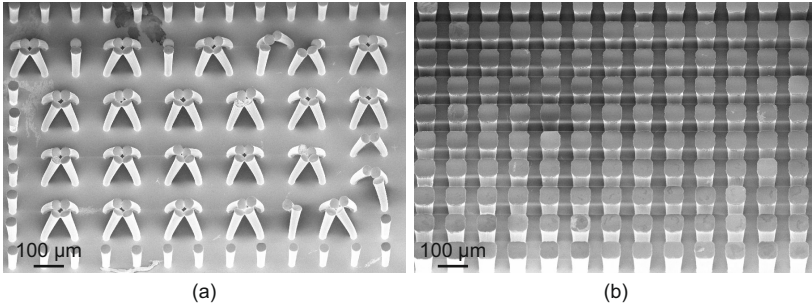


Figure 4.6: Array of SU-8 pillars with edge length of 40 μm (a) and 60 μm (b); the periodicity is 100 μm in both cases.

The overall stiffness is composed proportionally of the two stiffnesses:

$$\left(\frac{EI}{w}\right)_{all} = \frac{c_{dist}}{c_{pillar} + c_{dist}} \cdot \frac{E_{PI}I_{PI}}{w} + \frac{c_{pillar}}{c_{pillar} + c_{dist}} \cdot \frac{E_{SU-8}I_{pillar}}{w} \quad (4.4)$$

The bending stiffness of SU-8 coated polyimide foil is two orders of magnitude higher than the bare polyimide foil. Therefore, according to Eq. 4.4, a decreased edge length of the pillars c_{pillar} decreases the stiffness of the cavity. However, decreasing the edge length of the pillars reduces adhesion to the substrate surface. As the flexibility of the polyimide substrate along with the gold surface reduces the adhesion of SU-8 on the substrate surface [93], a balance is required. Experiments show that a pillar edge length of 40 μm leads to collapsed pillar structures during the fabrication process (see Fig. 4.6a) while an edge length of 60 μm is sufficient to achieve a good fabrication yield (see Fig. 4.6b).

- **Pillar spacing:** The spacing of the pillars is also an influencing factor for the stiffness of the sensor cavity. As the bending stiffness of polyimide and SU-8 coated polyimide differ by two orders of magnitude, a larger spacing c_{dist} between the pillars decreases the stiffness of the cavity in Eq. 4.4. However, the spacing should be smaller than the diameter of the microspheres (250 μm) to avoid that the microspheres *drop* into the void space between the pillars and increase the hysteresis of the microsphere movement. Instead, the side walls of the cavity should provide an

even boundary which is the reason for pillars with a square cross section.

Experimental trials show that a spacing of 20 μm and less leads to an underdevelopment between the pillars, while a spacing of 40 μm and more ensure a good development.

Based on the above observations, the pillar edge length c_{pillar} is selected as 60 μm and the minimum spacing c_{dist} is 40 μm for all further cavity designs.

The height of the pillars was set to 150 μm in order to achieve a final cavity height of around 300 μm which allows for a unobstructed movement of the microspheres with a diameter of 250 μm within the cavity. Fig. 4.7a shows an SEM picture of a pillar cavity with a diameter of 2 mm and five rows of pillars. By using several rows of pillars instead of a single row, the stability of the pillar structure is increased. This cavity design will be used in later evaluations of the sensor for a 4-contact and 8-contact sensor.

The pillar height has been acquired with a profilometer in Fig. 4.7b, depicting the whole cavity. The imperfections on the right side of the image are measurement artefacts which are due to the measurement tool. In addition, we show the height profile along the dotted, circular line in Fig. 4.7c. The pillar height varies over the area of the cavity with a maximum deviation of ± 10 μm from the targeted height of 150 μm . This deviation is due to the fabrication process on the flexible polyimide foil where the SU-8 spin-coating does not yield a homogeneous thickness.

4.2.1.2 UV exposure

As a UV light source was used for the exposure of SU-8, the top edges of the pillars formed an overhang, leading to a continuous connection as seen in Fig. 4.8a. The undesired *T-topping* effect has already been reported in literature [94], but can also be used for new applications, e.g. a hollow microneedle array [95]. The T-topping is due to the high absorption of SU-8 at wavelengths below 350 nm. With these wavelengths, the top part of the photoresist is strongly exposed while the bottom part of the layer is not. This leads to the crosslinking and the formation of the overhang resulting in the above described effect [96].

To mitigate the T-topping, wavelengths below 350 nm need be cut out of the spectrum. We introduce an optical high-pass filter (HOYA UV-34) with a cut-off wavelength of 360 nm. As also wavelengths above

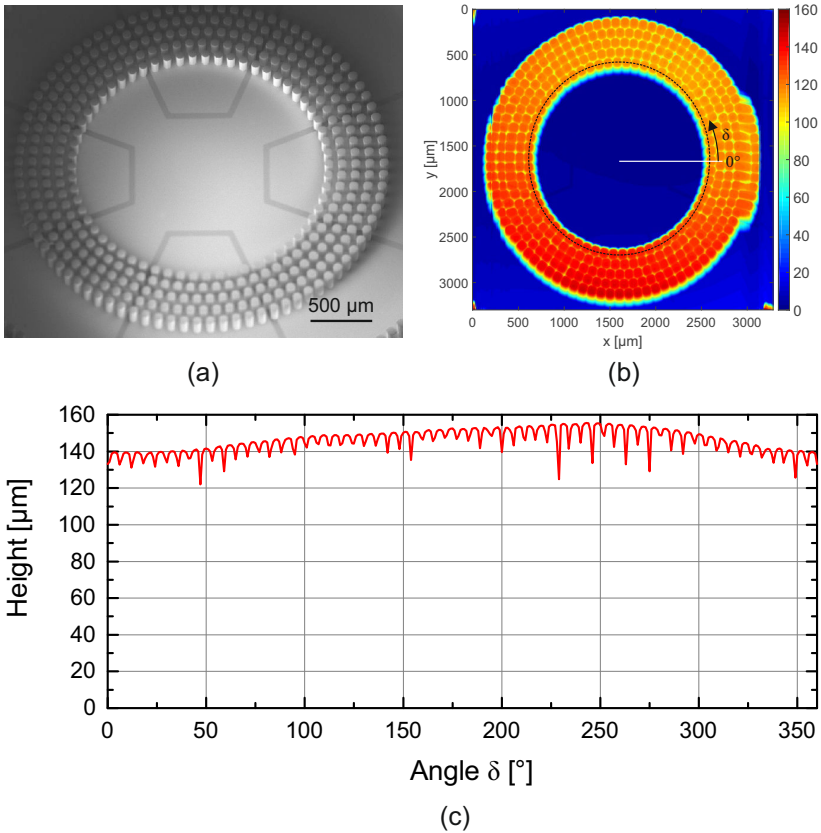


Figure 4.7: a) SEM picture of a pillar cavity with pillar edge length of 60 μm, spacing of 40 μm, cavity diameter of 2 mm and five rows of pillars. b) Height of pillar cavity acquired with profilometer; measurement artefacts on right side of picture. c) Height profile along dotted line in (b).

the cut-off wavelength have a reduced transmission of around 87%, the total exposure time needs to be increased by 40% compared to the required exposure time without a filter. This leads to an optimized result of the pillars with no T-topping and well exposed and developed pillars (see Fig. 4.8b).

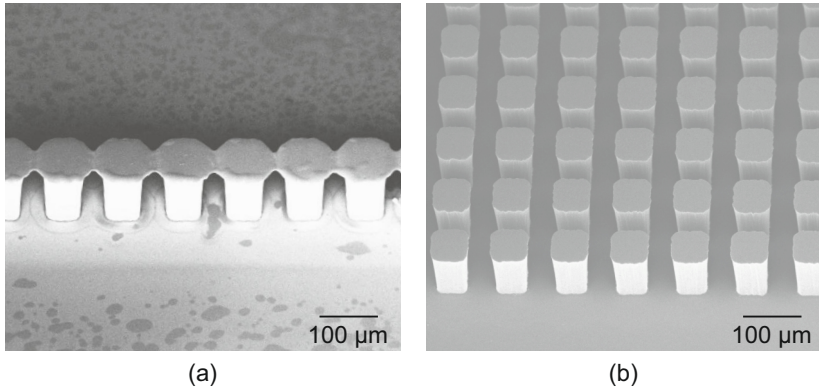


Figure 4.8: SEM picture of SU-8 pillars a) without optical filter during exposure and b) with high-pass filter (cut-off frequency $\lambda_{cutoff} = 360$ nm) during exposure.

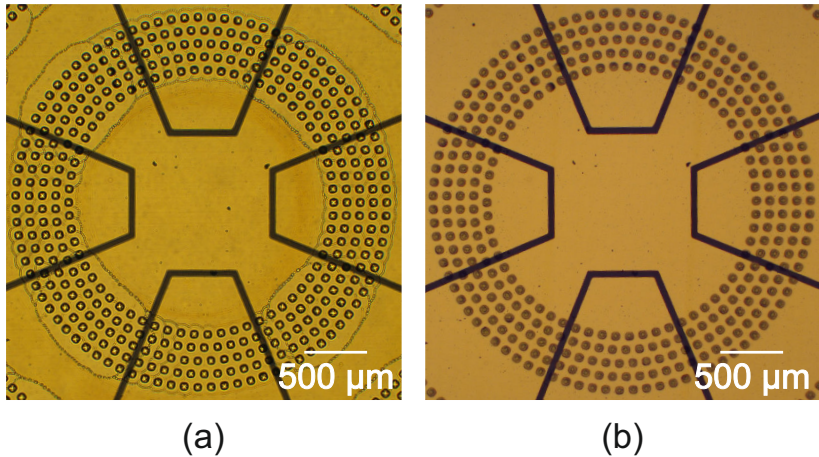


Figure 4.9: Macrograph of sensor cavity a) before reactive ion etching and b) after 4 min of reactive ion etching with O_2 plasma.

4.2.1.3 Surface cleaning

During the SU-8 pillar fabrication process, a reactive ion etching process (Fig. 4.5e) is performed. Despite agitation during the develop-

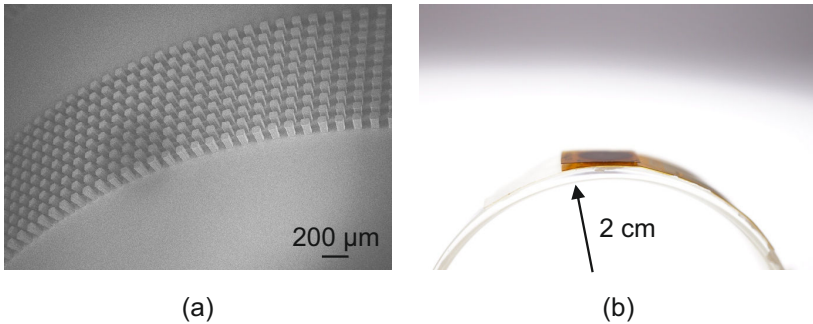


Figure 4.10: Photograph of cavity fabricated with SU-8 pillars, bent to a radius of 4 mm (a) and 2 cm (b).

ment process of SU-8 with mr-Dev 600 and extended development time, SU-8 residue remains on the substrate surface. Fig. 4.9a shows a micrograph of the substrate surface after the drying following the SU-8 development. Especially close to the pillar structures, the surface is covered with residue from the development. This residue would prohibit a reliable electrical contact between the pendulum of the tilt sensor and the contact pads and thus needs to be removed before further processing.

RIE allows to clean the substrate surface. The sensor is placed in an O_2 plasma at 150 W, 130 μ bar, and 100 sccm flow for 4 min. After the RIE treatment, the surface is free of remaining residue (see Fig. 4.9b). No change of the dimensions of the SU-8 pillars due the dry etching can be observed.

4.2.2 Bendability

The bendability of the cavity fabricated with SU-8 pillars is examined. The pillar structure increases the bendability compared to the layer cavity (Fig. 4.4).

The substrate with the cavity is attached to double-sided adhesive tape and subsequently attached to objects with different radii.

First, we examine the cavity without closing and sealing it with a second polyimide layer on top. A bending radius of down to 4 mm is possible, at lower bending radii the pillars delaminate from the substrate. Fig. 4.10a shows that the pillars fan out during the bending

which increases the pillar spacing by 2.5% at the top edge, avoiding the strain that would build up in a continuous layer.

Fig. 4.10b depicts the closed and sealed cavity which is bent down to a radius of 2 cm, corresponding to a maximum strain of 1% (Eq. A.6). A further decrease of the bending radius leads to a delamination of the SU-8 pillars from the bottom substrate.

The strain of 1% is absorbed both by a bending of the pillars as well as an elongation of the polyimide layer. Due to the high second moment of area of the SU-8 pillar structure, the polyimide elongation absorbs the majority of the strain (around 97%) while the rest is absorbed through a bending of the pillars. Based on Hooke's law, the resulting force F on the glued areas of the cavity, normalized to the width of the substrate w , is

$$\frac{F}{w} = h_{PI} \cdot E_{PI} \cdot \epsilon \cdot 97\% = 2.67 \times 10^3 \text{ N m}^{-1}. \quad (4.5)$$

The elongation of the polyimide foil in the area of the cavity with an outer diameter of 5 mm is around 48.5 μm while the pillars are bent by around 1.5 μm at their end. Compared to a flat surface, the pillar structure increases the contact area with the glue by a factor of four. This enables increased delamination forces which allows a higher bendability of the device.

4.3 Conclusion

Two different cavity fabrication processes have been presented with respect to their complexity and their bendability. The stacking of polyimide layers has been found to be a simple approach to fabricate a sensor prototype, but is less precise due to the required alignment of the layer stack. The approach with SU-8 pillars requires more processing steps, but is more suitable for mass fabrication due to the reduced number of alignments. The bendability of both approaches has been examined with a clear advantage for the pillar structure as it allows lower bending radii (down to 2 cm).

5

Contact mechanics

We discuss the interaction of the microsphere with the substrate surface and SU-8 cavity wall. The theory of the electrical contact between microsphere and substrate surface is presented and the resulting contact resistance is evaluated. The contact mechanics of the contact of microsphere and substrate surface and cavity wall are introduced and assessed with atomic force microscopy. Finally, lateral force microscopy determines the friction coefficient of the microsphere upon interaction with the different cavity materials.

5.1 Electrical contact resistance

The electrical connection created by the microspheres with the substrate surface is a key factor for the successful operation of the tilt sensor. In the following, we focus on this topic in more detail to determine the parameters for creation of a reliable electrical contact with the microspheres.

As described in chapter 3, the microspheres are solder spheres with a diameter of 250 μm . In the following, the electrical contact resistance of the microsphere with the substrate surface will be investigated. Therefore, we attach two gold coated substrates perpendicular to each other, forming a V-shaped trench (see Fig. 5.2). The two gold layers do not have an electrical connection. We place a single microsphere inside this trench and measure the electrical resistance between the two substrates.

With an uncoated microsphere, no electrical connection can be established at any tilt angle. Only once the load on the microsphere is increased by additional weight, the oxide on the microsphere surface cracks open and an electrical connection through the microsphere is made. However, the required load is around 1 mN for tin-oxide [97] which exceeds the weight of a single microsphere ($F_G = 0.6 \mu\text{N}$) by several orders of magnitude. Therefore, a coating of the microsphere with gold (see chapter 3) is required for the formation of a reliable electrical contact.

The electrical resistance of the setup is composed of several serial components according to Fig. 5.1a: each contact point of the microsphere with the substrate exhibits the constriction resistance R_C and the Sharvin resistance R_S [98]. In addition, the coating of the microsphere exhibits a resistance R_{sp} . All values are dependent on the radius a of the a -spots which are the electrical contact areas. Solid surfaces are rough on a micro scale, thus the electrical contact is not formed on the whole area of mechanical contact, but only on the contact of the a -spots.

- **Constriction resistance R_C**

The constriction resistance is the classical ohmic resistance where the electrical flow in the contact is assumed continuous and can be calculated according to [98]:

$$R_C = \frac{\rho}{2a}. \quad (5.1)$$

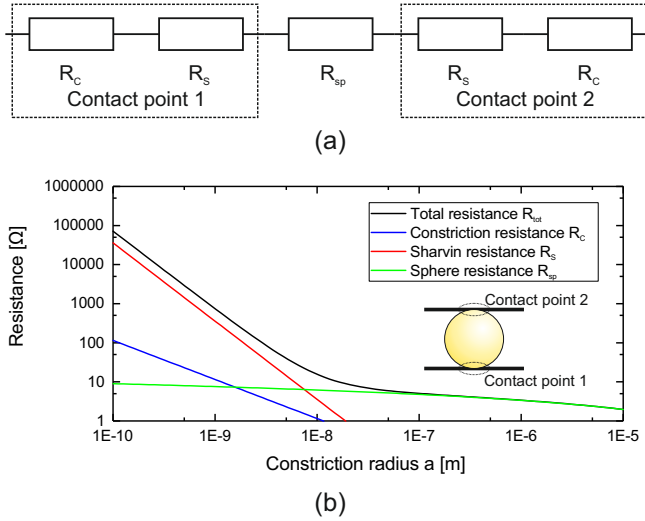


Figure 5.1: (a) Identification of electrical resistance components of a single microsphere in a V-shaped trench; (b) Total contact resistance R_{tot} and resistance components for a gold-coated (thickness: 12 nm) microsphere contacted at opposite sides with respect to the constriction radius a .

- **Sharvin resistance R_S**

When the scale of the contacting solids is sufficiently small, i.e. when the radius a approaches the free mean path of the electrons l_{fp} , the current flow cannot be assumed as continuous. Instead, the electrons have an irregular motion as they collide with lattice imperfections and other defects and thus create the electrical current. This Knudsen effect arises for $a < l_{fp}$ with $l_{fp,Au} = 38.3 \text{ nm}$ [98]. In addition to the above constriction resistance, the Sharvin resistance arises which can be calculated according to

$$R_S = \frac{C}{a^2} \quad (5.2)$$

where C is a constant dependent on the electronic properties of the conductor and is $C_{Au} = 3.58 \times 10^{-16} \Omega \text{ m}^2$ [99].

- **Sphere resistance** R_{sp}

The gold coating on the surface of the microsphere exhibits its own resistance. Assuming that the current only flows through the gold coating and not through the sphere itself, the resistance between two points opposite to each other on the microsphere can be calculated by the following formula (see appendix, Eq. A.12):

$$R_{sp} = \frac{\rho}{2\pi h_{Au} R} \int_a^{\pi R - a} \frac{1}{\sin\left(\frac{x}{R}\right)} dx \quad (5.3)$$

$$= \frac{\rho}{2\pi h_{Au}} \left[\ln\left(\tan\left(\frac{\pi R - a}{2R}\right)\right) - \ln\left(\tan\left(\frac{a}{2R}\right)\right) \right].$$

Here, R is the radius of the microsphere and $h_{Au} = 12$ nm the thickness of the gold coating on the microsphere.

The total resistance R_{tot} can therefore be calculated as

$$R_{tot} = 2R_C + 2R_S + R_{sp} \quad (5.4)$$

which is only dependent on the constriction radius a . In Fig. 5.1b, R_{tot} is depicted as a function of a with $\rho_{Au} = 2.3 \times 10^{-8} \Omega \text{ m}$. For a constriction radius above $0.01 \mu\text{m}$, the total resistance is below 10Ω . However, for $a < 0.01 \mu\text{m}$ the resistance increases and reaches a value of 750Ω for $a = 1$ nm. This increase is due to the Sharvin resistance which becomes dominant for values of the constriction radius which are significantly smaller than the free mean path of the electrons l_{fp} .

We repeatedly measure the resistance between the two gold substrates with three different microspheres at different tilt angles. The gold coated substrates have received a treatment by RIE following chapter 4.2.1 to achieve results which are comparable to a fully fabricated tilt sensor. Fig. 5.2 shows that for angles $\lambda < 25^\circ$ and $\lambda > 65^\circ$, no conduction between the two gold plates can be measured. For angles $25^\circ \leq \lambda \leq 65^\circ$, the average resistance is around 400Ω . No significant dependence of the resistance on the tilt angle in this range can be observed.

The force of the microsphere on the contact plates can be determined which is required to create an electrical contact between the microsphere and the substrate surface. With a mass of $m = 60 \mu\text{g}$ and a weight of $F_G = 0.6 \mu\text{N}$, the resulting minimal force F_N can be calculated as

$$F_N = F_G \cdot \sin(\lambda) = 0.6 \mu\text{N} \cdot \sin(25^\circ) = 0.25 \mu\text{N}. \quad (5.5)$$

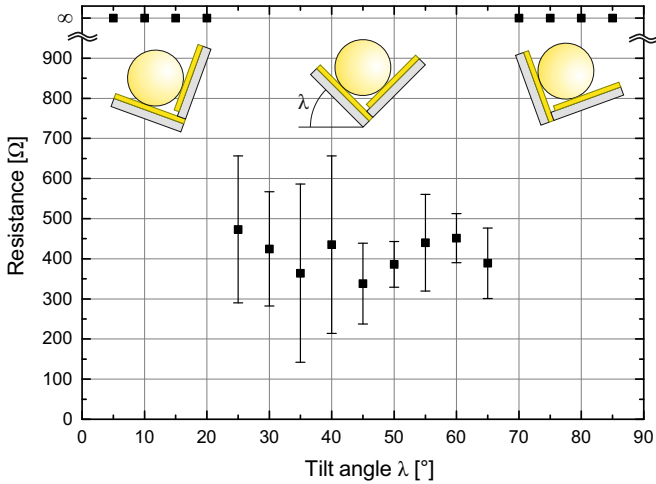


Figure 5.2: Contact resistance of a single microsphere in a V-shaped trench with respect to the tilt angle of the trench ($>$ five measurements, each for three different microspheres).

The non-contact at low ($< 25^\circ$) and high ($> 65^\circ$) contact angles can be attributed to a wetting of the microsphere and substrate surface. As we perform the above experiments and the fabrication and assembly of the tilt sensor in ambient air, the metal surface is likely to attract humidity and form a thin water film [100, 101]. This water film is insulating the electrical contact. However, once a threshold force of $0.25 \mu\text{N}$ between the two contacts is exceeded, the water film is pushed aside and an electrical connection is made [98]. This required threshold force could be reduced by performing the fabrication and assembly of the sensor in an inert, e.g. N_2 , atmosphere to avoid the wetting.

From the resulting average resistance of 400Ω , it can be concluded that the constriction radius of the gold coated microsphere with the gold coated substrate is around 1.3 nm which is more than a magnitude smaller than $l_{fp,Au} = 38.3 \text{ nm}$. Due to the low normal force of $0.25 \mu\text{N}$ of the microsphere onto the substrate surface, the value for the constriction radius is comprehensible.

5.2 Surface properties

We investigate the contact mechanics of the microsphere with the different surfaces of the tilt sensor and relate the surface roughness to the expected influence of adhesion forces and on the friction.

5.2.1 Surface roughness

In the following, the surface roughness of the different surfaces involved in the tilt sensor is measured by atomic force microscopy (AFM) which will be used to determine the influence of the roughness on the adhesion forces.

As the Young's Modulus E of the polyimide $E_{PI} = 5.5 \text{ GPa}$ is a magnitude smaller than the Young's Modulus of the solder alloy with $E_{sphere} = 51 \text{ GPa}$, we can apply a theoretical model of a rigid sphere indenting an elastic surface. The theory of this model has been developed by Heinrich Hertz (Hertzian Contact Theory) in 1881 [102] and allows to calculate the mechanical contact area of the microsphere with the substrate surface. The force F_{ind} required to create an indentation of d_{ind} into the elastic surface can be calculated according to [103]

$$F_{ind} = \frac{4}{3} E^* R^{1/2} d^{3/2} \quad (5.6)$$

where R is the radius of the sphere and E^* is the Young's modulus incorporating the poisson ratio ν for polyimide $\nu_{PI} = 0.32$:

$$E^* = \frac{E_{PI}}{(1 - \nu_{PI}^2)} = 6.13 \text{ GPa}. \quad (5.7)$$

From Eq. 5.5, the maximum normal force that one microsphere creates, when an electrical connection is established, is $F_{N,max} = F_{ind,max} = 0.54 \mu\text{N}$ at $\lambda = 65^\circ$. The maximum indentation d_{ind} thus is calculated with Eq. 5.6 according to

$$d_{ind,max} = \left(\frac{3}{4} \cdot \frac{1}{E^*} \cdot \frac{1}{R^{1/2}} \cdot F_{ind,max} \right)^{2/3} = 3.27 \times 10^{-10} \text{ m}. \quad (5.8)$$

The mechanical contact radius a_{mech} is determined to [103]

$$a_{mech} = \sqrt{R \cdot d_{ind}} = 0.2 \mu\text{m}. \quad (5.9)$$

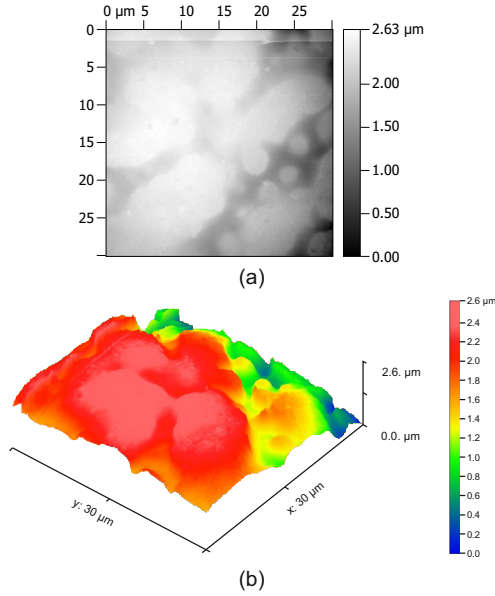


Figure 5.3: Two-dimensional (a) and three-dimensional (b) AFM representation of the surface of a microsphere in an area of $30\ \mu\text{m} \times 30\ \mu\text{m}$.

a_{mech} is larger than the constriction radius a , as the former is the macroscopic contact radius, while the latter describes the microscopic contact radius.

In Fig. 5.3, we show an atomic force microscopy (AFM) picture in an area of $30\ \mu\text{m} \times 30\ \mu\text{m}$. The curvature of the microsphere with regard to the center point of the measurement is around $0.9\ \mu\text{m}$ and is confirmed by the measurement. The difference between the elevated areas and valleys on the surface is up to $1\ \mu\text{m}$ which is several magnitudes larger than the indentation depth of $3.27 \times 10^{-10}\ \text{m}$. Therefore the contact of the microsphere with the underlying surface solely takes places on the elevated areas of the microsphere surface. The diameter of the elevated area on the microsphere surface is around $10\ \mu\text{m}$ which is also larger than the contact radius of $0.2\ \mu\text{m}$ according to Eq. 5.9. Thus, the contact of the microsphere with the substrate will only occur on a single elevated area. The surface roughness, defined by the RMS (root mean square) value, of such an elevated area is determined to

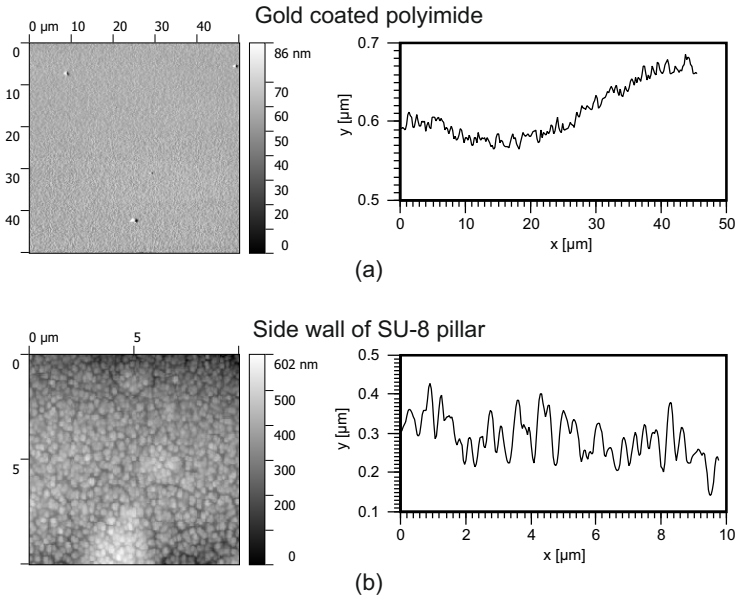


Figure 5.4: (a) Two-dimensional (left) and one-dimensional (right) AFM representation of gold coated polyimide in an area of $10\ \mu\text{m} \times 10\ \mu\text{m}$; (a) Two-dimensional (left) and one-dimensional (right) AFM representation of SU-8 in an area of $10\ \mu\text{m} \times 10\ \mu\text{m}$.

$$RMS_{\text{sphere}} = 64\ \text{nm}.$$

As the surface roughness of the involved surfaces can mitigate adhesion forces, such as van der Waals forces, we determine their influence. These adhesion forces are - usually attractive - forces between molecules or atomic groups, but are not based on covalent or ionic bonds. The force is proportional to r_{dist}^6 where r_{dist} is the distance of the two bodies of interest. Therefore an increased surface roughness (RMS value) is beneficial to mitigate the adhesion forces, as with rough surfaces only a small number of microscopic points are in contact with each other.

The surface roughness reduces the influence of adhesion forces when the following relationship of the critical penetration depth d_{crit} is met [103]:

$$RMS \gg \left(\frac{3\pi^2 \gamma^2 R}{16E^*2} \right)^{1/3} = d_{\text{crit}} \quad (5.10)$$

where $\gamma_{Au} = 1.04 \text{ J m}^{-2}$ is the surface energy of gold [104]. The right side of Eq. 5.10 is computed to a value of $d_{crit} = 18.8 \text{ nm}$.

The AFM scans on a gold coated polyimide surface as well as on the side of a SU-8 pillar are shown in Fig. 5.4a and b, respectively. The left graph shows a representation of the surface over an area while the right graph shows the height characteristics for a single scan line. The gold surface shows a roughness with a value of $RMS_{Au} = 18.9 \text{ nm}$. On the contrary, the SU-8 shows a structure with grains of the size of around 200 nm which contribute to a roughness of $RMS_{SU-8} = 82.9 \text{ nm}$. The values are summarized in Tab. 5.1.

Table 5.1: Root mean square (RMS) values for the surface roughness of different surfaces.

Surface	RMS value [nm]
Microsphere	64.0
Gold coated polyimide	18.9
SU-8 pillar side wall	82.9

The relation between the value of RMS_{sphere} compared to RMS_{Au} is in line with the observation on the contact resistance in chapter 5.1. A small constriction radius a is observed which is due to the high surface roughness of the microsphere.

Both the values of RMS_{sphere} and RMS_{SU-8} are larger than the critical penetration depth $d_{crit} = 18.8 \text{ nm}$. Therefore, in the case of a contact of the microsphere with the SU-8 pillars, the adhesion forces are mitigated by the surface roughness of both materials and do not influence the free movement of the microspheres inside the cavity.

The values of RMS_{Au} and d_{crit} are in a similar range, the roughness of the gold is not high enough to mitigate the adhesion forces. The adhesion forces of the gold coated polyimide will thus have an influence on the movement of the microspheres. However, with the knowledge from chapter 5.1, it is not advisable to increase the surface roughness by corresponding processing, as an increased roughness further decreases the constriction radius a which in return increases the contact resistance further.

5.2.2 Friction

Here, a friction measurement is performed to gain insight into the kinematic friction coefficient μ_k [105] which is an important parameter for the sliding of the bulk of the microspheres inside the cavity. The measurement is conducted by lateral force microscopy (LFM), an experimental technique for nanotribology. In contrast to a regular AFM measurement, where the deflection of the cantilever is detected while the tip of the cantilever is brought into contact with the substrate surface, the substrate is moved sideways in LFM. This happens while cantilever and substrate are in contact and the torsion of the cantilever is measured, as shown in Fig. 5.5a.

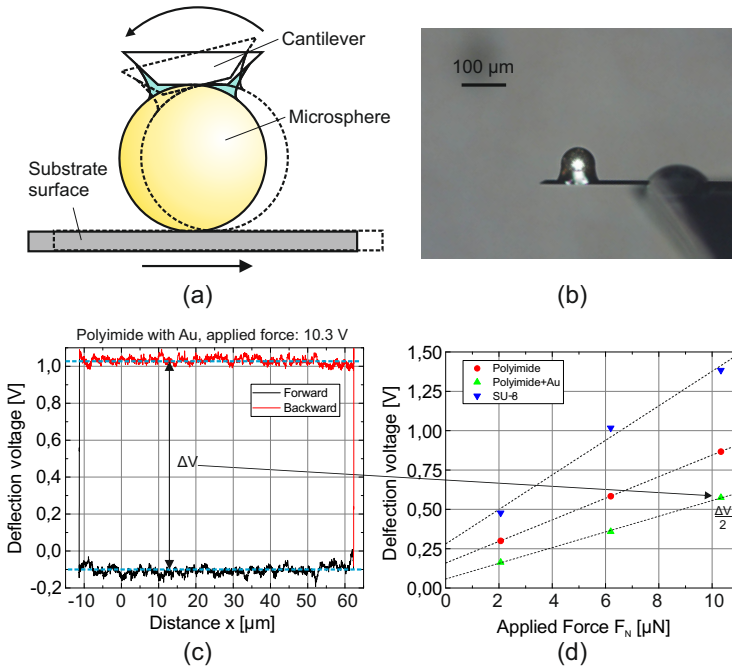


Figure 5.5: (a) Schematic illustrating principle of lateral force microscopy (LFM); (b) Micrograph of microsphere with diameter of 75 μm glued to cantilever; (c) Single measurement run obtained for an applied voltage of 5 V on a gold coated polyimide surface; (d) Averaged voltage differences obtained for varied applied forces F_N and on different materials.

Table 5.2: Slope and intercept of linear fit through friction measurement values on different surfaces.

Substrate surface	Slope [$V \mu\text{N}^{-1}$]	Intercept [V]
Polyimide	0.069	0.16
Polyimide with Au	0.050	0.057
SU-8	0.11	0.28
Si wafer	0.049	0.075

Instead of using a cantilever with a tip, a tipless cantilever is used and the microsphere is glued to the cantilever which acts as the tip (see Fig. 5.5b). The microsphere is brought into contact with the substrate and oscillated sideways to create a sliding of the sphere over the surface. The deflection is measured and allows to infer a friction curve. We use a cantilever with a length of $225 \mu\text{m}$, a thickness of $7 \mu\text{m}$ and a width from $14 \mu\text{m}$ at the bottom side up to $41 \mu\text{m}$ at the top side. As the friction coefficient does not depend on the size of the microsphere, we use a gold coated microsphere with a diameter of $75 \mu\text{m}$ to adapt the microsphere size to the cantilever size.

The sphere is brought into contact with the surface and a voltage is applied to create a normal force F_N of the microsphere onto the surface. The surface is then oscillated left and right, resulting in a torsion of the cantilever. This torsion results in a voltage output on the photodetector of the AFM and is different for the forward and backward movement. Fig. 5.5c shows such a single acquisition for a gold coated polyimide surface with a normal force of $F_N = 10.3 \mu\text{N}$. The voltage difference between both movement directions is a measure for the friction force between microsphere and surface.

These measurements are repeated several times at three different areas of the substrate and are averaged. For different applied forces F_N and substrate surfaces of pure polyimide, polyimide coated with Au and SU-8, we obtain the values as shown in Fig. 5.5d. A linear fit through the data yields the slope and intercept according to Tab. 5.2 which has been amended with values obtained on a pure Si wafer.

The slope of the fit is a measure of the kinematic friction between the microsphere and the substrate surface while the intercept of the fit is a measure for the interaction forces such as adhesion and electrostatic

forces. The friction of the microsphere with a polyimide surface is reduced by around 30% when the surface is coated with gold. The slope is then identical to the friction on a Si wafer which shows that the gold coating reduces the friction to a minimum. From the previous section, we know that the adhesion forces are not completely mitigated by the roughness of the gold surface. However, as the gold surface is conductive, electrostatic forces can be ruled out as a source for the interaction forces.

The interaction with a SU-8 surface shows a two-fold higher friction than with the gold surface. This is in line with the observations from the surface roughness in chapter 5.2.1 as the SU-8 surface has a higher roughness than the gold coated polyimide. The intercept is increased by a factor of 5, indicating that the interaction forces are increased. Due to the surface roughness of SU-8, adhesion forces are negligible. However, electrostatic charges that build up in the SU-8, e.g. during the fabrication process, are not mitigated by the roughness and therefore lead to the observed high value for the interaction forces.

We conclude that the SU-8 surface exhibits a high friction coefficient which inhibits a sliding movement of the microspheres in the cavity while the gold coated polyimide surface has a friction which is significantly lower than the friction on SU-8 and similar to a smooth silicon wafer surface.

5.3 Conclusion

We showed that a threshold pressure of the microspheres is required to penetrate the humidity film and create an electrical contact. The resistance of the electrical contact is around $400\ \Omega$ which is due to microscale effects of the electron movement in the contact area. The roughness of the interacting surfaces was measured and examined which showed that the adhesion forces between SU-8 and the microsphere can be neglected while the adhesion forces of the gold coated polyimide will have an influence on the microsphere. The examination of the kinematic friction of the microsphere on surfaces of gold coated polyimide and pure SU-8 confirms the conclusions that due to the increased surface roughness the friction on SU-8 is dominant compared to a gold surface.

6

Sensor modeling

The tilt sensor principle entails several geometrical design parameters that have an influence on the sensor characteristics. We introduce the different design parameters and define the evaluation criteria. A comprehensive model is introduced to quantify the leverage of the design parameters on the characteristics of the tilt sensor.

6.1 Definition of parameters

In the following, we introduce and define the design parameters of the tilt sensor and present the evaluation parameters which are used to determine the influence of the design parameters.

6.1.1 Design parameters

The sensor design in Fig. 2.3 entails several geometrical design parameters that can have an influence on the sensor characteristics. We investigate parameters that describe the design and layout of the contact pads on the sensor substrate (Fig. 6.1) as well as specifications concerning the cavity and pendulum (Fig. 6.2):

- *Number of contact pads N* : The number of contact pads inside the cavity (Fig. 6.1a).
- *Sensor pad design*: Different designs are possible for the design of the sensor contact pads inside the cavity. Here, we evaluate three different arrangements (Fig. 6.1b):
 - *Trapezoidal*: Trapezoidal contact pads alternating with a ground plane.
 - *No ground*: Trapezoidal contact pads with no ground plane between the pads.
 - *Rectangular*: Rectangular contact pads alternating with a ground plane.
- *Inner contact radius r_{contact}* : The inner radius of the contact pads, i.e. the distance of the contact pads from the sensor center (Fig. 6.1c).
- *Ratio of ground to contact pad η_{pad}* : The ratio of the angle of the contact pad α_{pad} in relation to the angular resolution α_{res} as will be defined in Eq. 6.2 (Fig. 6.1d), applicable for pad styles *Trapezoidal* and *Rectangular* where $0 \leq \eta_{\text{pad}} = \frac{\alpha_{\text{pad}}}{\alpha_{\text{res}}} \leq 2$.
- *Radius of sensor cavity r_{cavity}* : The inner radius of the sensor cavity defining the movement area of the pendulum (Fig. 6.2a).
- *Amount of microspheres N_{spheres}* : The amount of microspheres inside the cavity, determining how many contact pads are connected at a given point in time. We represent the contact area

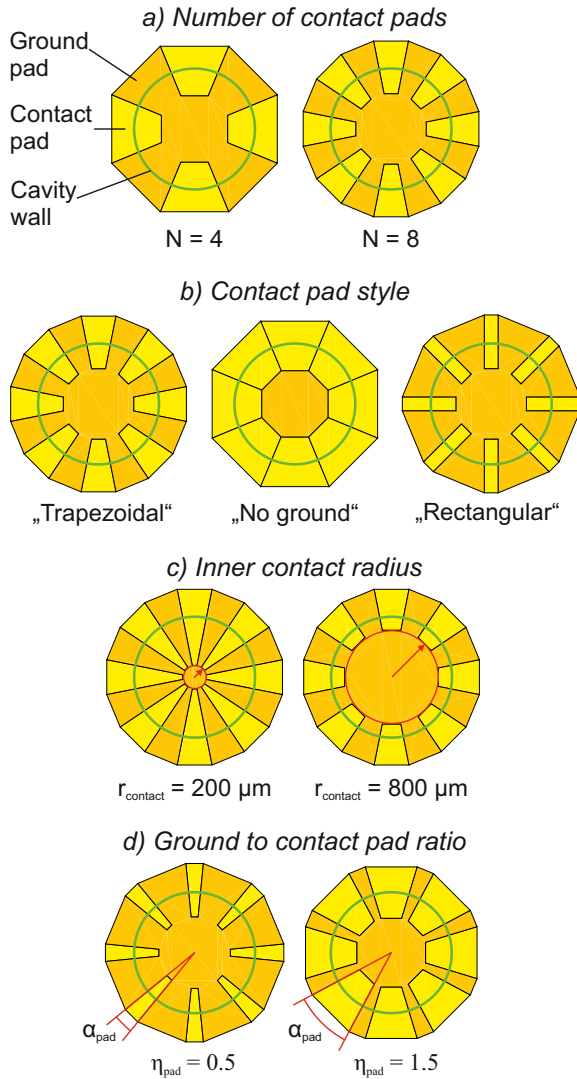


Figure 6.1: Schematic representation of the different geometrical design parameters for contact pads of the tilt sensor.

of the bulk of microspheres for the static case as a continuum, a circular segment with the height h_{disk} (Fig. 6.2b).

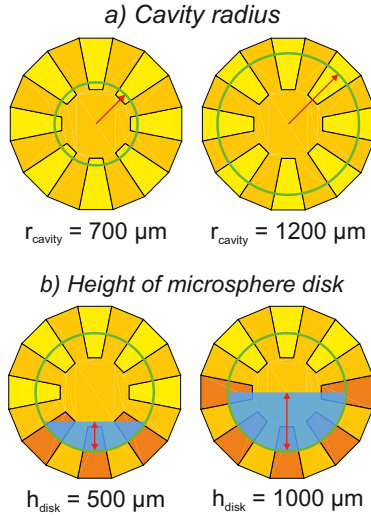


Figure 6.2: Schematic representation of the design parameters *cavity radius* and *amount of microspheres* for the tilt sensor.

6.1.2 Evaluation parameters

The sensor is an analog-to-digital converter (ADC) which converts an analog input - the applied tilt - into a digital output - the 0 and 1 of the contact pad states. The states are then converted to a corresponding tilt angle with the respective lookup table (e.g. Tab. 2.1). This leads to a graphical representation, as shown in Fig. 6.3 where the measured tilt angle is depicted over the applied tilt. We use the quantization steps as well as the non-linearity of the ADC as performance measures and apply them to the output of our tilt sensor:

The quantization steps relate to the angular resolution α_{res} of the tilt sensor and are represented by the height of the steps in the transfer function.

For the purpose of the presented tilt sensor, the non-linearity describes a difference in step length in the transfer function of the ADC and should ideally have the same length for each step. Therefore we introduce an evaluation parameter ξ_{states} which captures this behaviour. The parameter represents the ratio of the length of the shortest step and the length of the longest step. With $\alpha_{\text{states},\text{min}}$ as the smallest size of the input domain with a constant output angle value and $\alpha_{\text{states},\text{max}}$ for

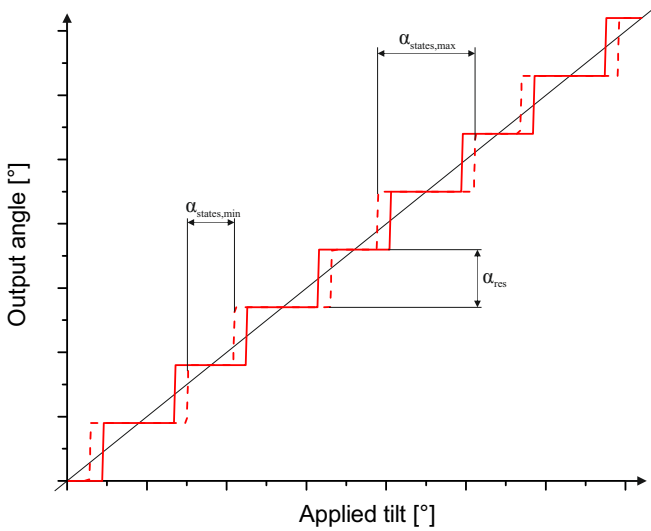


Figure 6.3: Graphical representation of transfer function of the sensor output with respect to the applied tilt angle; identification of evaluation parameter.

the largest size of the domain, ξ_{states} is defined by

$$\xi_{states} = \frac{\alpha_{states,min}}{\alpha_{states,max}}. \quad (6.1)$$

This parameter can assume values between 0 and 1 with $\xi_{states} = 1$ representing the desirable case where all step lengths are identical.

6.2 Control of design parameters

The rotational symmetry in the design of the tilt sensor allows an analytical approach to determine the influence of the design parameters on the evaluation parameters. We present the analytical solution in the following which has also been verified with respective simulations.

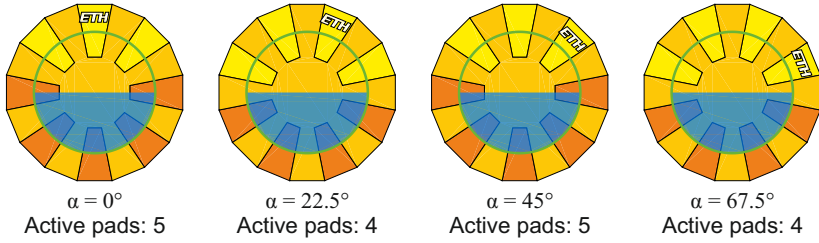


Figure 6.4: Schematic display of alternating number of *active* contact pads during changing tilt α with the pendulum microspheres represented as a continuum.

6.2.1 Resolution

The angular resolution of the tilt sensor with a number of contact pads N can be determined according to

$$\alpha_{res} = \frac{360^\circ}{2 \cdot N} \quad \forall N \geq 3. \quad (6.2)$$

Each additional contact pad in the circular arrangement adds another contact which can change its state. During the change of tilt, the number of *active* contact pads alternates between an odd and an even amount, as depicted in Fig. 6.4. Therefore, the denominator is complemented by an additional factor of 2.

The number of contact pads is the only design parameter which has an influence on the resolution of the tilt sensor. However, as will be demonstrated in the following section, the number of contact pads also influences the non-linearity, i.e. the differences in step length of the transfer function.

6.2.2 Non-linearity

Sensor pad design

As the evaluation of the non-linearity depends on the contact pad style, we first determine the best pad style in terms of non-linearity. For this, we simulate a full rotation of the tilt sensor by changing the design parameters in the following boundaries:

- $4 \leq N \leq 20$, stepsize: 1
- $100 \mu\text{m} \leq r_{contact} \leq 1000 \mu\text{m}$, stepsize: $100 \mu\text{m}$

- $0.05 \leq \eta_{pad} \leq 1.95$, stepsize: 0.05
- $r_{cavity} = 1000 \mu\text{m}$
- $250 \mu\text{m} \leq h_{disk} \leq 1750 \mu\text{m}$, stepsize: 25 μm

For each parameter combination, we determine the non-linearity ξ_{states} and subsequently calculate the average for all combinations. The resulting average value for each pad style is given in Tab. 6.1.

Table 6.1: Average value for evaluation parameter ξ_{states} for each pad style after a parameter sweep across all other design parameters.

Contact pad style	Mean of ξ_{states}
Trapezoidal	0.3818
No ground	0.3783
Rectangular	0.3673

The noted values are less than 0.4 as the values are obtained by averaging over all obtained ξ_{states} for all parameter sets. The table shows a dependency of the non-linearity on the contact pad style. We see an advantage for the pad style *Trapezoidal*, as the larger the value of ξ_{states} is, the smaller is the difference in step lengths in the transfer function. The style *No ground* with the missing ground plane between the contact pads relates to a pad style *Trapezoidal* where the contact to pad ratio is $\eta_{pad} = 2$. The style *Rectangular* is similar to the style *Trapezoidal*, but as the trapezoidal shape caters more for the circular design of the pads and due to the reduced contact area of the rectangular pads, the trapezoidal pad design shows the best performance. Therefore all further analysis will be focusing on the trapezoidal design.

Radius of sensor cavity

The cavity radius r_{cavity} has no influence on the non-linearity of the tilt sensor, it merely affects the size of the sensor. As stated in the specifications in chapter 2.3, the diameter of the sensor should be in the range of several millimeter. However, the cavity radius should also be not too small to ensure a sufficient amount of microspheres in the cavity. The microsphere disk consists of discrete particles which should be taken into account. We select $r_{cavity} = 1000 \mu\text{m}$ which corresponds to

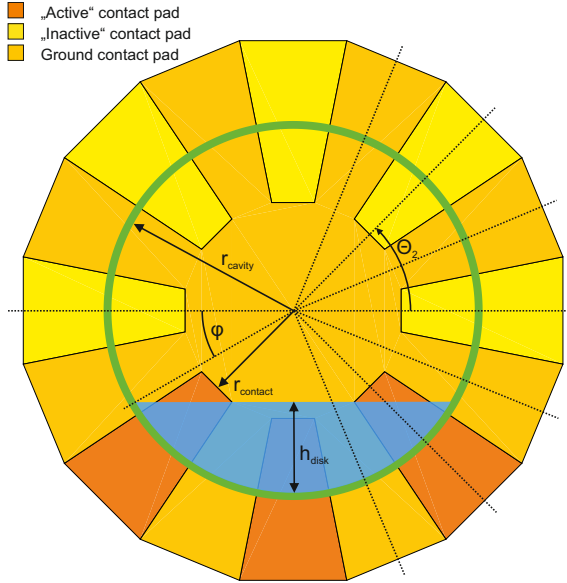


Figure 6.5: Representation of parameters for determination of the evaluation parameter ξ_{states} in a tilt sensor with $N = 8$; θ_i is exemplarily depicted for $i = 2$.

a cavity diameter that can fit 8 microspheres with a diameter of $250 \mu\text{m}$.

Inner contact radius

The evaluation parameter ξ_{states} is also not affected by the inner radius of the contacts $r_{contact}$. Nevertheless, it should be taken into consideration that the area of the contact pads inside the cavity is large enough that microspheres resting at the edge of the cavity can create an electrical contact with the contact pads below. Therefore, the relation

$$r_{contact} < r_{cavity} - \frac{d_{sphere}}{2} \quad (6.3)$$

should be kept, we select $r_{contact} = 600 \mu\text{m}$.

Number of contact pads, amount of microspheres

In order to describe the influence of the number of contact pads N , the height of the microsphere disk h_{disk} as well as the contact to ground

pad ratio η_{pad} , additional parameters are introduced for the sensor geometry and are exemplarily depicted for an 8-contact tilt sensor in Fig. 6.5:

- The angles θ_i determine the central angles of the contact pads and the ground pads with regard to the horizontal according to:

- for an even number of contact pads N :

$$\theta_i = i * \frac{360^\circ}{2N} \quad (6.4)$$

with $-\frac{N}{2} + 1 \leq i \leq \frac{N}{2} - 1, i \in \mathbb{N}$,

- for an odd number of contact pads N :

$$\theta_i = i * \frac{360^\circ}{2N} + \frac{360^\circ}{4N}. \quad (6.5)$$

with $-\frac{N-1}{2} \leq i \leq \frac{N-1}{2} - 1, i \in \mathbb{N}$.

- The ratio between the height of the microsphere disk h_{disk} and the radius of the cavity r_{cavity} is labeled with η_{disk} :

$$\eta_{disk} = \frac{h_{disk}}{r_{cavity}} \quad (6.6)$$

- The angle φ determines the angle between the horizontal and a line drawn from the cavity center to the top edge of the microsphere disk and can be calculated by:

$$\varphi = \sin^{-1} \left(\frac{|r_{cavity} - h_{disk}|}{r_{cavity}} \right) = \sin^{-1} (|1 - \eta_{disk}|) \quad (6.7)$$

Subsequently, θ_{max} is selected as the θ_i which is closest to φ .

Finally, the ratio ξ_{states} is analytically deduced as:

$$\xi_{states} = \frac{\min \left\{ \left| \varphi - \left(\theta_{max} \pm \frac{360^\circ}{4N} \right) \right| \right\}}{\max \left\{ \left| \varphi - \left(\theta_{max} \pm \frac{360^\circ}{4N} \right) \right| \right\}} * \mu_{pad}. \quad (6.8)$$

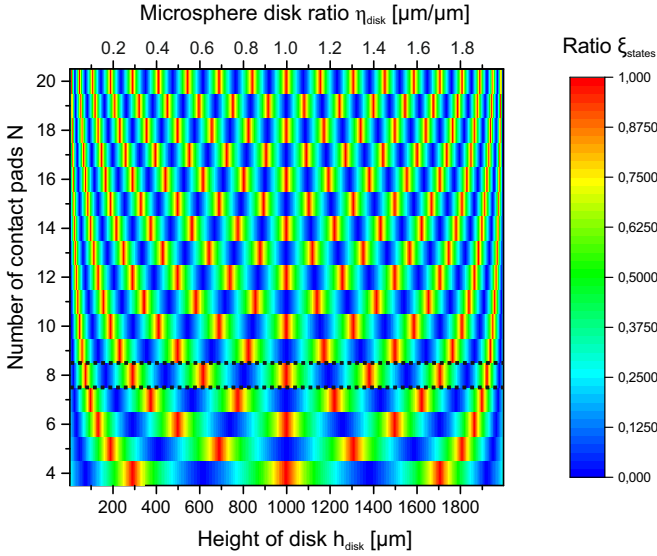


Figure 6.6: Evaluation parameter ξ_{states} dependent on the number of contact pads N and the height of the microsphere disk h_{disk} . Contact to ground pad ratio is constant at $\eta_{pad} = 1$, radius of the cavity is $r_{cavity} = 1000 \mu\text{m}$. The values for $N = 8$ (highlighted by dotted lines) are given in more detail in Fig. 6.7.

μ_{pad} is a representation of η_{pad} in the interval between 0 and 1:

$$\mu_{pad} = \frac{\min\{\eta_{pad}; 2 - \eta_{pad}\}}{\max\{\eta_{pad}; 2 - \eta_{pad}\}}. \quad (6.9)$$

The results of previously performed simulations of the sensor behaviour in this section are compared to the outcome of the above equations and confirm accurateness.

From the equations 6.7 – 6.9, it is apparent that ξ_{states} depends on N , h_{disk} as well as η_{pad} . Following the goal of finding the optimum in these three parameters with respect to the non-linearity, we first set a constant pad ratio $\eta_{pad} = 1$. We show in Fig. 6.6 the evaluation parameter ξ_{states} for varying number of contact pads N and disk heights h_{disk} . As mentioned before, we aim for a value of $\xi_{states} = 1$, i.e. the red regions are of interest. The figure shows that there is no single disk height for

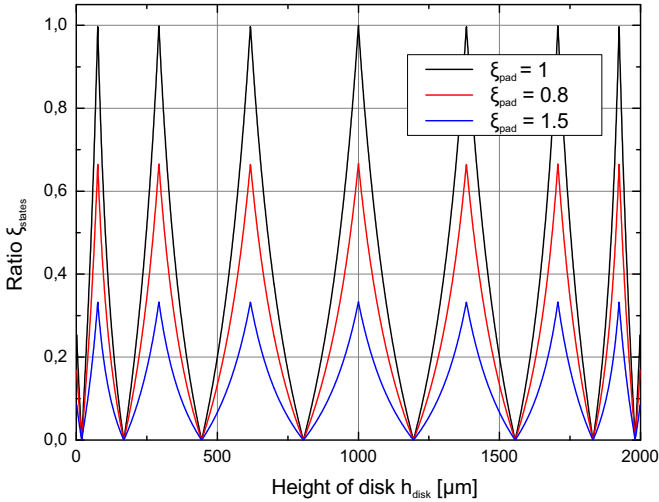


Figure 6.7: Evaluation parameter ξ_{states} dependent on the height of the microsphere disk h_{disk} and for different pad ratios η_{pad} , with $N = 8$.

all number of contacts that achieves $\xi_{states} = 1$. Instead, the disk height needs to be selected according to the number of contacts which are required to obtain the desired resolution.

Contact pad to ground pad ratio

The influence of the contact pad to ground ratio η_{pad} is evaluated in the following. Exemplarily, we choose $N = 8$ here. Fig. 6.6 shows the influence of h_{disk} as well as η_{pad} on ξ_{states} . Again, the strong dependency of ξ_{states} on the height of the microsphere disk is clearly visible, requiring to choose the amount of microspheres carefully. It is evident, also from Eq. 6.8, that a value $\eta_{pad} \neq 1$ decreases the value of ξ_{states} . The angular width of the contact pads and the ground pads should therefore have the same width, independent of the height of the microsphere disk h_{disk} or number of contact pads N .

Amount of microspheres

From Fig. 6.6 and Fig. 6.7, we observe that a disk of microspheres that covers half of the cavity, i.e. $h_{disk} = r_{cavity}$ or $\eta_{disk} = 1$ respectively, yields a ratio of $\xi_{states} = 1$ for all even N . For odd N , the disk height which achieves $\xi_{states} = 1$ is always dependent on the exact number of

N and needs to be determined individually for each N .

A greater weight of the bulk of the microspheres leads to greater pressure of the microspheres onto the contact pads. Therefore, we deduct that a ratio of $\eta_{disk} = 1$ is also beneficial for the creation of the electrical contact, as shown in chapter 5. If $\eta_{disk} > 1$, the cavity is filled more than half with the microspheres which reduces the free area for movement, therefore is also not desirable.

We have modeled the bulk of the microspheres as a solid disk with the height h_{disk} . However, this disk actually consists of discrete elements of microspheres, requiring a conversion of h_{disk} to the number of microspheres $N_{spheres}$.

With the disk being a circular segment, a disk height of h_{disk} and a cavity radius r_{cavity} corresponds to an area A_{disk} of [106]

$$A_{disk} = r_{cavity}^2 \cos^{-1} \left(\frac{r_{cavity} - h_{disk}}{r_{cavity}} \right) - (r_{cavity} - h_{disk}) \sqrt{2r_{cavity}h_{disk} - h_{disk}^2}. \quad (6.10)$$

As mentioned above, for an even number of contacts, the ideal disk height is $h_{disk} = r_{cavity}$ and Eq. 6.10 simplifies to

$$A_{disk} = \frac{\pi}{2} r_{cavity}^2. \quad (6.11)$$

We assume here that the microspheres are densely packed, therefore the packing density δ_n (fraction of area covered) results in [107]

$$\delta_n = \frac{1}{6} \pi \sqrt{3} \approx 90,7\%. \quad (6.12)$$

With A_{sphere} as the area of the cross section of the microspheres, this results in the number of spheres

$$N_{spheres} = \left\lceil \frac{\delta_n \cdot A_{disk}}{A_{sphere}} \right\rceil. \quad (6.13)$$

For a cavity with $r_{cavity} = 1000 \mu\text{m}$ and $h_{disk} = r_{cavity}$, a number of $N = 29$ microspheres are required to cover half of the cavity area. In chapter 7.2.3, high speed image recordings show that the assumption of a continuum of the microspheres is valid, as they form a bulk with the shape of a circular segment when at rest inside the cavity.

6.3 Conclusion

We have shown that the performance of the tilt sensor mainly depends on the number of contact pads N , the number of microspheres $N_{spheres}$ as well as the contact pad to ground pad ratio η_{pad} . For the following section 7 we select the parameter values as follows:

- a) *Number of contact pads:*
 - $N = 4$, achieving a resolution of $\alpha_{res} = 45^\circ$
 - $N = 8$, achieving a resolution of $\alpha_{res} = 22.5^\circ$
- b) *Sensor pad design:* Trapezoidal
- c) *Inner contact radius:* $r_{contact} = 600 \mu\text{m}$
- d) *Radius of sensor cavity:* $r_{cavity} = 1000 \mu\text{m}$
- e) *Ratio of ground to contact pad:* $\eta_{pad} = 1$
- f) *Amount of microspheres:* $h_{disk} = r_{cavity}$, resulting in $N_{spheres} = 29$.

We fabricated the corresponding tilt sensors and evaluate their characteristics in the following chapter.

7

Evaluation

We perform an evaluation of the characteristics of both the tilt switch as well as the tilt sensor. Both devices are first characterized under static conditions. We also observe the movements of the microspheres in the cavity of the tilt sensor before performing a dynamic evaluation of the tilt sensor.

7.1 Tilt switch¹

A tilt switch based on the sensing principle presented in chapter 2.2.1 is fabricated with a cavity formed by stacking layers of polyimide. The evaluated sensor has an outer dimension of 14 mm x 7 mm and an inner dimension of the cavity of 10 mm x 3 mm. The inner height of the cavity adds up to 300 μm as six layers of polyimide are stacked upon each other. The cavity is filled with 44 microspheres, a sufficient amount to cover the complete area of the contact pads ($2 \times 1.5 \text{ mm} \times 750 \mu\text{m}$) on the substrate surface.

Fig. 7.1 shows the tilt switch used for the subsequent characterization before sealing the cavity with the top layer of polyimide.

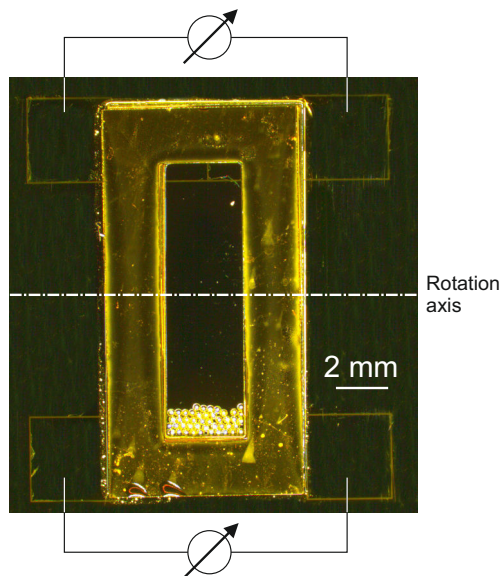


Figure 7.1: Macrograph of the fabricated tilt switch with an inner cavity size of 10 mm x 3 mm and 44 microspheres as the pendulum.

¹This section is based on "Sensoren und Messsysteme 2014, ITG-Fachbericht 250, Beiträge der 17. ITG/GMA-Fachtagung vom 3. bis 4. Juni 2014, Beitrag 36: L. Büthe u.a., A Mechanically Flexible Tilt Switch on Kapton Foil with Microspheres as a Pendulum", VDE VERLAG, Berlin, Offenbach, 2014. [88]

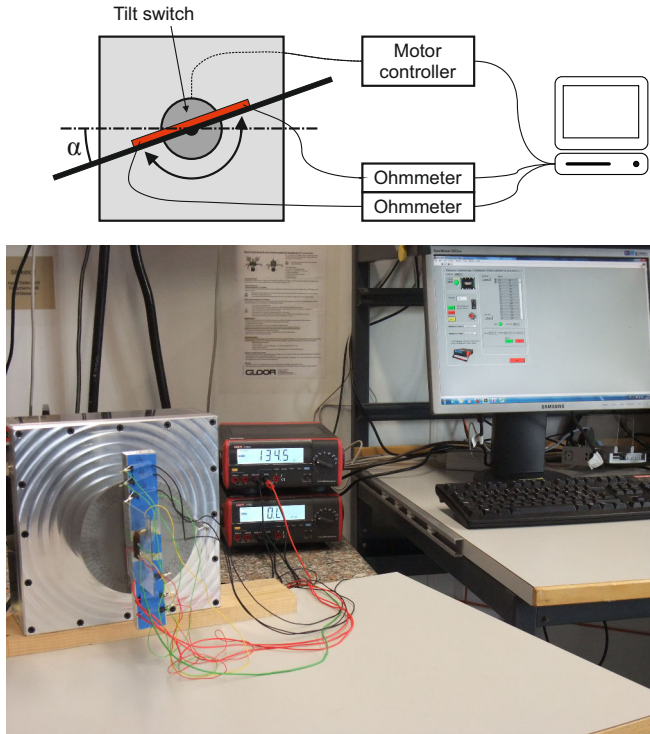


Figure 7.2: Schematic (top) and photograph (bottom) of the computer controlled measurement setup: tilt switch device on electronically actuated tilt table, connected to ohmmeters.

7.1.1 Experimental setup

We attach the sensor to an electronically actuated tilt table, controlled by a PC. Each of the two pairs of contact pads is connected to an ohmmeter which then send the data to the PC as well. A schematic and a photograph of the experimental setup is shown in Fig. 7.2.

The tilt table allows a continuous rotation. Here, we tilt the tilt switch around the axis indicated in Fig. 7.1 in the range of $-90^\circ \leq \alpha \leq 90^\circ$ in steps of 5° where α defines the angle between the sensor plane and the horizontal. After each step the resistance between two adjacent contact pads is evaluated.

Important parameters for a tilt switch are the make angle α_{make}

and the break angle α_{break} . They define the angle needed to create an electrical contact between the contact pads (α_{make}) and the angle required for breaking the electrical connection (α_{break}), respectively.

7.1.2 Static performance

In Fig. 7.3a, the measurement results for one pair of the contact pads are shown before bending the device. Once the microspheres create an electrical contact, the resistance determined with the multimeter is in the range of a few 100 Ω . For non-connected electrical contacts, an open circuit is measured.

The tilt switch shows a make angle α_{make} of 5° and a break angle α_{break} of 30° before bending. These values are the same for each pair of contacts on either side of the sensor. The make/break angle asymmetry originates from the fact that the pendulum is not a single, solid continuum, but consists of several microspheres. Not all spheres start rolling at once when the tilt of the sensor crosses the horizontal. Instead, first a few spheres start to pass over to the open contact side, closing these contacts and resulting in a low make angle α_{make} . Only when the sensor is tilted beyond the break angle α_{break} all spheres will have rolled across the cavity to the other side, leading to an open circuit of the previously connected contact pads.

In chapter 4.1.2, we already showed that the cavity allows a bending down to a bending radius of 5 cm while staying intact. After the bending, the sensor is reflattened and the characterization repeated. The results, shown in Fig. 7.3b, are in line with the state before bending: the make angle is unchanged at $\alpha_{make} = 5^\circ$, whereas the break angle has decreased to $\alpha_{break} = 25^\circ$. While bending the sensor, the glued polyimide layers already start delaminating on a microscopic level, leading to a change of the structure inside the cavity. This results in the observed change of the break angle.

Characterization of a tilt switch bent to radii smaller than 5 cm is impossible, as the sensor cavity would be destroyed (see chapter 4.1.2).

7.2 Tilt sensor²

For further investigations, tilt sensors based on the sensing principle presented in chapter 2.2.2 with a cavity formed by SU-8 are fabricated

²This section is based on [108]

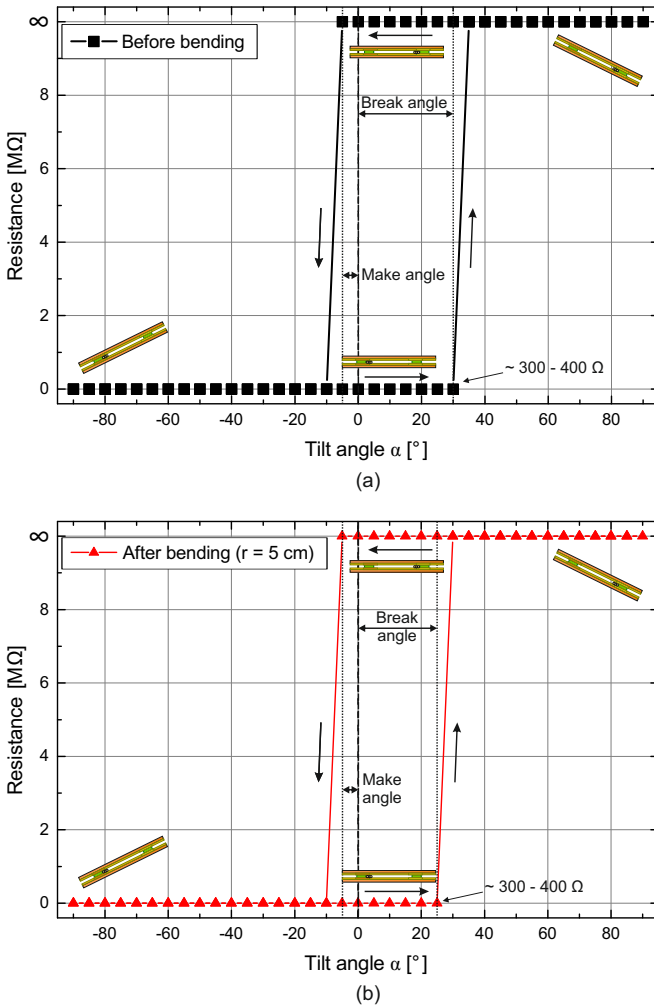


Figure 7.3: Measurement results (resistance) for tilt switch before bending (a) and after bending to a radius of 5 cm and reflattening (b).

with an outer diameter of 5.5 mm and an inner diameter of the cavity of 2 mm. The inner height of the cavity is 300 μm . The cavity is loaded with 29 microspheres, filling half of the cavity as described in chapter 6. The tilt sensors have either 4 or 8 contacts, according to Eq. 6.2 achieving a

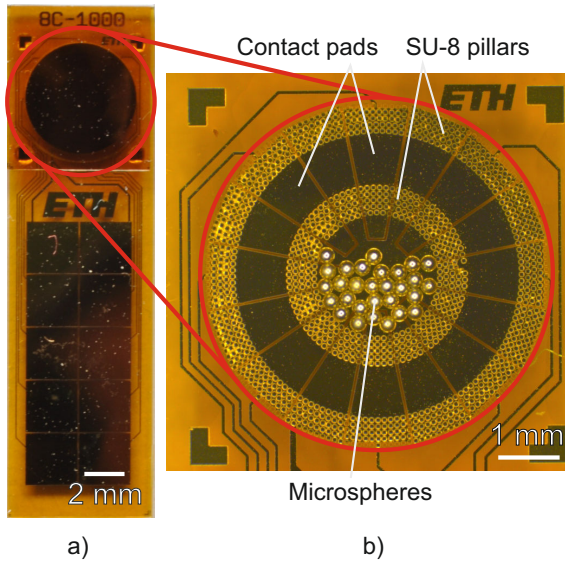


Figure 7.4: Photo- (a) and macrograph (b) of tilt sensor with 8 contacts and 29 microspheres.

resolution of 45° and 22.5° , respectively. Fig. 7.4 exemplarily shows the tilt sensor with 8 contacts used for the subsequent characterization.

7.2.1 Experimental setup

The characterization setup is a tilt table with two axes which is shown in Fig. 7.5, identifying the two axes with their respective rotation angles. γ is the rotation angle of the first (outer) axis from the horizontal. δ describes the rotation angle of the second (inner) axis with regard to the horizontal which has been previously tilted by γ . The tilt sensor is attached to the inner axis of the tilt table.

The two angles α and β which describe the orientation of the tilt sensor (see chapter 2.2.2) and the angles γ and δ are related to each other in order to calculate the orientation of the tilt sensor at a given position of the tilt table:

$$\cos \alpha = \frac{1}{\sqrt{1 + \frac{\sin^2 \delta}{\tan^2 \gamma}}} \quad (7.1)$$

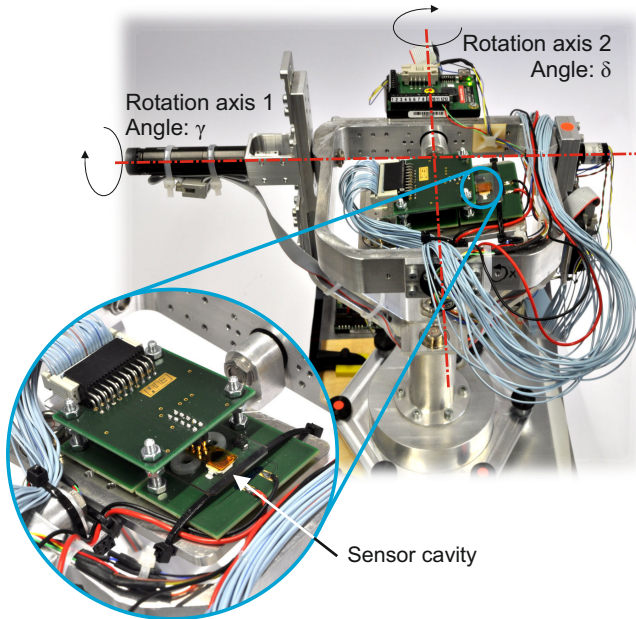


Figure 7.5: Photograph of the characterization tilt table with identification of the two rotation axes and a close-up of the tilt sensor.

$$\cos \beta = \cos \gamma \cdot \cos \delta. \quad (7.2)$$

A LED below the sensor cavity illuminates the sensor during the operation of the tilt table, allowing to observe the movement of the microspheres inside the cavity by visual inspection through the gold coated polyimide foil. Each contact pad is connected to a data logger which evaluates the contact resistance between each contact pad and the ground plane. Finally, a PC uses the respective look-up table, e.g. Tab. 2.1 for a 4-contact sensor, to determine the measured tilt by the tilt sensor. The tilt table is electronically controlled by the PC as well. It can run curves where the tilt of the sensor plane β is kept at a constant value and only the sensor tilt α is changed, which corresponds to a rotation around the normal of the sensor plane.

7.2.2 Static performance

The movement of the microspheres in the cavity has a hysteresis as not every change in the tilt angle α leads to an immediate change of the position of the microspheres. Once a threshold angle α_{hys} is reached, the microspheres start rolling towards the direction of gravity and obtain a new position at the bottom of the cavity. This angle α_{hys} is dependent on the tilt of the sensor plane β as will be shown in the following:

The tilt angle α of the tilt sensor is changed in steps of 1° from 0° to 360° with a rotational speed of 1 rpm while β is kept constant. After each step, the position of the microspheres is visually inspected. Once one or more microspheres have moved to a new position in the cavity, the angle is recorded and the difference to the previous angle at which a movement occurred is recorded. This difference is the hysteresis angle α_{hys} of the microsphere movement. As α_{hys} is smaller than the angular resolution $\alpha_{res} = 22.5^\circ$ of an 8-contact tilt sensor, α_{hys} cannot be determined by the electrical response of the tilt sensor. Therefore, the change of position of the microspheres needs to be determined by visual observation of the microspheres.

The average hysteresis angle α_{hys} along with the standard deviation of all measurements is depicted in Fig. 7.6 for different angles β . The graph shows that the tilt of the sensor plane has an influence on the hysteresis angle: both, the average as well as the standard deviation decrease with increasing tilt of the sensor plane. For $\beta \geq 50^\circ$, α_{hys} reaches a minimum of 10° with a minimal standard deviation of 2° .

The movement of the microspheres in the cavity is composed of rolling as well as sliding [105]:

- The rolling occurs when a single microsphere at the top of the bulk is lying on a downward slope. Fig. 7.7a schematically depicts the idea a rolling microsphere. During the rolling, the microsphere passes on its impulse to other microspheres which also start moving. In the end, the bulk of the microspheres has shifted towards the lower side of the cavity.
- Sliding occurs when several microspheres are in contact with each other, impeding a rolling movement. The bulk then starts sliding towards the bottom of the cavity as depicted in Fig. 7.7b.

Both mechanisms can occur simultaneously, but the rolling is the dominant effect which starts the movement of microspheres. Due to the high friction between the microspheres and SU-8 (see chapter 5.2.2) and the

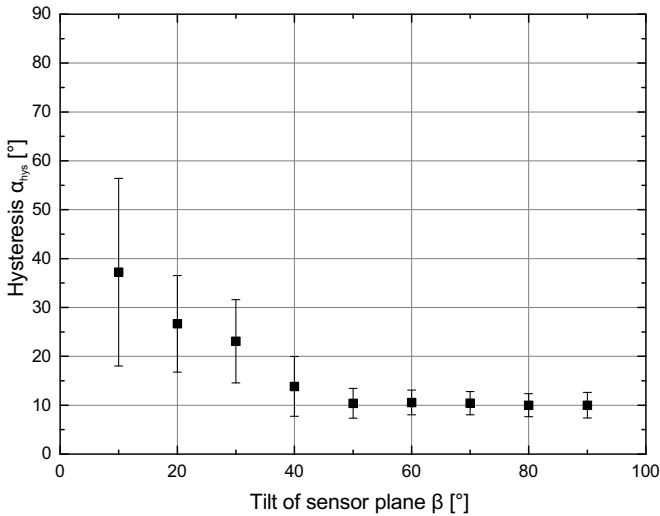


Figure 7.6: Hysteresis α_{hys} of the tilt sensor (i.e. movement of the microspheres) at different tilt angles of the sensor plane β .

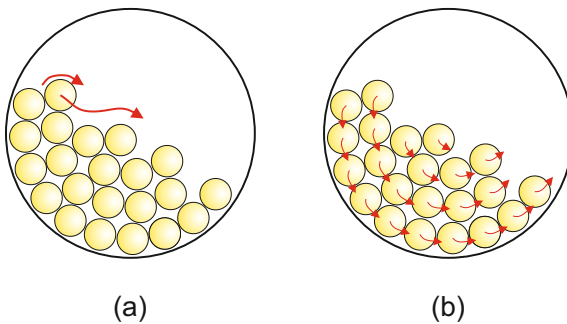


Figure 7.7: Schematic explanation of (a) rolling microsphere and (b) sliding microspheres.

lower center of gravity of the bulk of microspheres, the sliding is unlikely. In chapter 7.2.3, high speed image recordings of the microsphere movements confirm the observation.

The force that acts on the microspheres and causes the rolling is proportional to $\sin\{\beta\}$. Therefore, when the sensor plane is horizon-

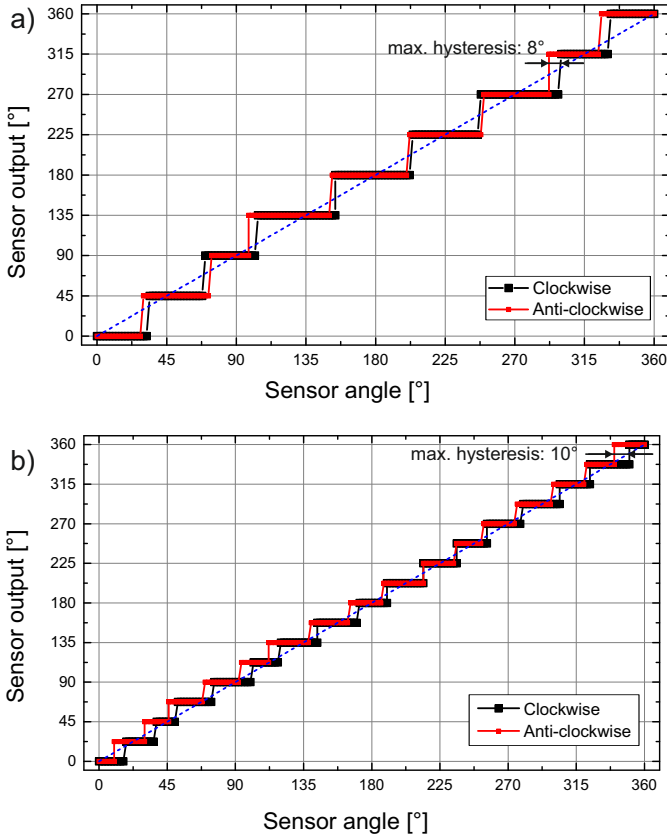


Figure 7.8: Characteristics of a 4-contact tilt sensor (a) and 8-contact tilt sensor (b) at a tilt of the sensor plane $\beta = 50^\circ$.

tal ($\beta = 0^\circ$), the static change of α does not effect the microsphere movement while the hysteresis angle α_{hys} decreases with increasing β .

The dependency of α_{hys} on the β makes it desirable to operate the tilt sensor with a low hysteresis: thus the tilt sensor should be operated when the sensor plane is tilted by 50° or more. However, as shown in chapter 5.1, the electrical contact is only reliable for tilt angles up to 65° . Therefore, the tilt sensor will only be characterized at $\beta = 50^\circ$ in the following parts of the evaluation.

After determining the hysteresis of the microsphere movement, we

measure the electrical output of the tilt sensor in the static case. The sensor is evaluated by a full clockwise and anti-clockwise rotation of α at $\beta = 50^\circ$. α is changed in steps of 1° with a speed of 1 rpm, and the states of the contact pads are recorded 1 s after the movement has stopped to ensure that the microspheres are not moving. Via look-up table (analog to table 2.1) the states are converted to the output angle. An exemplary curve for a 4-contact and an 8-contact tilt sensor each is depicted in Fig. 7.8.

The quantization steps of the transfer function are visible with eight steps for the 4-contact sensor and 16 steps for the 8-contact tilt-sensor, respectively. The characteristic curve follows the linear bisecting line in both graphs. However, deviations in the step lengths are visible which are different for each obtained curve. The deviations can be attributed to

- the random arrangement of the microspheres in the bulk which makes a prediction of the exact movement impossible,
- the hysteresis of the microsphere movement in the cavity.

The maximum value of the hysteresis between a clockwise and anti-clockwise rotation does not exceed an average of 10° which is in line with the conclusions from Fig. 7.6.

The measurement is repeated after bending the tilt sensor to a bending radius of 2 cm and reflattening (see chapter 4.2.2). The subsequently obtained characterization curve shows no deviation from the measurement in Fig. 7.8, therefore allowing the conclusion that bending and reflattening does not lead to a measurable change of the inside structure of the cavity.

7.2.3 Response time

An important parameter to characterize the performance of tilt sensors is the response time which is evaluated in this section. The response time of the tilt sensor indicates the time needed from a tilt change until this change is reflected on the sensor output.

We determine the response time visually by performing a recording of the microsphere movement with a high-speed camera (*Phantom v1610*) at a frame rate of 1000 fps. The camera films vertically from the top while the sensor plane is tilted by 50° . Several recordings are established at a rotation speed of 10 rpm, a typical recording of a microsphere movement is shown in Fig. 7.9 in intervals of 4 ms.

Instead of sealing the sensor cavity with a gold-coated polyimide layer on top, the cavity is closed with a glass slide. If sealed with the polyimide layer, the LED shining from the back through the sensor does not deliver sufficient light intensity for the high-speed imaging. The glass slide is coated with indium tin oxide (ITO) which is transparent in the visible light spectrum [109], thus ensuring a visibility of the microspheres. The ITO coating is conductive and thereby mitigates electrostatic forces that might build up in glass substrate.

From the recording in Fig. 7.9, it can be established that the time from the first movement of a microsphere until all microspheres have come to a rest, is 53 ms. At $t = 0$ ms, a single microsphere starts rolling in the direction of gravity. At $t = 4$ ms the microsphere collides with other spheres and causes the whole bulk to move. At first, the bulk moves slowly as the microspheres have to overcome friction and adhesion forces between each other. From $t = 16$ ms onwards, the major movement of all microspheres takes place until $t = 44$ ms. Finally, the microspheres come to rest. Based on the average of several recordings, the response time of the tilt sensor is established around 50 ms.

In chapter 5, it was determined that it is easier for a single microsphere to start rolling than for the whole bulk to start sliding, due to the increased friction coefficient of an Au-SU-8 contact compared to an Au-Au contact. The rolling time t of a microsphere crossing from one side of the cavity to the other can be determined by the formula describing a sphere accelerating down a tilted plane according to

$$t = \sqrt{\frac{2 \cdot d}{\sin(\beta_d) \cdot g}} \quad (7.3)$$

where d is the rolling distance and β_d is the tilt of the sensor plane which the microsphere experiences in direction of travel. For the microspheres in Fig. 7.9, this angle is around $\beta_d = 35^\circ$. For a $d = 1.5$ mm which is the distance covered by the microsphere initiating the movement, the rolling time is calculated to $t = 23$ ms. In the image recording, the microsphere requires around 40 ms which can be attributed to collisions between the microspheres and friction which slow down the rolling movement.

The measured response time of around 50 ms is in line with characteristics of current state of the art tilt sensors, which have been reported to have response times in the range of around 100 ms [44].

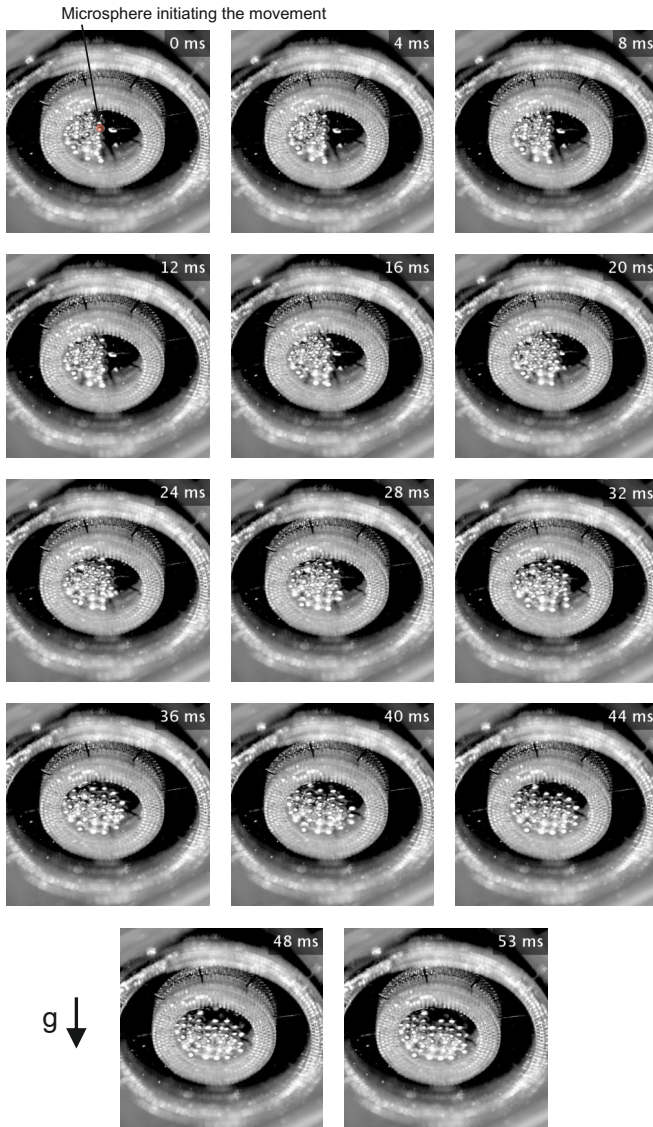


Figure 7.9: High-speed image recording of microsphere movement inside cavity at $\beta = 50^\circ$.

In chapter 7.2.4, the electrical response time will be established to be comparable with the visually determined response time.

7.2.4 Dynamic performance

In chapter 7.2.2, we evaluated the sensor in a static condition. Bearing in mind that the microspheres require around 50 ms to obtain a new position inside the cavity, we also performed a dynamic evaluation of the tilt sensor. This provides insight into the influence of dynamic parameters onto the sensor output.

The connection pads of the tilt sensor are connected through pull-up resistors to an oscilloscope to measure the states of the contact pads. The temporal resolution was set to 1 ms. Again, the sensor plane was tilted to $\beta = 50^\circ$ to ensure a reliable electrical contact as determined in chapter 5 and a low hysteresis (see chapter 7.2.2). The tilt angle was changed from 0° to 360° . Several recordings were performed with rotation speeds between 10 rpm and 60 rpm.

While the tilt sensor is rotating, the centripetal force acts upon the microspheres. Thus, the normal force onto the cavity boundaries increases which in return increases the friction. The maximal centripetal acceleration a_c can be determined to

$$a_c = \omega^2 r_{cavity} = \left(60 \text{ min}^{-1} \cdot 2\pi\right)^2 \cdot 1 \text{ mm} = 0.04 \text{ m s}^{-2} \quad (7.4)$$

with ω as the angular velocity of the rotation. The resulting a_c is three magnitudes smaller than the acceleration of gravity and can be neglected as an influence on the microsphere movement.

The results for a single rotation at speeds of 10 rpm and 60 rpm are depicted in Fig. 7.10a and Fig. 7.10b, respectively. Each measured combination of states of the contact pads is converted with the respective look-up table (similar to Tab. 2.1) to a tilt angle. If this converted value corresponds to the value of the applied tilt, it is classified as a correct output (black square), in the other case it is classified as a wrong output (red circle). In case the combination of states does not yield an entry in the look-up table, the measurement is classified as an artefact (blue bars at the bottom of the graph).

Additional analysis of the detailed output signals of each contact pad reveal the average electrical response time is around 50 ms, comparable to the timescale of the microsphere movement. This manifests itself that, during the rolling of the microspheres, the state of a contact oscillates between *active* and *inactive* until the microspheres come to

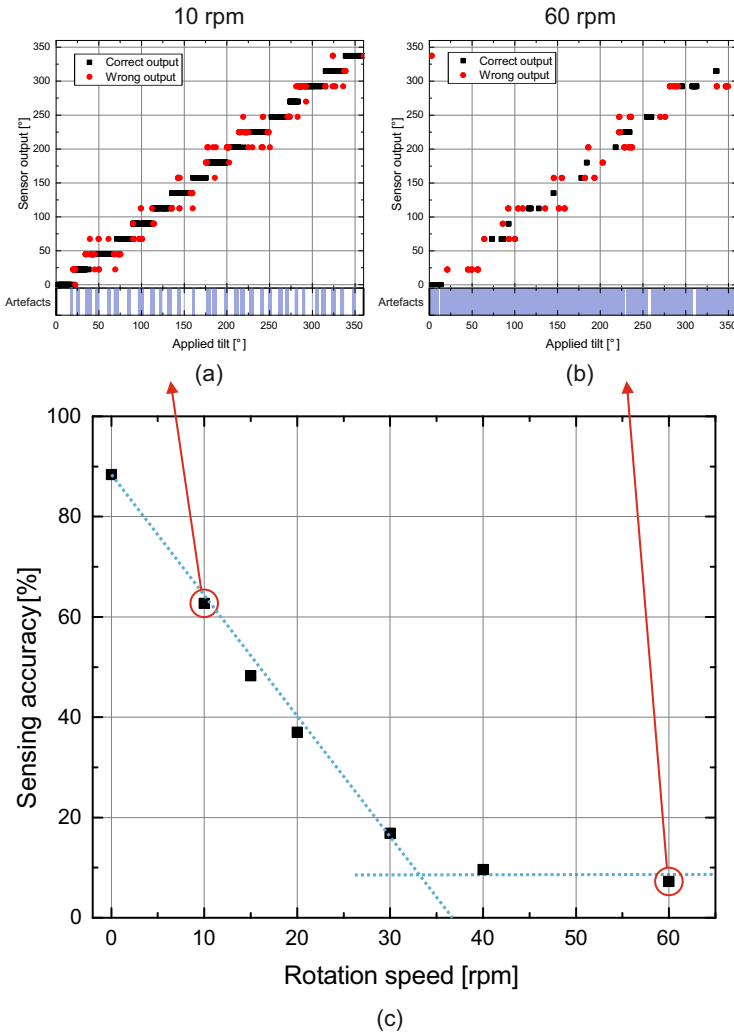


Figure 7.10: (a) Sensor output at a rotation speed of 10 rpm and $\beta = 50^\circ$; (b) Sensor output at a rotation speed of 60 rpm and $\beta = 50^\circ$; (c) Sensing accuracy for rotation speeds between 0 rpm and 60 rpm and $\beta = 50^\circ$.

rest again. This oscillation leads to artefacts in the measurement as a combination of states can occur which is not listed in the look-up table

and can therefore not be classified.

During the movement of the microspheres of 50 ms, the sensor changes its tilt angle by around 3° at 10 rpm and by 18° at 60 rpm. As 18° is larger than the hysteresis angle of 10° , a rotation speed of 60 rpm keeps the microspheres constantly rolling inside the cavity which leads to measurement artefacts most of the time.

The amount of correctly measured tilt sensor outputs (black squares) is set into relation to the total number of acquired measurement points and defined as the sensing accuracy. Fig. 7.10c shows the results for the sensing accuracy with respect to the applied rotation speed. The sensing accuracy declines with increasing rotation speed until it reaches a saturation value of around 9% for rotation speeds higher than 30 rpm. The linear decline of accuracy up to 30 rpm is due to the increased relative amount of time that the microspheres spend rolling inside the cavity. With a microsphere movement time of 50 ms and a hysteresis of 10° (see chapter 7.2.2), the microspheres are continuously moving for rotation speeds larger than 33 rpm. As the state of a contact pad oscillates while microspheres are rolling across the pad, the contact pad states are not predictable, which makes the sensor output non-deterministic and results in a sensing accuracy of less than 10%.

The tilt sensor is best operated in static applications with no movement during the signal acquisition. If the sensor is operated in dynamic conditions, a rotation speed of 20 rpm or an angular velocity of 2.1 rad/min, respectively, should not be exceeded to achieve a correct output signal in more than 50% of the acquisitions.

7.3 Conclusion

In this section we examined the characteristics of the tilt switch and tilt sensor. It was observed that the tilt switch has a make angle of 5° and a break angle of 30° . After bending to a radius of 5 cm and reflattening the sensor is still operational without changing the output characteristics.

We identified that the tilt sensor should be operated at angles of the sensor plane $\beta \geq 50^\circ$ to ensure a minimum in hysteresis. The examined 4-contact and 8-contact tilt sensors exhibit a hysteresis of less than 10° in the static states. The time scale of the microsphere movements inside the cavity is around 50 ms which allows to operate the sensor at rotation speeds up to 20 rpm if an accuracy higher than 50% is desired.

8

Conclusion

A flexible tilt sensor was designed and evaluated. Different approaches for fabrication were presented. A comprehensive model of the sensor was introduced which provides insight on the influence of different design parameters.

An outlook discusses possible further improvements and applications of the tilt sensor concept.

8.1 Summary and achievements

Research has covered different types of tilt sensors with varying sensing principles, achieving a wide range of possible tilt domains and resolutions, targeting specific applications. However, no tilt sensor has been presented which is flexible and delivers a digital output signal.

In this thesis, we pursued the idea of a tilt sensor with microspheres as a pendulum, fabricated on plastic.

The major contributions of this thesis are the following:

- A flexible tilt sensor has been designed and fabricated on polyimide foil, using standard clean room processes at temperatures of less than 200 °C. This allows the combination of the sensor with other electronics and sensors on a single polyimide substrate which will enable future, more complex systems. This is a further step towards the development of completely flexible, wearable electronics which allow for new smart textiles, e.g. for health care.
- The use of microspheres with a diameter of 250 μm as a pendulum was assessed, especially considering the contact mechanics which influence the performance of the microspheres. Here a balance needs to be found between a reliable electrical contact and minimizing the adhesion forces of cavity and pendulum.
- A comprehensive model of the tilt sensor was developed and evaluated identifying important parameters for the sensor design. The number of contact pads and the amount of microspheres in the cavity are the critical parameters which have a dominant influence on the resolution and non-linearity.
- The characteristics of the tilt sensor concerning static behavior as well as the dynamics were evaluated. In order to reduce the sensor hysteresis to a minimum of 10°, the sensor plane is tilted by 50°. The response time of the tilt sensor was identified. As a result an application of the sensor in dynamic systems is not desirable.

8.2 Scalability and limitations

The angular resolution of the tilt sensor is limited by the number of contact pads patterned on the substrate surface. An increase of the

number of contact pads with constant cavity radius however reduces the area per contact pad in the cavity. With a cavity radius $r_{cavity} = 1000 \mu\text{m}$ and for $N \geq 12$ the width of the contact pads at the edge of the cavity is less than $250 \mu\text{m}$. In this case, a reliable electrical connection of the microsphere with the contact pad cannot be guaranteed. Therefore, for a number of contact pads $N \geq 12$ the size of the cavity needs to be increased to increase the width of the contact pad inside the cavity.

Alternatively, the diameter of the microspheres could be reduced. However, we have seen that for sphere diameters smaller than $250 \mu\text{m}$ the parasitic forces such as adhesion to the cavity wall dominate the gravitational forces, hindering a free movement of the microspheres. In addition, the reduced weight of the microsphere also creates less pressure on the contact pads which has a negative influence on the electrical contact with the contact pads.

The resolution of the sensor can be chosen according to the requirements of the application, however an improved resolution requires a larger size of the sensor.

8.3 Conclusions

The following conclusions can be drawn from the results of this thesis:

- The non-linearity of the tilt sensor can be reduced to a minimum by selecting the amount of microspheres according to the size of the cavity and the number of contact pads. For an even number of contact pads, the non-linearity is at a minimum when the pendulum covers half of the area of the cavity.
- It is possible to fabricate a flexible tilt sensor using standard clean room processes.
- Reducing the size of the microspheres below a diameter of $250 \mu\text{m}$ comes to a limit because adhesion forces such as Van-der-Waals forces start to dominate the gravitational forces. Equally, the pressure between microsphere and contact pad to create a reliable electrical contact becomes marginal.
- The time scale of the microsphere movement inside the cavity does not allow to operate the sensor in highly dynamic applications.

8.4 Outlook

The sensing principle proved its functionality. Yet, we see a number of areas where further development of the presented results can lead to new application fields.

8.4.1 Materials and technology

Improvements in the materials and fabrication technology can enhance the bendability of the sensor and further reduce the size of the sensing structure.

We showed that the sensor is flexible and can be bent down to a radius of 2 cm with the SU-8 pillar structure. However, the height of the pillar structure combined with the epoxy glue increases the stiffness significantly in the area of the sensing structure. This is a downside for an unobtrusive integration into textiles, where the stiffness is a negative factor.

By identifying alternative sealing chemicals, e.g. a silicone glue which has a lower Young's modulus, the stiffness of the sensing structure could be reduced and in return even allowed for a decreased bending radius. The current sensing structure also consists of a double ring of SU-8 pillars with the outer ring used to apply the epoxy while avoiding that the glue reaches the inner side of the cavity and interacts with the microspheres. While an alternative glue would be one option for improvement, other sealing and packaging approaches could be developed to close the cavity and drop the outer ring of SU-8 pillars. This would allow to even further decrease the size of the tilt sensor, improving the unobtrusiveness.

A fabrication process which is performed entirely in a sealed environment with no humidity is desirable to mitigate the build-up of a water film on the substrate and microsphere surface. We showed that this film reduces the operation range of the tilt sensor. By avoiding wet surfaces, the tilt sensor operation range might be extended.

8.4.2 Sensor design

In this work, the focus for the cavity of the tilt sensor was always on a circular design with regularly arranged contact pads. This allowed to develop a comprehensive model of the tilt sensor and understand the influence of the design parameters on the sensor performance.

However, by modifying the arrangement of the contact pads and the shape of the cavity, we believe that the sensor can be optimized to target specific applications.

The number of the contact pads on one side of the cavity can be increased, leading to an increased resolution, while the other side of the cavity has a lower number of contact pads. The tilt sensor would then offer a rough resolution with the sensor tilted in one direction and an improved resolution when tilted to the other direction.

The cavity wall of SU-8 pillars is structured by photolithography. This means, that arbitrary shapes of the cavity can be realized with the appropriate lithography mask. The cavity can be not only circular, but also have e.g. areas that keep microspheres from rolling out of a trench again once they have rolled inside. Logistics use sensors with a cavity where a sphere rolls into trenches when tilted above a certain threshold angle and so allow the indication of the maximum applied tilt during the transport [110]. By combining this principle with our tilt sensor, a miniaturized, electronic version of this sensor can be realized.

8.4.3 Sensor readout

The readout of the tilt sensor has been performed by connecting the device with cables to a multimeter which defines the current state of each contact pad. With the respective look-up table these states are then translated into the tilt angle. We see improvement possibilities regarding the state detection as well as the use of look-up table.

As one advantage of the tilt sensor, it does not require an active power supply and for a readout merely the state of each contact pad is important. Therefore, we envision a wireless passive readout of the sensor with a resonant circuit. Each contact pad is connected to a different capacitance and all pads are then connected with a single coil. Depending on the state of the contact pads, the coil is electrically connected to a varying overall capacitance which leads to different resonance frequencies. This shift in resonance frequency of the LC resonant circuit can be detected with respective equipment, even a readout via Near Field Communication (NFC) with a smartphone can be possible. Other wireless LC sensors have already been demonstrated, such as humidity [111] or pressure sensors [112]. We have also shown a proof of concept by combining off-the-shelf tilt switches with Radio Frequency Identification (RFID) chips to build a die which can be read out wirelessly [113].

The use of a look-up table could be replaced by the application of respective algorithms. When evaluating the dynamics of the tilt sensor, we noticed that during the movement of the microspheres they do not reliably connect with the contact pads. This leads to undefined states in the sensor output which are not listed in the look-up table. By developing an appropriate algorithm, these undefined states could also be translated into a respective tilt angle, mitigating a missing active state of the tilt sensor. This would improve the sensor performance in a dynamic environment and decrease the number of motion artefacts.

Appendix

Strain induced by bending

The strain ϵ induced in a device with the height h and the length l when bent to a bending radius r is determined as follows:

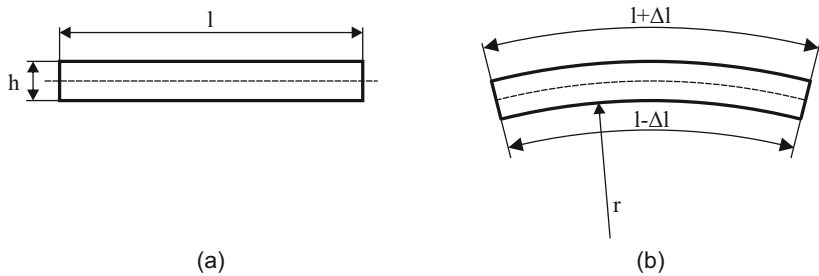


Figure A.1: Device with a height h and a length l (a) flat state and (b) bent to a bending radius r . The neutral axis is depicted as a dashed line.

The device is shown in a flat state in Fig. A.1a. When bent to a bending radius r (shown in Fig. A.1b), the upper part of the device is elongated, the lower part is compressed. The neutral axis, i.e. where no longitudinal stress is induced, is indicated with a dashed line.

The strain ϵ is defined as:

$$\epsilon = \frac{\Delta l}{l} \quad (\text{A.1})$$

The length b of a circular arc can be calculated according to

$$b = \pi \cdot r \cdot \frac{\alpha}{180^\circ} \quad (\text{A.2})$$

where α is the mid point angle.

From this, the following equations are determined:

$$l = \pi \cdot r \cdot \frac{\alpha}{180^\circ} \quad (\text{A.3})$$

$$l + \Delta l = \pi \cdot \left(r + \frac{h}{2} \right) \cdot \frac{\alpha}{180^\circ} \quad (\text{A.4})$$

The relation of Eq. A.3 and Eq. A.4 is

$$\frac{l + \Delta l}{l} = \frac{\pi \cdot \left(r + \frac{h}{2} \right) \cdot \frac{\alpha}{180^\circ}}{\pi \cdot r \cdot \frac{\alpha}{180^\circ}} = 1 + \frac{h}{2r} \quad (\text{A.5})$$

The left side of Eq. A.5 simplifies to $1 + \epsilon$, therefore

$$\epsilon = \frac{h}{2r} \quad (\text{A.6})$$

Sphere resistance R_{sp}

We calculate the resistance of a sphere with the radius r which is contacted on opposite sides by a cylinder with the radius a . The current flows only through the coating of the microsphere which has a thickness h .

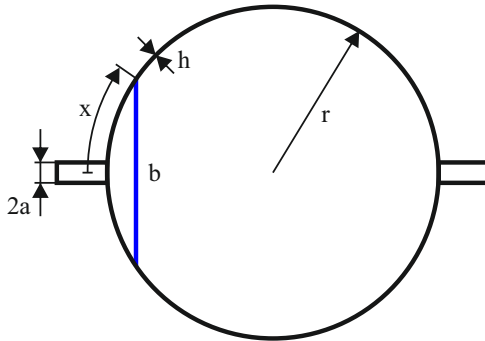


Figure A.2: Sphere with a radius r , contacted on opposite sides by a cylinder with a radius a . The thickness of the sphere coating through which the current flows is h .

To calculate the resistance R , we integrate the incremental resistance along the surface coordinate x from a to $\pi r - a$ with ρ as the electrical resistivity.

$$R = \int_a^{\pi r - a} \frac{\rho}{U(x) \cdot h} dx \quad (\text{A.7})$$

The diameter $b(x)$ at a given value of x can be determined by

$$b(x) = 2 \sin\left(\frac{x}{r}\right) r. \quad (\text{A.8})$$

The circumference $U(x)$ is then calculated according to

$$U(x) = b(x)\pi = 2\pi r \sin\left(\frac{x}{r}\right). \quad (\text{A.9})$$

With Eq. A.9, Eq. A.7 equates to

$$\begin{aligned} R &= \int_a^{\pi r - a} \frac{\rho}{2\pi r \sin\left(\frac{x}{r}\right) \cdot h} dx \\ &= \frac{\rho}{2\pi h r} \int_a^{\pi r - a} \frac{1}{\sin\left(\frac{x}{r}\right)} dx \end{aligned} \quad (\text{A.10})$$

The integral is determined to

$$\int \frac{1}{\sin\left(\frac{x}{r}\right)} dx = \left[r \cdot \ln\left(\tan\left(\frac{x}{2r}\right)\right) \right] \quad (\text{A.11})$$

With Eq. A.11 in Eq. A.10, we determine the resistance to

$$R = \frac{\rho}{2\pi h} \left[\ln\left(\tan\left(\frac{x}{2r}\right)\right) \right]_a^{\pi r - a} \quad (\text{A.12})$$

Bibliography

- [1] K. Cherenack, T. Kinkeldei, C. Zysset, and G. Tröster, "Woven thin-film metal interconnects," *IEEE Electron Device Letters*, vol. 31, no. 7, pp. 740–742, 2010.
- [2] Y. Moser and M. Gijs, "Miniaturized flexible temperature sensor," *Journal of Microelectromechanical Systems*, vol. 16, no. 6, pp. 1349–1354, 2007.
- [3] S. C. Mannsfeld, B. C. Tee, R. M. Stoltenberg, C. V. H. Chen, S. Barman, B. V. Muir, A. N. Sokolov, C. Reese, and Z. Bao, "Highly sensitive flexible pressure sensors with microstructured rubber dielectric layers," *Nature materials*, vol. 9, no. 10, pp. 859–864, 2010.
- [4] T. Kinkeldei, C. Zysset, N. Münzenrieder, and G. Tröster, "An electronic nose on flexible substrates integrated into a smart textile," *Sensors and Actuators B: Chemical*, vol. 174, pp. 81–86, 2012.
- [5] N. Münzenrieder, K. Cherenack, and G. Tröster, "The effects of mechanical bending and illumination on the performance of flexible igzo tfts," *Electron Devices, IEEE Transactions on*, vol. 58, no. 7, pp. 2041–2048, July 2011.
- [6] J. Seiter, S. Feese, B. Arrrich, G. Tröster, O. Amft, L. Macrea, and K. Maurer, "Activity monitoring in daily life as an outcome measure for surgical pain relief intervention using smartphones," in *Proceedings of the 17th annual international symposium on International symposium on wearable computers*, 2013, pp. 127–128.
- [7] S.-W. Lee and K. Mase, "Activity and location recognition using wearable sensors," *Pervasive Computing, IEEE*, vol. 1, no. 3, pp. 24–32, 2002.
- [8] C. Strohrmann, H. Harms, C. Kappeler-Setz, and G. Tröster, "Monitoring kinematic changes with fatigue in running using body-worn sensors," *IEEE Transactions on Information Technology in Biomedicine*, vol. 16, no. 5, pp. 938–990, 2012.

- [9] H. Harms, O. Amft, and G. Tröster, "Wearable therapist: sensing garments for supporting children improve posture," in *11th International Conference on Ubiquitous Computing, Ubicomp 2009*, 2009.
- [10] R. Hyde, L. Ketteringham, S. Neild, and R. Jones, "Estimation of upper-limb orientation based on accelerometer and gyroscope measurements," *IEEE Transactions on Biomedical Engineering*, vol. 55, no. 2, pp. 746–754, Feb 2008.
- [11] H. Gjoreski, M. Lustrek, and M. Gams, "Accelerometer placement for posture recognition and fall detection," in *2011 7th International Conference on Intelligent Environments (IE)*, 2011, pp. 47–54.
- [12] S. Sukkariéh, P. Gibbens, B. Grocholsky, K. Willis, and H. F. Durrant-Whyte, "A low-cost, redundant inertial measurement unit for unmanned air vehicles," *The International Journal of Robotics Research*, vol. 19, no. 11, pp. 1089–1103, 2000.
- [13] T. Toriyama and S. Sugiyama, "Analysis of piezoresistance in p-type silicon for mechanical sensors," *Microelectromechanical Systems, Journal of*, vol. 11, no. 5, pp. 598–604, 2002.
- [14] S. Huang, X. Li, Z. Song, Y. Wang, H. Yang, L. Che, and J. Jiao, "A high-performance micromachined piezoresistive accelerometer with axially stressed tiny beams," *Journal of Micromechanics and Microengineering*, vol. 15, no. 5, p. 993, 2005.
- [15] H. Chen, M. Bao, H. Zhu, and S. Shen, "A piezoresistive accelerometer with a novel vertical beam structure," *Sensors and Actuators A: Physical*, vol. 63, no. 1, pp. 19 – 25, 1997.
- [16] A. Partridge, J. Reynolds, B. Chui, E. Chow, A. Fitzgerald, L. Zhang, N. I. Maluf, and T. Kenny, "A high-performance planar piezoresistive accelerometer," *Microelectromechanical Systems, Journal of*, vol. 9, no. 1, pp. 58–66, 2000.
- [17] R. Amarasinghe, D. V. Dao, T. Toriyama, and S. Sugiyama, "Development of miniaturized 6-axis accelerometer utilizing piezoresistive sensing elements," *Sensors and Actuators A: Physical*, vol. 134, no. 2, pp. 310 – 320, 2007.

- [18] J. Sim, D. Kim, Y. Bae, K. Nam, and J. Lee, "Six-beam piezoresistive accelerometer with self-cancelling cross-axis sensitivity," *Electronics Letters*, vol. 34, no. 5, pp. 497–499, Mar 1998.
- [19] A. R. Atwell, R. S. Okojie, K. T. Kornegay, S. L. Roberson, and A. Beliveau, "Simulation, fabrication and testing of bulk micro-machined 6h-sic high-g piezoresistive accelerometers," *Sensors and Actuators A: Physical*, vol. 104, no. 1, pp. 11 – 18, 2003.
- [20] H. Luo, G. Zhang, L. Carley, and G. Fedder, "A post-cmos micro-machined lateral accelerometer," *Microelectromechanical Systems, Journal of*, vol. 11, no. 3, pp. 188–195, 2002.
- [21] J. Chae, H. Kulah, and K. Najafi, "A monolithic three-axis micro-g micromachined silicon capacitive accelerometer," *Journal of Microelectromechanical Systems*, vol. 14, no. 2, pp. 235–242, 2005.
- [22] C.-M. Sun, M.-H. Tsai, Y.-C. Liu, and W. Fang, "Implementation of a monolithic single proof-mass tri-axis accelerometer using cmos-mems technique," *IEEE Transactions on Electron Devices*, vol. 57, no. 7, pp. 1670–1679, 2010.
- [23] I. Gönenli, Z. Celik-Butler, and D. Butler, "Surface micromachined mems accelerometers on flexible polyimide substrate," *IEEE Sensors Journal*, vol. 11, no. 10, pp. 2318–2326, 2011.
- [24] F. Mailly, A. Giani, A. Martinez, R. Bonnot, P. Temple-Boyer, and A. Boyer, "Micromachined thermal accelerometer," *Sensors and Actuators A: Physical*, vol. 103, no. 3, pp. 359 – 363, 2003.
- [25] U. Mescheder and S. Majer, "Micromechanical inclinometer," *Sensors and Actuators A: Physical*, vol. 60, no. 1, pp. 134 – 138, 1997.
- [26] L. Tang, K. Zhang, S. Chen, G. Zhang, and G. Liu, "MEMS inclinometer based on a novel piezoresistor structure," *Microelectronics Journal*, vol. 40, no. 1, pp. 78 – 82, 2009.
- [27] C. Smith, A. Villanueva, and S. Priya, "Aurelia aurita bio-inspired tilt sensor," *Smart Materials and Structures*, vol. 21, no. 10, p. 105015, 2012.
- [28] C. H. Lee and S. S. Lee, "Capacitive tilt sensor using metallic ball," in *Proceedings of ASME 2009 International Mechanical Engineering Congress and Exposition*, vol. 12, 2009, pp. 445–448.

- [29] J. Liang, F. Kohsaka, X. Li, K. Kunitomo, and T. Ueda, "Characterization of a quartz MEMS tilt sensor with 0.001° precision," in *International Solid-State Sensors, Actuators and Microsystems Conference, 2009. TRANSDUCERS 2009.*, 2009, pp. 308–310.
- [30] L. Zhao and E. Yeatman, "Micro capacitive tilt sensor for human body movement detection," in *4th International Workshop on Wearable and Implantable Body Sensor Networks (BSN 2007)*, ser. IFMBE Proceedings, S. Leonhardt, T. Falck, and P. Mähönen, Eds. Springer Berlin Heidelberg, 2007, vol. 13, pp. 195–200.
- [31] R. Olaru and D. Dragoi, "Inductive tilt sensor with magnets and magnetic fluid," *Sensors and Actuators A: Physical*, vol. 120, no. 2, pp. 424–428, 2005.
- [32] L. Rovati and S. Cattini, "Contactless two-axis inclination measurement system using planar flux-gate sensor," *IEEE Transactions on Instrumentation and Measurement*, vol. 59, no. 5, pp. 1284–1293, 2010.
- [33] T. G. Constandinou and J. Georgiou, "Micro-optoelectromechanical tilt sensor," *Journal of Sensors*, vol. 2008, 2008.
- [34] J.-H. Wu, K.-Y. Horng, S.-L. Lin, and R.-S. Chang, "A two-axis tilt sensor based on optics," *Measurement Science and Technology*, vol. 17, no. 4, p. N9, 2006.
- [35] L. Amaral, O. Frazao, J. Santos, and A. Ribeiro, "Fiber-optic inclinometer based on taper michelson interferometer," *IEEE Sensors Journal*, vol. 11, no. 9, pp. 1811–1814, 2011.
- [36] O. Frazao, R. Falate, J. L. Fabris, J. L. Santos, L. A. Ferreira, and F. M. Araújo, "Optical inclinometer based on a single long-period fiber grating combined with a fused taper," *Optics Letters*, vol. 31, no. 20, pp. 2960–2962, 2006.
- [37] L.-Y. Shao and J. Albert, "Compact fiber-optic vector inclinometer," *Optics Letters*, vol. 35, no. 7, pp. 1034–1036, 2010.
- [38] B.-O. Guan, H.-Y. Tam, and S.-Y. Liu, "Temperature-independent fiber bragg grating tilt sensor," *IEEE Photonics Technology Letters*, vol. 16, no. 1, pp. 224–226, 2004.

- [39] X. Dong, C. Zhan, K. Hu, P. Shum, and C. C. Chan, "Temperature-insensitive tilt sensor with strain-chirped fiber bragg gratings," *IEEE Photonics Technology Letters*, vol. 17, no. 11, pp. 2394–2396, 2005.
- [40] B.-J. Peng, Y. Zhao, Y. Zhao, and J. Yang, "Tilt sensor with fbg technology and matched fbg demodulating method," *IEEE Sensors Journal*, vol. 6, no. 1, pp. 63–66, 2006.
- [41] H. Bao, X. Dong, L.-Y. Shao, C.-L. Zhao, and S. Jin, "Temperature-insensitive 2-d tilt sensor by incorporating fiber bragg gratings with a hybrid pendulum," *Optics Communications*, vol. 283, no. 24, pp. 5021–5024, 2010.
- [42] J. H. Lee and S. S. Lee, "Electrolytic tilt sensor fabricated by using electroplating process," *Sensors and Actuators A: Physical*, vol. 167, no. 1, pp. 1–7, 2011.
- [43] H. Jung, C. J. Kim, and S. H. Kong, "An optimized MEMS-based electrolytic tilt sensor," *Sensors and Actuators A: Physical*, vol. 139, no. 1 - 2, pp. 23–30, 2007.
- [44] J. C. Choi, Y. C. Choi, J. K. Lee, and S. H. Kong, "Miniaturized dual-axis electrolytic tilt sensor," *Japanese Journal of Applied Physics*, vol. 51, no. 6, p. 06FL13, 2012.
- [45] W. Bin, M. M. Hossain, and S. H. Kong, "Pdms-based two-axis inclinometer with a 360-degree measuring range," *Sensors and Actuators A: Physical*, vol. 239, pp. 54–60, 2016.
- [46] R. A. Yotter, R. R. Baxter, S. Ohno, S. D. Hawley, and D. M. Wilson, "On a micromachined fluidic inclinometer," in *12th International Conference on Solid-State Sensors, Actuators and Microsystems (TRANSDUCERS)*, vol. 2, 2003, pp. 1279–1282.
- [47] A. B. A. Manaf, K. Nakamura, and Y. Matsumoto, "Characterization of miniaturized one-side-electrode-type fluid-based inclinometer," *Sensors and Actuators A: Physical*, vol. 144, no. 1, pp. 74–82, 2008.
- [48] B. Salvador, A. Luque, and J. M. Quero, "Microfluidic capacitive tilt sensor using pcb-mems," in *2015 IEEE International Conference on Industrial Technology (ICIT)*, 2015, pp. 3356–3360.

- [49] H. Ueda, H. Ueno, K. Itoigawa, and T. Hattori, "Micro capacitive inclination sensor utilizing dielectric nano-particles," in *19th IEEE International Conference on Micro Electro Mechanical Systems (MEMS)*, 2006, pp. 706–709.
- [50] D. Benz, T. Botzelmann, H. Kück, and D. Warkentin, "On low cost inclination sensors made from selectively metallized polymer," *Sensors and Actuators A: Physical*, vol. 123-124, no. 0, pp. 18–22, 2005.
- [51] O. Baltag, D. Costandache, and A. Salceanu, "Tilt measurement sensor," *Sensors and Actuators A: Physical*, vol. 81, no. 1 - 3, pp. 336–339, 2000.
- [52] B. Ando, A. Ascia, and S. Baglio, "A ferrofluidic inclinometer in the resonant configuration," *IEEE Transactions on Instrumentation and Measurement*, vol. 59, no. 3, pp. 558–564, 2010.
- [53] D. Welch, J. Georgiou, and J. B. Christen, "Fully differential current-mode MEMS dual-axis optical inclination sensor," *Sensors and Actuators A: Physical*, vol. 192, no. 0, pp. 133 – 139, 2013.
- [54] J. S. Bajic, D. Z. Stupar, L. M. Manojlovic, M. P. Slankamenac, and M. B. Zivanov, "A simple, low-cost, high-sensitivity fiber-optic tilt sensor," *Sensors and Actuators A: Physical*, vol. 185, no. 0, pp. 33–38, 2012.
- [55] X. Zhang, K. Ni, C. Zhao, M. Ye, and Y. Jin, "Tilt sensor based on intermodal photonic crystal fiber interferometer," *Photonic Sensors*, vol. 4, no. 3, pp. 209–214, 2014.
- [56] J. Courteaud, P. Combette, N. Crespy, G. Cathebras, and A. Giani, "Thermal simulation and experimental results of a micromachined thermal inclinometer," *Sensors and Actuators A: Physical*, vol. 141, no. 2, pp. 307–313, 2008.
- [57] S. Billat, H. Glosch, M. Kunze, F. Hedrich, J. Frech, J. Auber, W. Lang, H. Sandmaier, and W. Wimmer, "Convection-based micromachined inclinometer using SOI technology," in *The 14th IEEE International Conference on Micro Electro Mechanical Systems (MEMS)*, 2001, pp. 159–161.

- [58] S. Billat, H. Glosch, M. Kunze, F. Hedrich, J. Frech, J. Auber, H. Sandmaier, W. Wimmer, and W. Lang, "Micromachined inclinometer with high sensitivity and very good stability," *Sensors and Actuators A: Physical*, vol. 97–98, pp. 125–130, 2002.
- [59] J. C. Choi, Y. C. Choi, J. K. Lee, and S. H. Kong, "Electrolytic tilt sensor with domed cap for improved performance," *Japanese Journal of Applied Physics*, vol. 52, no. 6S, p. 06GL13, 2013.
- [60] C. H. Lin and S. M. Kuo, "Micro-impedance inclinometer with wide-angle measuring capability and no damping effect," *Sensors and Actuators A: Physical*, vol. 143, no. 1, pp. 113–119, 2008.
- [61] C. H. Lee and S. S. Lee, "Study of capacitive tilt sensor with metallic ball," *ETRI Journal*, vol. 36, no. 3, pp. 361–366, 2014.
- [62] L. Büthe, C. Vogt, L. Petti, G. Cantarella, G. Tröster, and N. Münzenrieder, "Digital output flexible tilt sensor with conductive microspheres," in *2015 IEEE Sensors conference*, 2015, pp. 1–4.
- [63] J. Cheng, P. Lukowicz, N. Henze, A. Schmidt, O. Amft, G. A. Salvatore, and G. Tröster, "Smart textiles: From niche to mainstream," *IEEE Pervasive Computing*, vol. 12, no. 3, pp. 81–84, 2013.
- [64] L. Petti, N. Munzenrieder, G. Salvatore, C. Zysset, T. Kinkeldei, L. Buthe, and G. Troster, "Influence of mechanical bending on flexible ingazno-based ferroelectric memory tfts," *IEEE Transactions on Electron Devices*, vol. 61, no. 4, pp. 1085–1092, 2014.
- [65] T. Kinkeldei, C. Zysset, K. Cherenack, and G. Tröster, "A textile integrated sensor system for monitoring humidity and temperature," in *16th International Solid-State Sensors, Actuators and Microsystems Conference (TRANSDUCERS)*, 2011, pp. 1156–1159.
- [66] C. Zysset, N. Munzenrieder, L. Petti, L. Buthe, G. Salvatore, and G. Troster, "Igzo tft-based all-enhancement operational amplifier bent to a radius of 5 mm," *IEEE Electron Device Letters*, vol. 34, no. 11, pp. 1394–1396, 2013.
- [67] M. C. Buzzeo, C. Hardacre, and R. G. Compton, "Use of room temperature ionic liquids in gas sensor design," *Analytical Chemistry*, vol. 76, no. 15, pp. 4583–4588, 2004.

- [68] J. F. Brennecke and E. J. Maginn, "Ionic liquids: Innovative fluids for chemical processing," *AIChE Journal*, vol. 47, no. 11, pp. 2384–2389, 2001.
- [69] S. Pandey, "Analytical applications of room-temperature ionic liquids: A review of recent efforts," *Analytica Chimica Acta*, vol. 556, no. 1, pp. 38–45, 2006.
- [70] H. Zhao, Z.-C. Liang, and F. Li, "An improved model for the conductivity of room-temperature ionic liquids based on hole theory," *Journal of Molecular Liquids*, vol. 149, no. 3, pp. 55–59, 2009.
- [71] M. Galinski, A. Lewandowski, and I. Stepniak, "Ionic liquids as electrolytes," *Electrochimica Acta*, vol. 51, no. 26, pp. 5567–5580, 2006.
- [72] L. P. N. Rebelo, J. N. Canongia Lopes, J. M. S. S. Esperança, and E. Filipe, "On the critical temperature, normal boiling point, and vapor pressure of ionic liquids," *The Journal of Physical Chemistry B*, vol. 109, no. 13, pp. 6040–6043, 2005.
- [73] M. J. Earle, J. M. Esperança, M. A. Gilea, J. N. C. Lopes, L. P. Rebelo, J. W. Magee, K. R. Seddon, and J. A. Widegren, "The distillation and volatility of ionic liquids," *Nature*, vol. 439, no. 7078, pp. 831–834, 2006.
- [74] G. K. Batchelor, *An introduction to fluid dynamics*. Cambridge university press, 2000.
- [75] G. Yu, D. Zhao, L. Wen, S. Yang, and X. Chen, "Viscosity of ionic liquids: Database, observation, and quantitative structure-property relationship analysis," *AIChE Journal*, vol. 58, no. 9, pp. 2885–2899, 2012.
- [76] T. Cassagneau and F. Caruso, "Contiguous silver nanoparticle coatings on dielectric spheres," *Advanced Materials*, vol. 14, no. 10, pp. 732–736, 2002.
- [77] iepco AG, "Products for surface treatment," accessed 27.09.2016. [Online]. Available: <http://www.iepco.ch/en/products/additives-and-raw-materials/products-for-surface-treatment>

- [78] J. Soulages, T. Schweizer, D. Venerus, J. Hostettler, F. Mettler, M. Kröger, and H. Öttinger, "Lubricated optical rheometer for the study of two-dimensional complex flows of polymer melts," *Journal of Non-Newtonian Fluid Mechanics*, vol. 150, no. 1, pp. 43–55, 2008.
- [79] C. E. Ho, Y. M. Chen, and C. R. Kao, "Reaction kinetics of solder-balls with pads in bga packages during reflow soldering," *Journal of Electronic Materials*, vol. 28, no. 11, pp. 1231–1237, 1999.
- [80] H. Pezous, C. Rossi, M. Sanchez, F. Mathieu, X. Dollat, S. Charlot, and V. Conedera, "Fabrication, assembly and tests of a MEMS-based safe, arm and fire device," *Journal of Physics and Chemistry of Solids*, vol. 71, no. 2, pp. 75–79, 2010.
- [81] Caplinq, "Buy sac305 leadfree solder spheres solder bball online," accessed 27.09.2016. [Online]. Available: http://www.caplinq.com/buy-sac305-leadfree-solder-spheres-solder-balls-online-sac305.html?cat_id=99&parent_cat=14
- [82] S. McAllister, S. Patankar, I. F. Cheng, and D. Edwards, "Lead dioxide coated hollow glass microspheres as conductive additives for lead acid batteries," *Scripta Materialia*, vol. 61, no. 4, pp. 375–378, 2009.
- [83] R. A. Wydro, "Method of producing solder spheres," 1983, uS Patent 4,380,518.
- [84] J.-H. Lee, B. C. Moon, J. Lee, J.-T. Moon, C.-R. Oh, and J. G. Nam, "Method of manufacturing solder balls," US Patent 6,312,498, 2001.
- [85] C. Perabo, "How is a high quality solder sphere made?" accessed 02.10.2016. [Online]. Available: http://www.caplinq.com/blog/how-is-a-high-quality-solder-sphere-made_824/
- [86] S. Metz, R. Holzer, and P. Renaud, "Polyimide-based microfluidic devices," *Lab on a Chip*, vol. 1, no. 1, pp. 29–34, 2001.
- [87] S. Metz, S. Jiguet, A. Bertsch, and P. Renaud, "Polyimide and SU-8 microfluidic devices manufactured by heat-depolymerizable sacrificial material technique," *Lab Chip*, vol. 4, pp. 114–120, 2004.

- [88] L. Bütthe, C. Vogt, L. Petti, N. Münzenrieder, C. Zysset, G. A. Salvatore, and G. Tröster, "A mechanically flexible tilt switch on kapton foil with microspheres as a pendulum," in *Proceedings of Sensors and Measuring Systems 2014 17. ITG/GMA Symposium*, 2014, pp. 1–4.
- [89] U. Buder, J.-P. von Klitzing, and E. Obermeier, "Reactive ion etching for bulk structuring of polyimide," *Sensors and Actuators A: Physical*, vol. 132, no. 1, pp. 393–399, 2006.
- [90] H. Lorenz, M. Despont, N. Fahrni, N. LaBianca, P. Renaud, and P. Vettiger, "SU-8: a low-cost negative resist for MEMS," *Journal of Micromechanics and Microengineering*, vol. 7, no. 3, p. 121, 1997.
- [91] A. del Campo and C. Greiner, "SU-8: a photoresist for high-aspect-ratio and 3D submicron lithography," *Journal of Micromechanics and Microengineering*, vol. 17, no. 6, p. R81, 2007.
- [92] L. Dellmann, S. Roth, C. Beuret, G. A. Racine, H. Lorenz, M. Despont, P. Renaud, P. Vettiger, and N. F. de Rooij, "Fabrication process of high aspect ratio elastic structures for piezoelectric motor applications," in *Solid State Sensors and Actuators, 1997. TRANSDUCERS '97 Chicago., 1997 International Conference on*, vol. 1, Jun 1997, pp. 641–644 vol.1.
- [93] M. Nordström, A. Johansson, E. S. Nogueron, B. Clausen, M. Calleja, and A. Boisen, "Investigation of the bond strength between the photo-sensitive polymer SU-8 and gold," *Microelectronic Engineering*, vol. 78-79, pp. 152–157, 2005.
- [94] S. J. Lee, W. Shi, P. Maciel, and S. W. Cha, "Top-edge profile control for su-8 structural photoresist," in *Proceedings of the 15th Biennial University/Government/Industry Microelectronics Symposium*, 2003, pp. 389–390.
- [95] K. Kim, D. S. Park, H. M. Lu, W. Che, K. Kim, J.-B. Lee, and C. H. Ahn, "A tapered hollow metallic microneedle array using backside exposure of su-8," *Journal of Micromechanics and Microengineering*, vol. 14, no. 4, p. 597, 2004.
- [96] S. Hobson, "Mitigation of su-8 t-topping," *Fraunhofer USA Center for Manufacturing and Innovation*, 2003.

- [97] T. Tamai, S. Sawada, and Y. Hattori, "Deformation of crystal structure and distribution of mechanical stress in tin-plated layer under contact loading," in *2009 Proceedings of the 55th IEEE Holm Conference on Electrical Contacts*, 2009, pp. 162–167.
- [98] P. G. Slade, *Electrical contacts: principles and applications*. CRC Press, 2013.
- [99] B. H. Jang, P. H. Tseng, W. Fang, and S. W. Lin, "Extraction of micro-contact properties using a novel micromachined on-chip apparatus," in *2008 International Conference on Electronic Materials and Packaging*, Oct 2008, pp. 285–288.
- [100] C. Clay and A. Hodgson, "Water and mixed oh/water adsorption at close packed metal surfaces," *Current Opinion in Solid State and Materials Science*, vol. 9, no. 1–2, pp. 11–18, 2005.
- [101] A. Hodgson and S. Haq, "Water adsorption and the wetting of metal surfaces," *Surface Science Reports*, vol. 64, no. 9, pp. 381–451, 2009.
- [102] H. Hertz, "Über die berührung fester elastischer körper," *Journal für die reine und angewandte Mathematik*, vol. 92, pp. 156–171, 1881.
- [103] V. Popov, *Contact mechanics and friction: physical principles and applications*. Springer Science & Business Media, 2010.
- [104] J. Diao, K. Gall, and M. L. Dunn, "Surface-stress-induced phase transformation in metal nanowires," *Nature materials*, vol. 2, no. 10, pp. 656–660, 2003.
- [105] L. Kondic, R. Hartley, S. Tennakoon, B. Painter, and R. Behringer, "Segregation by friction," *EPL (Europhysics Letters)*, vol. 61, no. 6, p. 742, 2003.
- [106] E. Weisstein, "Circular segment - mathworld - a wolfram web resource," accessed 17.09.2016. [Online]. Available: <http://mathworld.wolfram.com/CircularSegment.html>
- [107] J. H. Conway and N. J. A. Sloane, *Sphere packings, lattices and groups*. Springer Science & Business Media, 2013, vol. 290.
- [108] L. Büthe, C. Vogt, L. Petti, G. Cantarella, N. Münzenrieder, and G. Tröster, "Fabrication, modeling and evaluation of a digital

- output tilt sensor with conductive microspheres," *IEEE Sensors Journal*, 2016, submitted.
- [109] T. Minami, H. Sonohara, T. Kakumu, and S. Takata, "Physics of very thin ito conducting films with high transparency prepared by dc magnetron sputtering," *Thin Solid Films*, vol. 270, no. 1, pp. 37–42, 1995.
- [110] Shockwatch, "Tilt indicators - shipping and handling monitoring devices," accessed 17.09.2016. [Online]. Available: <http://shockwatch.com/products/impact-and-tilt/tilt-indicators>
- [111] E. L. Tan, W. N. Ng, R. Shao, B. D. Pereles, and K. G. Ong, "A wireless, passive sensor for quantifying packaged food quality," *Sensors*, vol. 7, no. 9, p. 1747, 2007.
- [112] C. Li, Q. Tan, C. Xue, W. Zhang, Y. Li, and J. Xiong, "A high-performance lc wireless passive pressure sensor fabricated using low-temperature co-fired ceramic (ltcc) technology," *Sensors*, vol. 14, no. 12, pp. 23 337–23 347, 2014.
- [113] L. Büthe, M. Hardegger, P. Brülisauer, and G. Tröster, "Rfid-die: Battery-free orientation sensing using an array of passive tilt switches," in *Proceedings of the 2014 ACM International Joint Conference on Pervasive and Ubiquitous Computing: Adjunct Publication*, 2014, pp. 215–218.

Glossary

Notation	Description	Page List
A_{disk}	Area of the microsphere disk	70
A_{sphere}	Cross-section area of a microsphere	70
E	Young's modulus	40, 52
F_N	Normal force of microsphere on substrate surface	50, 56, 57
F_{ind}	Indentation force	52
I	Second moment of area	40
N	Number of contact pads	60, 64, 66, 68–71
$N_{spheres}$	Amount of microspheres	60, 70, 71
R	Radius of microsphere	50, 52
R_C	Constriction resistance	48
R_S	Sharvin resistance	48, 49
R_{sp}	Sphere resistance	48, 50
α	Tilt angle of device	21, 64, 75, 78–80, 82, 83
α_T	Coefficient of thermal expansion	39
α_{break}	Break angle of tilt switch	76
α_{hys}	Hysteresis angle of tilt sensor	80, 82
α_{make}	Make angle of tilt switch	75, 76
α_{pad}	Angle of a single contact pad	60
α_{res}	Angular resolution	60, 62, 71
β	Tilt angle of sensor plane	20, 78–80, 82
δ	Rotation angle of second rotation axis	78
δ_n	Packing density	70
η_{disk}	Ratio of microsphere disk height and cavity radius	67
η_{pad}	Ratio of ground to contact pad	60, 67–69, 71
γ	Rotation angle of first rotation axis	78
γ_{lv}	Surface tension	26
μ_k	Kinematic friction coefficient	56
μ_{pad}	Representation of η_{pad} between 0 and 1	68

Notation	Description	Page List
ν	Poisson ratio	52
ω	Angular velocity	86
ρ_l	Density of liquid	27
θ	Contact angle of liquid with solid surface	26
θ_i	Central angles of contact and ground pad to the horizontal	66, 67
φ	Angle between horizontal and top of microsphere disk	67
ξ_{states}	Evaluation parameter describing the non-linearity	62, 65–69
a	Radius of a -spots	48, 49, 55
a_c	Centripetal acceleration	86
c_{dist}	Spacing between pillars	40–42
c_{pillar}	Edge length of a pillar	40–42
d_{crit}	Critical penetration depth	54, 55
d_{ind}	Indentation depth	52
h	Height	27
h_{disk}	Height of microsphere disk	61, 66–71
l_{fp}	Mean free path of electrons	49, 50
r_{cavity}	Radius of sensor cavity	60, 65, 67, 70, 71
$r_{contact}$	Inner contact radius of contact pads	60, 66, 71
ADC	Analog-to-digital converter	62
AFM	Atomic force microscopy	52–57
Al	Aluminum	35
Au	Gold	34, 35, 57, 84
CMOS	Complementary metal-oxide semiconductor	6
Cr	Chrome	34, 35
DC	Direct current	4
FBG	Fiber bragg grating	6

Notation	Description	Page List
GaInSn	Gallium indium tin	7
HWA	Healthcare, wellness and assisted living	xiii
IL	Ionic liquid	27
ITO	Indium tin oxide	84
LC	Circuit with inductance and capacitance forming a resonant circuit	93
LED	Light emitting diode	6, 79, 84
LFM	Lateral force microscopy	56
MEMS	Micro-electromechanical system	3, 22
N ₂	Nitrogen	51
NaCl	Sodium chloride	8, 27
NFC	Near Field Communication	93
O ₂	Oxygen	35, 40, 45
OSA	Optical spectrum analyzer	6
PC	Personal computer	75, 79
PCF	Photonic crystal fiber	8
PI	Polyimide	xiii, xv
RFID	Radio Frequency Identification	93
RIE	Reactive ion etching	35, 40, 45, 50
RMS	Root mean square of surface roughness	53–55
SEM	Scanning electron microscopy	29, 36, 42–44
SF ₆	Sulfur hexafluoride	35
Si	Silicon	3, 57, 58

Notation	Description	Page List
SMD	Surface mount device	5
SNR	Signal to noise ratio	4
UV	Ultra violett	39, 40
ZnO	Zinc oxide	3